eXPRESS Polymer Letters Vol.3, No.4 (2009) 200
Available online at www.expresspolymlett.com
DOI: 10.3144/expresspolymlett.2009.25

Editorial corner – a personal view
Towards nanofibrillar single polymer composites

*S. Fakirov**

Centre for Advanced Composite Materials (CACM) at the Department of Mechanical Engineering of The University of Auckland, Auckland, Private Bag 92019, New Zealand

In their recent review 'How Nano Are Nanocomposites?' (*Macromolecules*, **40** (2007) 8501–8517) Schaefer and Justice concluded that: 'Composite materials loaded with nanometer-sized reinforcing fillers are widely believed to have the potential to push polymer mechanical properties to extreme values. Realization of anticipated properties, however, has proven elusive… With the exception of reinforced elastomers, nanocomposites have not lived up to expectations. Although claims of modulus enhancement by factors of 10 exist, these claims are offset by measurements that show little or no improvement…'.

Obviously, today we can hardly be happy with the mechanical performance of polymer composites reinforced with nano-sized fillers of various origins. For this reason, in addition to the attempts to overcome the encountered problems, new routes to create polymeric materials with improved properties have to be searched. Attractive alternative in this respect seems to be the *preparation of polymers themselves as nano-sized materials*, as for example electrospinning does. This elegant technique has the disadvantage that not that much can be done practically with the fine nanofibers.

The concept of microfibrillar composites (MFC), developed during the last decade, leads to the nanofibrillar composites (NFC), which are reinforced with polymer nanofibrils with diameters in the range of 50–150 nm. The latter can be isolated in a neat form after selective dissolution of the second blend component, even after preparation of fabrics or knitted articles from the blend yarn. The neat nanofibrils can be used as a starting material for preparation of nanostructured single polymer composites (SPC) applying the one- or two constituent approach.

Very recently we demonstrated the superior mechanical properties of the new poly(ethylene terephthalate) (PET) nanofibrillar SPC prepared via hot compaction using one constituent – the modulus is competitive with that of the glass fiber/PET (40/60 by wt) composites.

In conclusion, the MFC and NFC concept makes possible the conversion of any polymer in a neat nano- or microfibrillar form and to apply these materials for the preparation of one- or two constituent SPC via hot compaction. The final one-constituent nanocomposite is manufactured starting from nano-sized material only, a case which seems to be very rare if not unique.

Prof. Dr. Stoyko Fakirov
Member of International Advisory Board

*Corresponding author, e-mail: s.fakirov@auckland.ac.nz

eXPRESS Polymer Letters Vol.3, No.4 (2009) 201–206
Available online at www.expresspolymlett.com
DOI: 10.3144/expresspolymlett.2009.26

Gelatin films plasticized with a simulated biodiesel coproduct stream

M. Singh[1], *J. Milano*[1], *E. S. Stevens*[1*], *R. D. Ashby*[2], *D. K. Y. Solaiman*[2]

[1]Department of Chemistry, State University of New York at Binghamton, Binghamton, New York 13902, USA
[2]United States Department of Agriculture, ARS, ERRC, 600 East Mermaid Lane, Wyndmoor, Pennsylvania 19038, USA

Received 11 January 2009; accepted in revised form 17 February 2009

Abstract. In order to explore the possibility of substituting an unrefined biodiesel coproduct stream (BCS) for refined glycerol as a polymer plasticizer we have prepared cast gelatin films plasticized with a simulated BCS, i.e., mixtures of glycerol and some of the typical components found in BCS (methyl linoleate, methyl oleate, linoleic acid, and oleic acid). We measured the tensile properties as a function of plasticizer composition, and analyzed the specific effect of each individual component on tensile properties. We found that it is the unrecovered alkyl esters that largely determine the tensile properties, and that BCS can be successfully used to plasticize cast gelatin films as long as the BCS contains 11 parts by weight, or less, of unrecovered alkyl esters per 100 parts glycerol.

Keywords: *biopolymers, biodegradable polymers, mechanical properties, gelatin, biodiesel glycerol*

1. Introduction

In biodiesel production, the sale of coproduct glycerol can help to offset the costs of raw materials [1]. However, over the last few years biodiesel production has expanded at rates that have never before been seen. As the amount of available glycerol continues to exceed the market demand, the value of the biodiesel coproduct stream (BCS) has been drastically reduced. Currently, there is a push to find new outlets for BCS in order to help maintain its value. Success in this area would increase the feasibility of fuel production and also improve the economics of biorefinery operations.

Glycerol acts as a plasticizer by reducing the polymer glass temperature, and many applications have been described in the literature. Recent studies continue to illustrate its potential for practical use with both biopolymers and synthetic polymers [2–11].

Stevens *et al.* [12] have recently shown that replacing glycerol with a commercial sample of an unrefined BCS did not prevent the formation of viable cast gelatin films, and did not result in the deterioration of tensile properties. Studies of the use of an unrefined BCS as a plasticizer had not previously been reported.

The objective of the present work was to continue to elucidate the potential of using unrefined BCS as a bioplastics plasticizer. The specific aim was to quantify the composition requirements of the BCS necessary in such applications. BCS typically contains, other than glycerol, unreacted fatty acids and unrecovered fatty acid esters. Here we prepared cast gelatin films plasticized with a simulated BCS, i.e., mixtures of glycerol and some of the typical components found in BCS derived from a soy oil or canola oil process (methyl linoleate, methyl oleate, linoleic acid, and oleic acid). The tensile properties were measured as a function of plasticizer composition, and the specific effect of each individual component on tensile properties was analyzed.

*Corresponding author, e-mail: stevens@binghamton.edu

Gelatin was chosen for the present study because it is produced in large amounts for use in a variety of industrial processes, including the manufacture of pharmaceutical products, x-ray and photographic films development, and food processing [13]. It has been used as a component in bone substitute materials [14]. Also, gelatin, unlike some biopolymers, is thermoplastic and can be processed by conventional means, such as extrusion and injection molding [13, 15].

2. Materials and methods

2.1. Materials

Gelatin (Type A G2500), glycerol, methyl linoleate (≥99%), methyl oleate (99%), linoleic acid (≥99%), oleic acid (~99%), and ammonium hydroxide (30% aqueous solution) were purchased from Sigma-Aldrich Chemicals.

2.2. Film compositions

Previous work [12] had shown that a mid-range composition of gelatin-glycerol cast films, with respect to tensile properties, is approximately 72% gelatin and 28% glycerol. Here, we prepared films with a total weight, excluding water, of 6.0 g, containing 4.32 g gelatin and 1.68 g total plasticizer.

The composition of BCS varies with feedstock and biodiesel processing efficiency. As a typical composition we used that previously described [12] in which the organic component, excluding methanol, contained 82% glycerol and 18% other organics. In that sample the other organics were mainly unreacted free fatty acids and unrecovered fatty acid methyl esters, in approximately equal proportions. We therefore defined a series of simulated BCS mixtures, each containing an organic component of 1.38 g glycerol and 0.30 g of other BCS organic compounds, corresponding to 22 parts by weight per 100 parts glycerol.

Two common sources of biodiesel feedstocks are soy oil and canola oil (low erucic acid rapeseed oil). In both oils, the major fatty acids are linoleic and oleic acids, but the relative amounts (linoleic/oleic) differ, typically 53/23 in soy oil and 21/61 in canola oil [16]. Based on these considerations, we prepared the series of samples with compositions shown in Table 1.

In Table 1, the film compositions are presented in units of grams; the plasticizer (simulated BCS) compositions are described in units of parts by weight of each component per 100 parts glycerol.

Sample 1 was a control. In the remaining samples 18% of the glycerol was replaced with BCS components as shown in Table 1. In samples 8 and 9, the fatty acid and methyl ester of both fatty acids were used, in 2:1 and 1:2 proportions, respectively, approximating the proportions in soy oil and canola oil.

Samples were first prepared without the addition of ammonium hydroxide. Those samples, however, showed signs, by visual inspection, of macroscopic film heterogeneity and phase separation; there were visible dispersed droplets, larger than 1 mm in diameter, embedded in the gelatin/glycerol matrix. The films were not characterized further.

The films described herein were prepared with ammonium hydroxide. Previous work [12] had shown that, once dry, there is no free ammonia or ammonia odor.

Table 1. Composition [g] of gelatin samples plasticized with BCS components[a]. In parentheses is shown the parts by weight per 100 parts glycerol.

Sample	Glycero	Methyl Linoleate	Methyl Oleate	Linoleic Acid	Oleic Acid
1[b]	1.68	0	0	0	0
2	1.38	0.30 (21.7)	0	0	0
3	1.38	0	0.30 (21.7)	0	0
4	1.38	0	0	0.30 (21.7)	0
5	1.38	0	0	0	0.30 (21.7)
6	1.38	0.15 (10.9)	0	0.15 (10.9)	0
7	1.38	0	0.15 (10.9)	0	0.15 (10.9)
8	1.38	0.10 (7.2)	0.05 (3.6)	0.10 (7.2)	0.05 (3.6)
9	1.38	0.05 (3.6)	0.10 (7.2)	0.05 (3.6)	0.10 (7.2)
10	1.38	0.075 (5.4)	0.075 (5.4)	0.075 (5.4)	0.075 (5.4)

[a]Each sample contained 4.32 g gelatin. Total weight of gelatin plus plasticizer was 6.0 g.

[b]Sample 1 was prepared in duplicate.

2.3 Preparation of films

4.32 g gelatin was added to 2% (v/v) aqueous glycerol solution; the density of glycerol is 1.26 gm/cm^3. Other components were added according to Table 1. Ammonium hydroxide was added as 6 ml of aqueous NH_4OH solution (30%). Water was added to bring the total volume to 150 ml. The samples were heated with stirring to 85–95°C in an open beaker. Films were cast, and dried at ambient laboratory temperature and relative humidity.

2.4. Morphology

Film samples were optically scanned using a Hewlett Packard ScanJet 5370C and VueScan software.

2.5. Tensile properties

Films were stored for four weeks at ambient laboratory conditions prior to tensile testing. Immediately before testing, they were conditioned at a temperature of 23±2°C and relative humidity of 50±5%, according to ASTM Standard Practice D618. Tensile measurements were made on an Instron Model 5543 testing system with a 100 N load cell according to ASTM Test Method D882. Specimen width was 1.27 cm; gage length was 5.08 cm; and test speed was 5.08 cm/min.

2.6. Modeling

Tensile properties for the ten samples, with separate values for the duplicates of sample 1, provided eleven data points for the least squares fitting of tensile properties. Tensile properties were modeled with SAS JMP7 software (SAS Institute, Cary, NC). The Fit Model routine was used with the standard least squares fitting option. Role variables were elongation, modulus, or tensile strength. Effects were the amounts of linoleic acid, methyl linoleate, oleic acid, and methyl oleate. Cross-terms were added if doing so improved the model statistics. Goodness of fit of the model was measured by R^2, root mean square error, and p value. Low p values reflect the statistical significance of the analysis; composition factors with a p value greater than 0.05 were eliminated.

3. Results

3.1. Morphology

Sample 1 was clear and showed no signs of phase heterogeneity. Sample 2, containing 22 parts by weight of methyl linoleate per 100 parts glycerol, contained droplets of the methyl ester dispersed within the gelatin/glycerol matrix (Figure 1). The droplets were approximately 1000 μ in diameter. There were also smaller droplets, approximately 200–300 μ in diameter. Sample 3, containing the same level of methyl oleate, appeared similar to sample 2.

Samples 4 and 5, containing 22 parts by weight of linoleic acid and oleic acid, respectively, per 100 parts glycerol, appeared macroscopically homogeneous and were indistinguishable from the control.

Sample 6 (Figure 1) and samples 7–10, containing only 11 parts by weight of a methyl ester, displayed dispersed droplets distinctly smaller than the 1000 μ diameter droplets in samples 2 and 3.

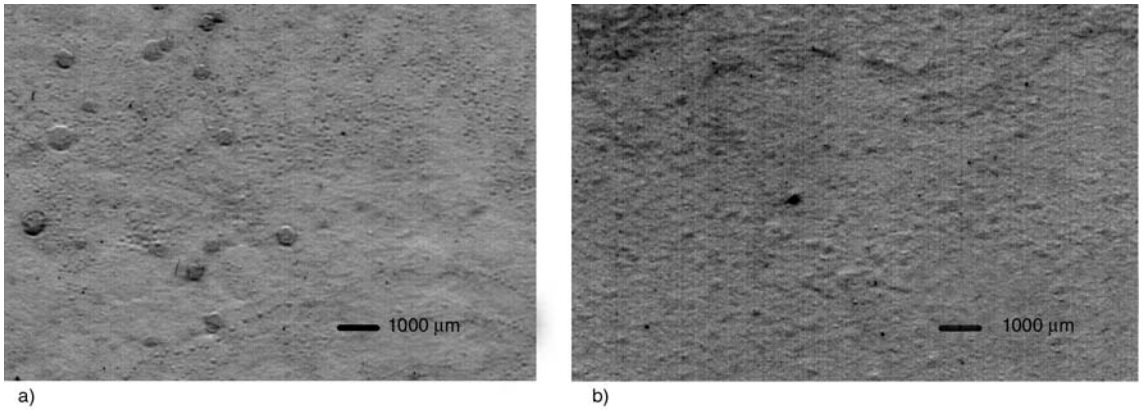

Figure 1. Optical scans of samples 2 (a) and 6 (b) containing, respectively, 22 and 11 parts by weight of methyl linoleate per 100 parts glycerol

3.2. Tensile properties

Results of the tensile measurements, including elongation at break (ε), Young's modulus (*E*), and stress at break (σ), are displayed graphically in Figure 2. Average values and standard deviations are shown; $N = 5$. For sample 1, the average of two sample sets of five specimens each is shown. The average sample thickness ranged from 0.15–0.21 mm. Also shown are the previously reported results for a film prepared with a commercial sample of BCS [12].

3.3. Modeling

A summary of the modeling statistics is shown in Table 2. The fits of all three tensile properties were statistically significant; at least 93% of the variance was accounted for (R^2), *rms* (root mean square) values are only slightly larger than or the same as the standard deviations of the individual samples, and all *p* values were significantly smaller than 0.05.

4. Discussion

4.1. Morphology

The films appeared tough and leathery at all compositions; gelatin films plasticized with glycerol and components of BCS are viable films. Methyl esters, when present at a level of 22 parts by weight per 100 parts glycerol (samples 2 and 3), lead to significant film heterogeneities (Figure 1); 1000 μ

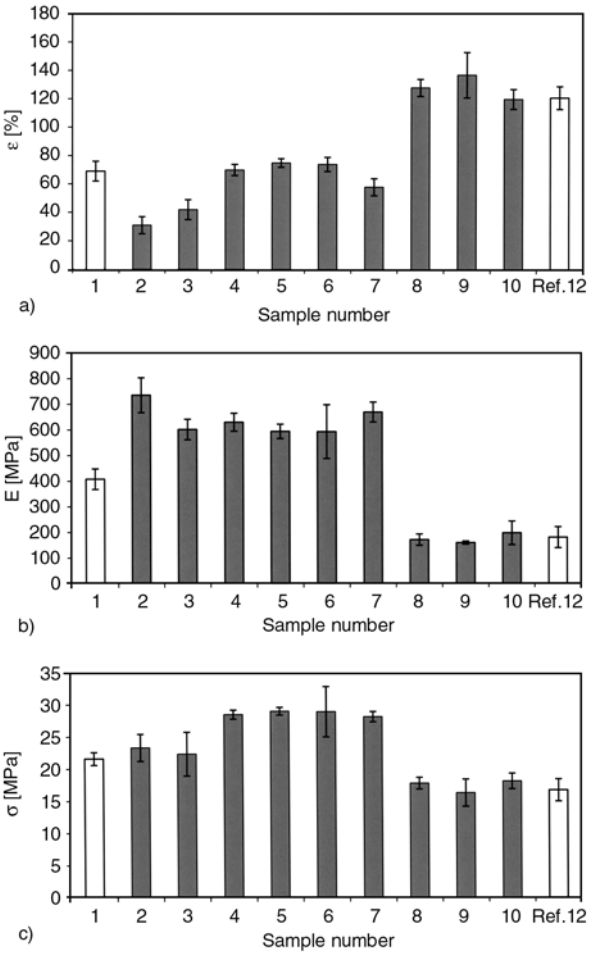

Figure 2. a) Elongation at break (ε), b) Young's modulus (*E*), and c) tensile stress at break (σ) of cast gelatin films 1–10 described in Table 1. Also shown are the previously reported results for a film prepared with a commercial sample of BCS [12].

Table 2. Statistical Results from Modeling Tensile Properties of Gelatin Films[a]

Property/factor	R^2	rms error	Scaled estimate	p value
Elongation	0.93	11%		0.0002
Methyl linoleate			108 ± 13	<0.0001
Methyl oleate			110 ± 13	<0.0001
Methyl linoleate × Methyl oleate[b]			306 ± 31	<0.0001
Modulus	0.96	57 MPa		0.0012
Methyl linoleate			–662 ± 72	0.0002
Methyl oleate			–703 ± 72	0.0002
Methyl linoleate × Methyl oleate[b]			–1980 ± 173	<0.0001
Linoleic acid			94 ± 33	0.0342
Oleic acid			103 ± 33	0.0248
Tensile strength	0.94	1.7 MPa		0.0047
Methyl linoleate			–15 ± 2	0.0008
Methyl oleate			–16 ± 2	0.0007
Methyl linoleate × Methyl oleate[b]			–40 ± 5	0.0005
Linoleic acid			3.9 ± 1.0	0.0094
Oleic acid			4.0 ± 1.0	0.0086

[a]R^2 is a measure of the variance that is explained by the model; rms is the root mean square error; scaled estimate is a measure of the relative importance of the various factors for a given property. For *p* value see text.

[b]A cross term indicates that the effect of one factor depends on the other factor

diameter droplets of methyl ester are dispersed non-uniformly throughout the gelatin/glycerol matrix. Presumably, the heterogeneities are the result of unfavorable interactions between the uncharged fatty acid methyl esters and the disordered gelatin chains, resulting in self-association of the methyl esters.

Free fatty acids, even when present at a level of 22 parts by weight per 100 parts glycerol (samples 4 and 5), are compatible with the gelatin/glycerol matrix; the films are clear and similar in appearance to the control. Presumably, film homogeneity is a result of favorable interactions between the deprotonated fatty acids and the charged side-chains and dipole moments of the disordered gelatin chains.

Films containing only 11 parts of methyl ester per 100 parts glycerol (samples 6–10) appear more homogeneous than films containing 22 parts of methyl ester; the large 1000 μ diameter droplets observed in samples 2 and 3 (Figure 1) are absent.

Ammonium hydroxide improves film homogeneity, regardless of composition. Differential scanning calorimetry results, previously reported [12], showed that ammonium hydroxide prevents the partial renaturation of gelatin during film formation. The present study suggests that it is the maintaining of disordered polymer chains that is responsible for the increase in film homogeneity when ammonium hydroxide is used.

4.2. Tensile properties

The low elongations, relative to the control, of films containing 22 parts by weight of methyl ester per 100 parts glycerol (Figure 2a, samples 2 and 3) correlate with those films displaying the greatest phase heterogeneity, and may be a consequence of the heterogeneity. Otherwise, the most notable feature of the tensile properties (Figure 2) is the similarity of samples 2–7, containing only C18:2 molecules (linoleic acid and methyl linoleate) or C18:1 molecules (oleic acid and methyl oleate), but not both. When both types are present, as in samples 8–10, the properties are significantly different; the difference is most notable for the elastic modulus. This result indicates that the interactions of C18:2 molecules with C18:1 molecules are different from the interactions between like molecules, in a way that affects tensile properties. Presumably, the overall difference in tensile behavior is the net result of polymer-additive interactions, through coefficients of adhesion, on the one hand, and additive-additive interactions, on the other.

It should be pointed out that tensile data for samples 8–10 are consistent with results previously reported for gelatin films plasticized with a commercial BCS which displayed a similar elongation (121±8%), modulus (179±41 MPa), and tensile strength (16.6±1.7 MPa) [12].

The tensile measurements provide quantitative data corroborating the physical description of the films as tough and leathery. It is also worth noting that there is no statistically significant difference between the tensile properties of sample 8, simulating a soy-derived BCS, and sample 9, simulating a canola-derived BCS.

4.3. Modeling

The modeling results confirm the important role of unrecovered methyl esters in determining the tensile properties of BCS-plasticized gelatin films. The scaled estimates (Table 2) show that it is the methyl esters that are the main determinants of tensile properties. When both methyl linoleate and methyl oleate are present, methyl esters increase elongation (positive scaled estimates) relative to glycerol and decrease modulus and tensile strength (negative scaled estimates). Significant cross terms between the two types of ester dominate the determination of tensile properties and confirm their interaction; when both are present, their effects are not additive. The fatty acid components play relatively small roles in determining tensile properties.

5. Conclusions

Methyl esters, present in BCS as unrecovered products of biodiesel production, play an important role in determining the tensile properties of cast gelatin films plasticized with BCS. Unreacted fatty acids play less of a role. Methyl esters, when present at levels greater than 11 parts by weight per 100 parts glycerol, are poorly incorporated into the gelatin/glycerol matrix, leading to decreased elongations. There are significant interactions between the C18:2 linoleic and C18:1 oleic components. There is no statistically significant difference between the tensile properties of gelatin films plasticized with a

composition simulating a soy-derived BCS and those of gelatin films plasticized with a composition simulating a canola-derived BCS.

In practical terms, the tensile properties of gelatin films could be modulated according to what properties are required. For example, to achieve the same elongation as films plasticized with refined glycerol, a smaller amount of BCS would be required. Also, the possibility exists of using blends of BCS and refined glycerol for additional control of properties.

In the commercial BCS used in the previous study of gelatin films [12], methyl esters were present in only 8 parts by weight per 100 parts of glycerol, which accounts for the homogeneity of the films observed in that study.

Acknowledgements

This work was carried out under USDA Cooperative Agreement 58-1935-7-731N.

References

[1] National Biodiesel Board: The economics of producing energy crops. (2009) http://www.biodiesel.org/resources/reportsdatabase/reports/gen/19930101_gen_293.pdf

[2] Franke H. G., Bittner D. R.: Resilient biodegradable packaging materials. U.S. Patent 7135063, USA (2006).

[3] Tanner K. E., Draper P. R., Getz J. J., Burnett S. W., Youngblood E.: Film forming compositions comprising modified starches and iota-carrageenan and methods for manufacturing soft capsules using same. U.S. Patent 6340473, USA (2006).

[4] Feinberg S. C., Talkowski C. J., Andersen K. C.: Compositions compromising ionomers and polyamide. U.S. Patent 7144938, USA (2006).

[5] Narayan R., Balakrishnan S., Nabar Y., Shin B-Y., Dubois P., Raquez J-M.: Chemically modified plasticized starch compositions by extrusion processing. U.S. Patent 7153354, USA (2006).

[6] Bastioli C., Bellotti V., Cella G. D., Del Giudice L., Montino S., Perego G.: Biodegradable polymeric compositions comprising starch and a thermoplastic polymer. U.S. Patent 7176251, USA (2007).

[7] Overby R. J., Schulz O. H., Burgess A. V., Haggard W. O., Vincent M.: Synthetic bone substitute. U.S. Patent 7250550, USA (2007).

[8] Tábi T., Kovács J. G.: Examination of injection moulded thermoplastic maize starch. Express Polymer Letters, **1**, 804-809 (2007). DOI: 10.3144/expresspolymlett.2007.111

[9] Yu L., Coombs S., Christie G. B. Y.: Biodegradable polymer. U.S. Patent 7326743, USA (2008).

[10] Stevens H. G.: PVA-containing compositions. U.S. Patent 7279510, USA (2008).

[11] Cao X., Chen Y., Chang P. R., Muir A. D., Falk G.: Starch-based nanocomposites reinforced with flax cellulose nanocrystals. Express Polymer Letters, **2**, 502–510 (2008). DOI: 10.3144/expresspolymlett.2008.60

[12] Stevens E. S., Ashby R. D., Solaiman D. K. Y.: Gelatin plasticized with a biodiesel coproduct stream. Journal of Biobased Materials and Bioenergy, **3**, 57–61 (2009). DOI: 10.1166/jbmb.2009.1007

[13] Rouilly A., Rigal L.: Agro-materials. A bibliographic review. Polymer Reviews, **42**, 441–479 (2002). DOI: 10.1081/MC-120015987

[14] Bundela H., Bajpai A. K.: Designing of hydroxyapatite-gelatin based porous matrix as a bone substitute: Correlation with biocompatibility aspects. Express Polymer Letters, **2**, 201–213 (2008). DOI: 10.3144/expresspolymlett.2008.25

[15] Das M., Banthia A. K., Bal S.: Tensile stress and elongation properties of edible plastics from starch. Indian Journal of Chemical Technology, **5**, 209–212 (1998).

[16] Wool R. P.: Polymers and composite resins from plant oils. in 'Bio-based polymers and composites' (eds.: Wool R. P., Sun X. S.) Elsevier, New York, 56–113 (2005).

eXPRESS Polymer Letters Vol.3, No.4 (2009) 207–218
Available online at www.expresspolymlett.com
DOI: 10.3144/expresspolymlett.2009.27

Optimization of chlorpheniramine maleate (CPM) delivery by response surface methodology – four component modeling using various response times and concentrations of chitosan-alanine, glutaraldehyde and CPM

K. Kumari[1], *K. Prasad*[2], *P. P. Kundu*[1*]

[1]Department of Chemical Technology, Sant Longowal Institute of Engineering & Technology, Longowal-148106, India
[2]Department of Food Technology, Sant Longowal Institute of Engineering & Technology, Longowal-148106, India

Received 13 December 2008; accepted in revised form 23 January 2009

Abstract. The aim of the current study was to investigate the effects of formulation variables on the release of drug and to optimize the formulation of chitosan-alanine beads loaded with chlorpheniramine maleate (CPM) for controlled release using response surface methodology (RSM). Drug loaded beads of chitosan-alanine were prepared and crosslinked by using glutaraldehyde as crosslinker. The release behavior of drug was affected by preparation variables. A central composite design was used to evaluate and optimize the effect of preparation variables; chitosan concentration (X_1), percentage of crosslinker (X_2), concentration of drug (X_3) and release time (X_4) on the cumulative amount of drug release, Y in solutions of pH = 2.0 and pH = 7.4, respectively. The influence of each parameter was studied by factorial design analysis. Analysis of variance (ANOVA) was also used to evaluate the validity of the model. The statistical parameters reveal strong evidence that the constructed models for drug release in pH = 2 and pH = 7.4 are reliable.

Keywords: *biodegradable polymers, chitosan, controlled drug release, crosslinking, response surface methodology (RSM)*

1. Introduction

Chitosan is a deacetylated derivative of chitin which is a water insoluble polymer, (N-acetyl-d-glucosamine) found in nature, present in insect exoskeletons, outer shells of crabs, shrimps, lobsters etc. and fungal cell walls. It has been extensively studied as a carrier for drugs owing to its biocompatibility and biodegradability [1–5]. Chitosan based interpenetrating polymer networks (IPNs) currently received enormous interest for medical and pharmaceutical applications due to their good biocompatibility, low degradation and processing ease. The ability of these IPNs to swell and dehydrate depend on composition and environment which has been exploited to facilitate a range of applications such as drug release, its biodegradability and ability to form hydrogels [6].

Drug release from chitosan based IPNs can be controlled by the matrix density, which is affected by various factors, such as concentration of chitosan, percentage of crosslinking agent, amount of drug and response time [7–8]. However, quantitative aspects of the effects and relationships among these various factors have not been studied extensively. The authors [9–10] have prepared semi-IPNs consisting of chitosan-alanine and chitosan-glutamic acid and studied their cure kinetics [11]. The biocompatibility is the reason behind the use of L-ala-

*Corresponding author, e-mail: ppk923@yahoo.com

nine along with chitosan and it (alanine) acts as spacer in the formation of semi-IPN. In order to form semi-interpenetrating polymer network, two chitosan polymer chains are crosslinked by glutaraldehyde. Amino groups of chitosan and alanine can react with glutaraldehyde resulting in the attachment of alanine in pendent form. Hence, the resultant polymer system is characterized as semi-IPN (one phase consists of crosslinked chitosan and the other phase is made of alanine attached chitosan).

Response surface methodology (RSM) is a collection of statistical and mathematical techniques, useful for developing, improving and optimizing processes [12–14]. It also has an important application in the design, development and formulation of new products as well as in the improvement of existing product designs. The basic components of response surface methodology include experimental design, regression analysis and optimization algorithms which are used to investigate the empirical relationship between one or more measured responses and a number of independent variables, with the ultimate goal of obtaining an optimal problem solution. RSM is a widely practiced approach in the development and optimization of drug delivery devices [15–17]. Based on the principle of design of experiments (DOE), the methodology encompasses the use of various types of experimental designs, generation of polynomial equations, and mapping of the response over the experimental domain to determine the optimum formulation(s) [18–21]. The technique requires minimum experimentation and time, thus proving to be far more effective and cost-effective than the conventional methods of formulating dosage forms.

The objectives are to investigate the effects of formulation variables on the release of drug from crosslinked chitosan-alanine beads and to optimize the preparation of drug loaded chitosan-alanine crosslinked beads for drug release using RSM. Chlorpheniramine maleate (CPM), which is a sedating antihistamine drug used for the symptomatic relief of allergic conditions, is selected as model drug.

2. Materials and methods

2.1. Materials

Chitosan (percentage of deacetylation 80%; total nitrogen: 7% minimum, ignition residue (sulfate): <2% and loss on drying <15%) is procured from Tokyo Kasei Kogyo Co., Ltd. Japan and used as received. Chlorpheniramine maleate (CPM) [$C_{16}H_{19}ClN_2C_4H_4O_4$] ($pK_a$ value = 9.4) is obtained as a gift sample from Japson Pharmaceuticals Ltd. Sangrur, India. Glutaraldehyde ($C_5H_8O_2$) (MW = 100.11) 25% aqueous, acetic acid and L-alanine [$CH_3CH(NH_2)COOH$] (MW = 89.09) are purchased from CDH (New Delhi, India) and are of analytical grade.

2.2. Experimental design

A central composite design (CCD) is employed to fit a second order model. The levels are calculated and experiments are performed using CCD described elsewhere [22]. The four independent formulation variables selected for this particular study are the amount of chitosan (X_1), the percentage of crosslinker i.e. glutaraldehyde (X_2), the drug loading level (X_3) and the time of drug release (X_4). The weight of alanine is taken proportional to weight of chitosan and all other parameters like 2% acetic acid solution (20 ml), amount of crosslinker (10 ml) and processing conditions such as temperature and drug release media (pH 2.0 and 7.4), are kept invariant throughout the study. The amount of drug release $Y(2)$ and $Y(7.4)$ in different pH solutions (pH 2 and 7.4) are studied as the dependent variables. The actual amounts and corresponding coded values of different variables taken for the design are reported in Table 1. The ranges of independent variables are chosen on the basis of the results obtained from the previous studies, conducted in our laboratory [9]. The range of concentration of chitosan is taken as 0.1–0.9 g/20 ml beyond which, it becomes very difficult to extrude

Table 1. Independent variables and their coded values for the central composite design

X_i	Independent variables	Coded values				
		–2	**–1**	**0**	**1**	**2**
X_1	chitosan [g]	0.1	0.3	0.5	0.7	0.9
X_2	glutaraldehyde (10 ml) [%]	0	6.25	12.5	18.8	25
X_3	drug [mg]	25	50	75	100	125
X_4	drug release time [hrs]	2	3	4	5	6

Table 2. Prepared formulations as per the experimental design

Trial No.	Formulation variables			
	Chitosan [g]	Glutaraldehyde (10 ml) [%]	Drug (CPM) [mg]	Response time [hrs]
	(X_1)	(X_2)	(X_3)	(X_4)
F1	0.3	6.25	50	3
F2	0.7	6.25	50	3
F3	0.3	18.8	50	3
F4	0.7	18.8	50	3
F5	0.3	6.25	100	3
F6	0.7	6.25	100	3
F7	0.3	18.8	100	3
F8	0.7	18.8	100	3
F9	0.3	6.25	50	5
F10	0.7	6.25	50	5
F11	0.3	18.8	50	5
F12	0.7	18.8	50	5
F13	0.3	6.25	100	5
F14	0.7	6.25	100	5
F15	0.3	18.8	100	5
F16	0.7	18.8	100	5
F17	0.1	12.5	75	4
F18	0.9	12.5	75	4
F19	0.5	0	75	4
F20	0.5	25.0	75	4
F21	0.5	12.5	25	4
F22	0.5	12.5	125	4
F23	0.5	12.5	75	2
F24	0.5	12.5	75	6
F25	0.5	12.5	75	4
F26	0.5	12.5	75	4
F27	0.5	12.5	75	4
F28	0.5	12.5	75	4
F29	0.5	12.5	75	4
F30	0.5	12.5	75	4

the solution through the syringe due to the high viscosity of the solution. At the same time, it is not possible to prepare the beads without substantial amount of chitosan. The drug release time is chosen as 2 to 6 hrs because a burst release is observed in the first hour and almost a plateau formation is there after sixth hour of drug release. The concentration of drug release $Y(2)$ and $Y(7.4)$ in pH solutions of 2.0 and 7.4, respectively are selected as response variables. Table 2 summarizes an account of thirty experimental runs conducted during study. The combinations of factors employed during the study and their responses are given in Table 3. The following second order model (Equation (1)) in X_1, X_2, X_3 and X_4 is fitted using the data in Table 3:

$$Y(\text{pH}) = \beta_0 + \beta_1 X_1 + \beta_2 X_2 + \beta_3 X_3 + \beta_4 X_4 + \beta_{12} X_1 X_2 + \beta_{13} X_1 X_3 + \beta_{14} X_1 X_4 + \beta_{23} X_2 X_3 + \beta_{24} X_2 X_4 + \beta_{34} X_3 X_4 + \beta_{11} X_1^2 + \beta_{22} X_2^2 + \beta_{33} X_3^2 + \beta_{44} X_4^2 \quad (1)$$

where β_0 is the intercept representing the arithmetic average of all quantitative outcomes of 30 runs; and β_1 to β_{44} are the coefficients computed from the observed experimental values of Y; and X_i's are the coded independent variables. Statistical validity of the polynomials is established on the basis of ANOVA technique. Subsequently, the feasibility and grid searches are performed to locate the composition of optimum formulations. The 2-D contour plots for drug release in acidic and basic medium are constructed using program developed in MATLAB V.5. The formulations corresponding to the design are prepared and evaluated for various

Table 3. Translation of actual units into coded levels and response for central composite design

Trial No.	Chitosan	Glutaraldehyde	Drug (CPM)	Response time	Response ($\cdot 10^{-4}$) [g/ml]	
	(X_1)	(X_2)	(X_3)	(X_4)	Y(2)	Y(7.4)
F1	–1	–1	–1	–1	7.24	8.33
F2	1	–1	–1	–1	6.84	7.71
F3	–1	1	–1	–1	6.74	8.27
F4	1	1	–1	–1	6.47	7.63
F5	–1	–1	1	–1	7.62	9.02
F6	1	–1	1	–1	7.50	8.46
F7	–1	1	1	–1	6.92	8.60
F8	1	1	1	–1	6.69	8.18
F9	–1	–1	–1	1	7.75	8.99
F10	1	–1	–1	1	7.16	8.32
F11	–1	1	–1	1	7.66	8.51
F12	1	1	–1	1	6.83	8.29
F13	–1	–1	1	1	8.25	9.35
F14	1	–1	1	1	7.94	8.61
F15	–1	1	1	1	7.54	8.86
F16	1	1	1	1	7.10	8.52
F17	–2	0	0	0	6.83	8.43
F18	2	0	0	0	6.10	7.34
F19	0	–2	0	0	9.16	9.92
F20	0	2	0	0	6.97	9.02
F21	0	0	–2	0	6.33	7.81
F22	0	0	2	0	7.89	9.48
F23	0	0	0	–2	6.24	8.69
F24	0	0	0	2	7.97	9.67
F25	0	0	0	0	7.40	9.01
F26	0	0	0	0	7.40	9.02
F27	0	0	0	0	7.40	9.01
F28	0	0	0	0	7.40	9.01
F29	0	0	0	0	7.41	8.98
F30	0	0	0	0	7.38	9.02

response properties. The resultant experimental data of response properties are quantitatively compared with that of the predicted values. Also, linear regression plots between actual and predicted values of the response properties are drawn using Microcal Origin 6.0, forcing the line to pass through origin.

2.3. Preparation of chitosan-alanine beads

Table 1 enlists the central composition design of different chitosan-alanine formulations prepared using varying amounts of the chitosan, alanine, glutaraldehyde and drug. Drug loaded beads of chitosan and alanine crosslinked with glutaraldehyde are prepared, as reported earlier [9]. Briefly, a known amount of CPM, chitosan and alanine are dissolved in 2% acetic acid solution by stirring conditions for three hours at room temperature. The composition of various formulations is given in Table 2. The homogeneous mixture is extruded in the form of droplets using a 0.56 mm diameter syringe into alkali–methanol solution (1:20 w/w) under stirring conditions. The beads are washed with hot and cold water, respectively. The resultant beads were allowed to react with 10 ml of glutaraldehyde solution (25, 18.8, 12.5 and 6.25%) at 50°C for about 10 min for crosslinking. The formation of crosslinked chitosan-alanine semi-IPN beads is shown in Figure 1. To form semi interpenetrating polymer network (semi-IPN), two chitosan chains are crosslinked by glutaraldehyde. Amino groups of chitosan and alanine can react with glutaraldehyde resulting in attachment of alanine in pendent form. Finally, the crosslinked beads were successively washed with hot and cold water and air dried at 37°C. After cross-linking, the strength of unreacted glutaraldehyde was determined by

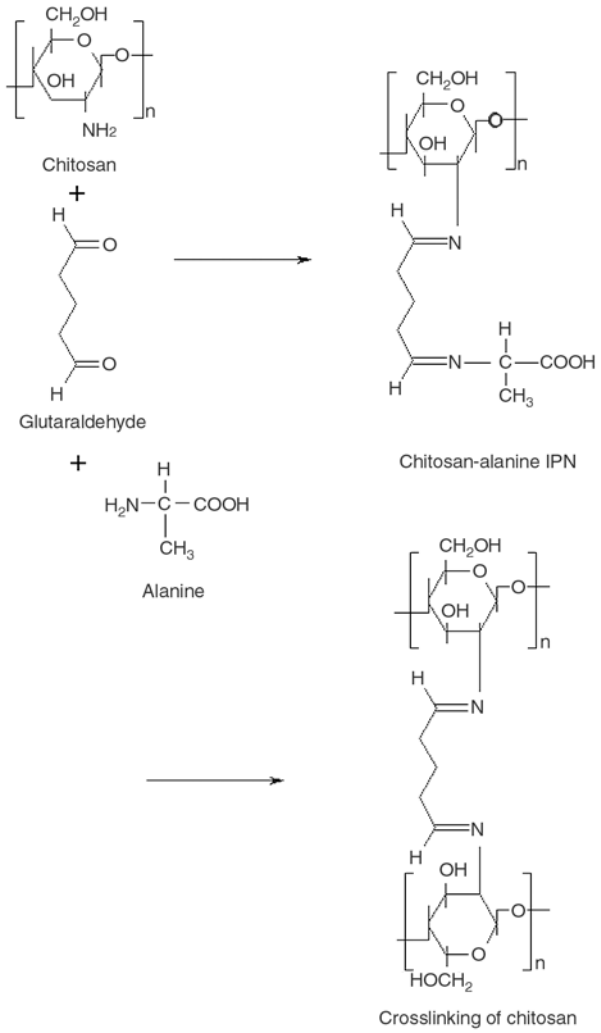

Figure 1. Schematic representation of crosslinking of chitosan and L-alanine by glutaraldehyde for the formation of interpenetrating network

Brady's reagent. The strength of residual glutaraldehyde, obtained after crosslinking the beads was in the range of 2–3.5%. In other words, more than 96% of glutaraldehyde was consumed during the crosslinking process and hence, a highly crosslinked structure was obtained.

2.4. In vitro drug release studies

The drug release experiments are performed in acidic and basic medium (30 ml each) for all the formulation combinations as reported elsewhere [9]. Briefly, the drug release experiments are performed in a glass apparatus at 37°C under unstirred conditions. Out of the prepared beads only 0.2 g are taken for the drug release studies which contain approximately 5, 10, 15, 20 and 25 mg of CPM drug, respectively. Different pH solutions (pH = 2 and pH = 7.4) are used as the drug release medium, and the samples of 3 ml are withdrawn periodically at predefined time intervals and analyzed under UV spectrophotometer at 193.5 nm. All the release experiments are carried out in triplicate and the average results are reported. In order to maintain nearly constant release environment and to get the cumulative drug release concentration, the samples withdrawn for the record of absorbance are immediately added back to the release medium after recording the absorbance. Drug release data are analyzed using ANOVA software.

3. Results and discussion

Semi-IPN beads of chitosan and L-alanine are formed by using glutaraldehyde as crosslinker. Alanine acts as a spacer between the chitosan polymer chains. The presence of alanine increases the void content of the semi-IPN and thus, lowers the tendency of 'blocking' effect of glutaraldehyde. It is further believed that due to the presence of a spacer, it is easier for the crosslinker to penetrate

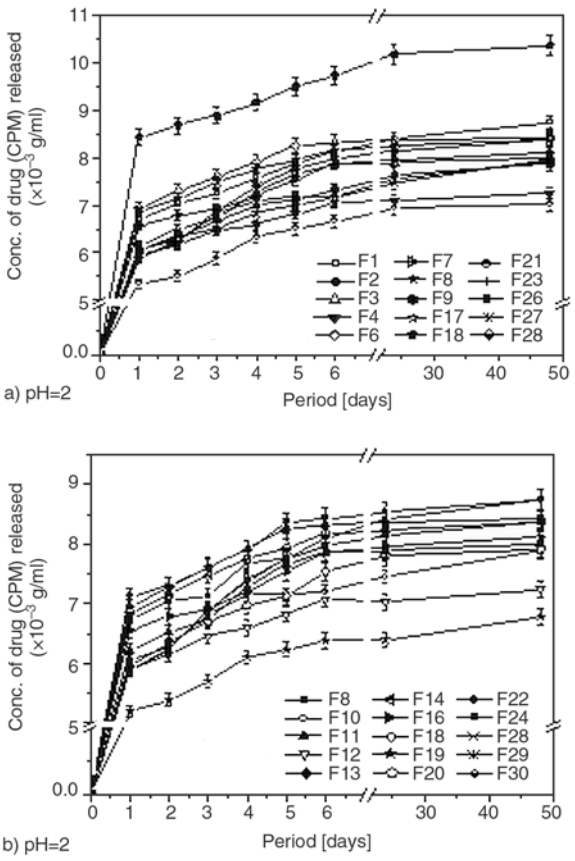

Figure 2. a) and b) drug release profiles through acidic medium from 30 formulations of chitosan-alanine crosslinked beads prepared using experimental design

into the core of the beads resulting in fully crosslinked network.

In vitro drug release studies are performed in acidic and basic environments. The crosslinked beads are immersed in solutions of pH = 7.4 and pH = 2.0, respectively. The dependence of drug release on concentration of chitosan, degree of crosslinking and nature of release environment is displayed in Figures 2 and 3. It is observed during the drug release experiments that the size of beads increases as a result of diffusion of solvent. Due to increase in the surface area of beads, the resistance to drug transport increases which lowers the rate of drug release in the latter part of study. Thirty experiments are required for central composite design to study the effect of various independent variables on drug release. The designed formulations and the observed responses for thirty experiments are given in Table 3. The polynomial equations relating the drug release responses $Y(2)$ and $Y(7.4)$ and independent variables are (Equations (2) and (3)):

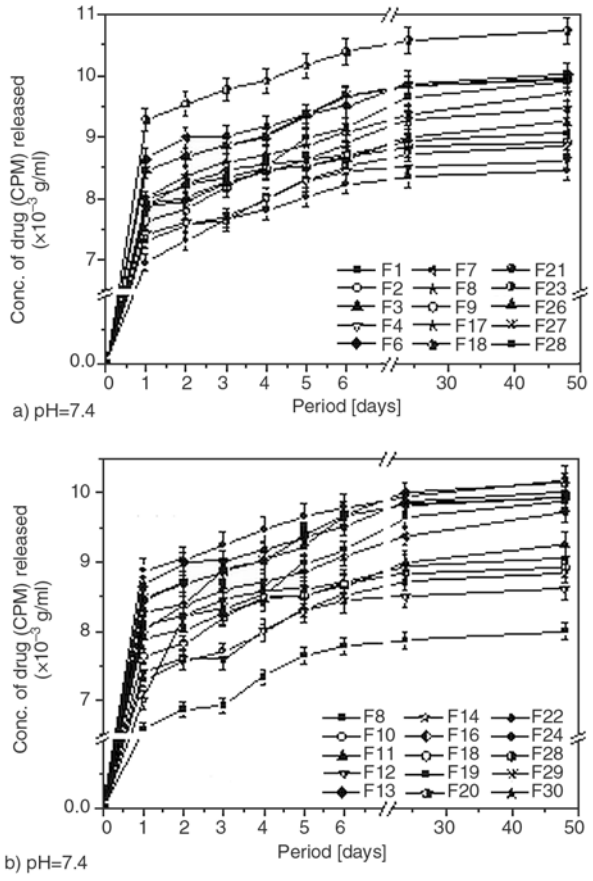

Figure 3. a) and b) drug release profiles through basic medium from 30 formulations of chitosan-alanine crosslinked beads prepared using experimental design

$$Y(2) = 7.4(\pm0.099) - 0.19(\pm0.049)X_1 - 0.36(\pm0.049)X_2 + 0.25(\pm0.049)X_3 + 0.32(\pm0.049)X_4 - 0.02(\pm0.06)X_1X_2 + 0.06(\pm0.06)X_1X_3 - 0.07(\pm0.06)X_1X_4 - 0.11(\pm0.06)X_2X_3 + 0.03(\pm0.06)X_2X_4 - 0.22(\pm0.046)X_1^2 + 0.18(\pm0.046)X_2^2 - 0.06(\pm0.046)X_3^2 - 0.06(\pm0.046)X_4^2 \quad (2)$$

$$Y(7.4) = 9.01(\pm0.098) - 0.27(\pm0.049)X_1 - 0.15(\pm0.049)X_2 + 0.29(\pm0.049)X_3 + 0.22(\pm0.049)X_4 + 0.06(\pm0.06)X_1X_2 + 0.01(\pm0.06)X_1X_3 + 0.02(\pm0.06)X_1X_4 - 0.04(\pm0.06)X_2X_3 - 0.02(\pm0.06)X_2X_4 - 0.07(\pm0.06)X_3X_4 - 0.33(\pm0.046)X_1^2 + 0.06(\pm0.046)X_2^2 - 0.14(\pm0.046)X_3^2 - 0.01(\pm0.046)X_4^2 \quad (3)$$

The Equations (2) and (3) represent the quantitative effect of the independent variables (X_1, X_2, X_3 and X_4) and their interactions on the responses $Y(2)$ and $Y(7.4)$, respectively. Coefficients with more than one factor term and those with higher order terms represent interaction terms and quadratic relationships, respectively. A positive sign represents a synergistic effect, while a negative sign indicates an antagonistic effect. The negative coefficients of X_1 and X_2 in both the models refer to the decreasing amount of drug release as the concentration of chitosan and concentration of glutaraldehyde increases. Similarly, the positive coefficients of X_3 and X_4 indicate the increase in drug release with increasing concentration of drug and response time.

In order to check the reliability of the models to predict drug release response four more experiments, consisting of different values of variables (X_1, X_2, X_3 and X_4) other than the design values, are conducted. The theoretical values of drug release are calculated using Equations (2) and (3). The theoretical and experimental values of drug release are compared and are shown in Table 4. Comparison of experimental and calculated values of drug release response shows that the predicted models are in reasonably good agreement with experimental data, outside the design values. Table 5 presents the ANOVA demonstrating that the model is significant. The probability values, $P< 0.0001$ in ANOVA, indicate significant effect of model on drug release response.

Figure 4 indicates the effect of concentration of chitosan, X_1 and percentage of glutaraldehyde, X_2

Table 4. Comparison of the calculated and experimental response values for the formulations other than the design values

Chitosan [g]	Glutaraldehyde (10 ml) [%]	Drug (CPM) [mg]	Response time [hrs]	Calculated response ($\cdot 10^{-4}$) [g/ml]		Experimental response ($\cdot 10^{-4}$) [g/ml]		Absolute error
(X_1)	(X_2)	(X_3)	(X_4)	Y(2)	Y(7.4)	Y(2)	Y(7.4)	
0.1	6.25	100	3	–	8.45	–	8.49	0.04
0.3	0	100	5	–	9.99	–	9.91	–0.08
0.3	6.25	25	5	7.35	–	7.34	–	–0.01
0.3	18.8	100	6	7.83	–	7.85	–	0.02

Table 5. Summary of results in analyzing lack of fit (LOF)

ANOVA for response surface quadratic model (drug release in pH = 2.0)					
Source	**Sum of squares**	**DF**	**Mean square**	**F value**	**P**
Model	11.12	14	0.794	13.584	< 0.0001
Residual	0.87684	15	0.05846		
Lack of fit	0.87634	10	0.08763	8.636	
Pure error	0.00051	5	0.0001		
Cor total	11.9936	29			
ANOVA for response surface quadratic model (drug release in pH = 7.4)					
Source	**Sum of squares**	**DF**	**Mean square**	**F value**	**P**
Model	9.34	14	0.667	11.485	< 0.0001
Residual	0.87092	15	0.05806		
Lack of fit	0.86989	10	0.08698	4.209	
Pure error	0.00103	5	0.00020		
Cor total	10.2067	29			

on drug release in acidic $Y(2)$ and basic $Y(7.4)$ media. In acidic medium, the drug release varies in a nonlinear manner, but in a descending pattern with an increase in concentration of chitosan and percentage of crosslinker as shown in Figure 4a. The contour plot shows that percentage of crosslinker has a comparatively greater influence on the drug release variable than concentration of chitosan. 'Saddle' point is observed at $X_1 = 0.42$ g and $X_2 = 18.8\%$. Figure 4b indicates the effect of simultaneous change in concentration of chitosan and crosslinker on the drug release in basic medium (pH 7.4). In our previous studies [9] on drug release from crosslinked chitosan-alanine beads, it is observed that the drug release in basic medium is higher than in acidic medium. It is also observed that at fixed concentration of crosslinker, the drug release increases with an increase in chitosan concentration, reaches a maxima, followed by its decrease. The drug release response increases to 'peak' maxima ($> 9.0 \cdot 10^{-4}$ g/ml) at the intermediate value of concentration of chitosan (0.42 g) and at somewhat higher concentration of crosslinker (15.5%). This may be due to the fact that a high concentration of chitosan results in a denser matrix, which causes reduced degree of swelling of beads. Consequently, the process of diffusion is slowed

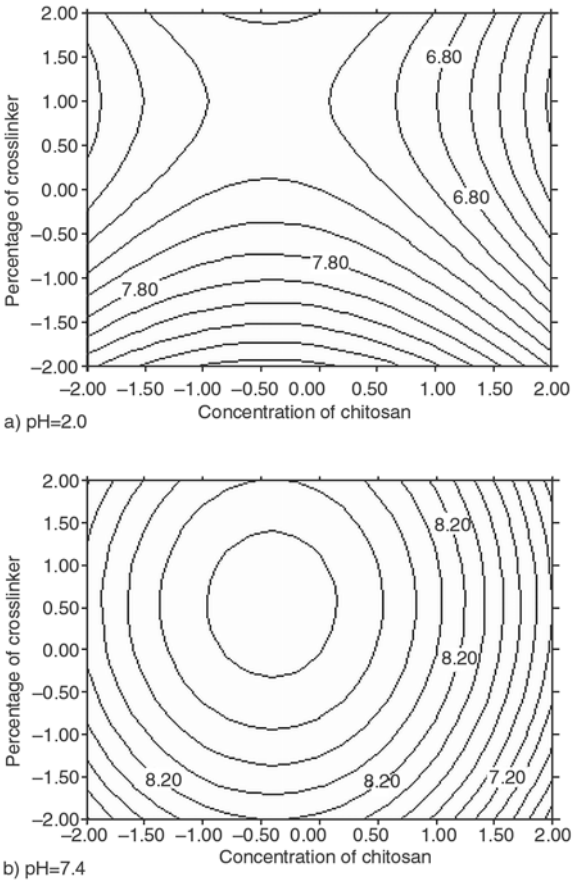

Figure 4. Contour plots (2D) showing the influence of concentration of chitosan (X_1) and concentration of glutaraldehyde (X_2) on drug release a) $Y(2)$, b) $Y(7.4)$ for pH 2 and pH 7.4, respectively

down due to the decreased level of penetration of solvent, which leads to decreased release of drug. Bayomi *et al*. [1], Genta *et al*. [2] and Acikgöz *et al*. [23] also observed that there is a significant increase in drug release, when a more porous matrix having low concentration of chitosan was used.

The effects of concentration of chitosan, X_1 and concentration of drug, X_3 on drug release in acidic $Y(2)$ and basic $Y(7.4)$ media are plotted as contour and shown in Figure 5. The amount of drug release increases with the drug concentration in beads at fixed level of chitosan concentration. The drug release is maximum at nearly intermediate value of concentration of chitosan, $X_1 = 0.42$ g and a 'rising ridge' is observed corresponding to this point. According to Gupta and Kumar [7] and Kumar and Gupta [8], the total amount of drug released from the beads loaded with a higher concentration of drug is found to be higher in comparison to the beads loaded with a lower amount of CPM. At the higher level of concentration of chitosan, the concentration of alanine is less. As a result of which, the intermediate space between the different layers of matrix is less causing lesser degree of swelling and hence, the amount of drug release is minimum. Figure 5b indicates that the drug release response is similar, but higher in basic medium as compared to drug release in acidic medium. Response to drug release increases to 'peak' maxima ($> 9.2 \cdot 10^{-4}$ g/ml) corresponding to concentration of chitosan, $X_1 = 0.42$ g and concentration of drug, $X_2 = 100$ mg.

Figure 6 illustrates the effect of concentration of chitosan, X_1 and response time, X_4 on drug release. The response time has the similar effect on drug release in acidic and basic media. In both the cases $Y(2)$ and $Y(7.4)$, the 'rising ridge' is observed corresponding to concentration of chitosan, $X_1 = 0.42$ g, similar to the studied effect of concentration of chitosan, X_1 and concentration of drug, X_3 on drug release in acidic medium $Y(2)$ in Figure 4a. At the

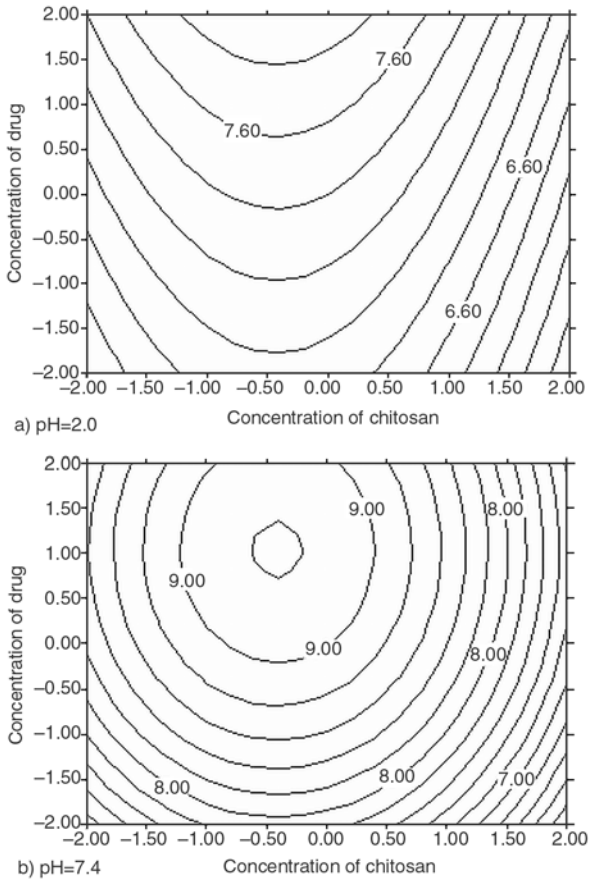

Figure 5. Contour plots (2D) showing the influence of concentration of chitosan (X_1) and concentration of drug (X_3) on drug release a) $Y(2)$, b) $Y(7.4)$ for pH 2 and pH 7.4, respectively

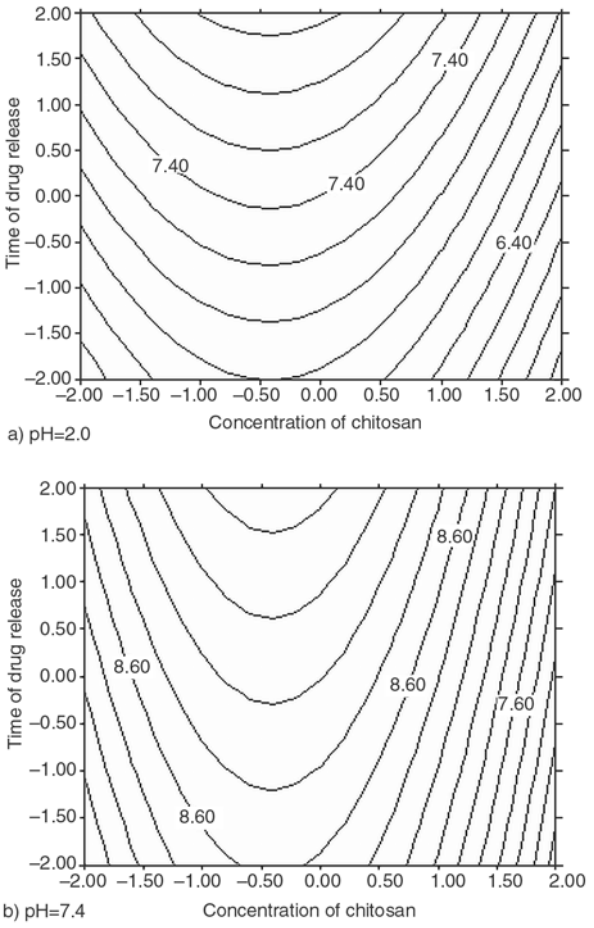

Figure 6. Contour plots (2D) showing the influence of concentration of chitosan (X_1) and response time (X_4) on drug release a) $Y(2)$, b) $Y(7.4)$ for pH 2 and pH 7.4, respectively

intermediate values of drug release time, the drug release in acidic medium $Y(2) = 7.45 \cdot 10^{-4}$ g/ml and in basic medium $Y(7.4) = 9.07 \cdot 10^{-4}$ g/ml. It is further observed that the effect of response time is more in acidic medium than in basic medium at fixed level of concentration of chitosan.

The effects of concentration of crosslinker, X_2 and concentration of drug, X_3 on drug release are depicted in Figure 7. Minimum drug release is found to be lying between the percentage of glutaraldehyde 9.8–20%, corresponding to lower range of concentration of drug i.e. 0–41 mg. At the lower values of percentage of crosslinker, the drug release $Y(2)$ increases linearly with the concentration of drug. The nature of response behavior changes to non-linear at higher concentration of crosslinker. Figure 7b observes the 'region of maxima' i.e. $9.4 \cdot 10^{-4}$ g/ml for the drug release lying between the high level of concentration of drug (100 mg) and low level of crosslinker (approximately 3%). At the lower values of drug load, the release of drug decreases linearly with an increase in the percentage of crosslinker. The nature of drug release behavior changes from linear to nonlinear at the intermediate and higher values of drug load. The effect of concentration of drug seems to be more pronounced as compared with that of crosslinker.

Figure 8 describes the effect of percentage of crosslinker, X_2 and response time, X_4 on drug release. Contour plots in Figure 8a show the 'region of minimum' for concentration of the released drug. The amount of drug release is minimum ($6.6 \cdot 10^{-4}$ g/ml) at higher values of glutaraldehyde (18.8%) and at initial response time. At the fixed response time, as the concentration of glutaraldehyde decreases, the response behavior changes to linear. In Figure 8b, drug release decreases linearly with percentage of crosslinker. As the percentage of crosslinker increases, the penetration of solvent in to the matrix becomes difficult. Thus, the degree of swelling decreases, result-

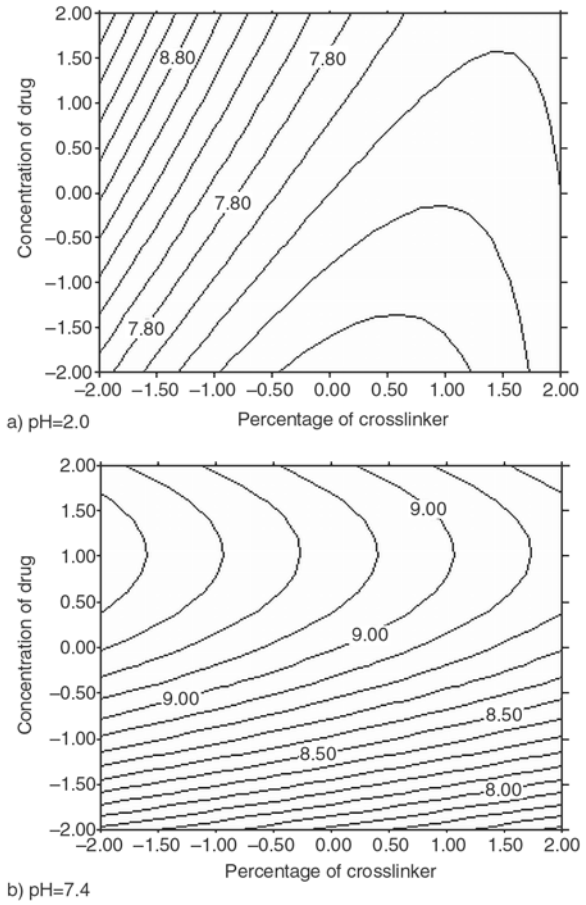

Figure 7. Contour plots (2D) showing the influence of concentration glutaraldehyde (X_2) and concentration of drug (X_3) on drug release a) $Y(2)$, b) $Y(7.4)$ for pH 2 and pH 7.4, respectively

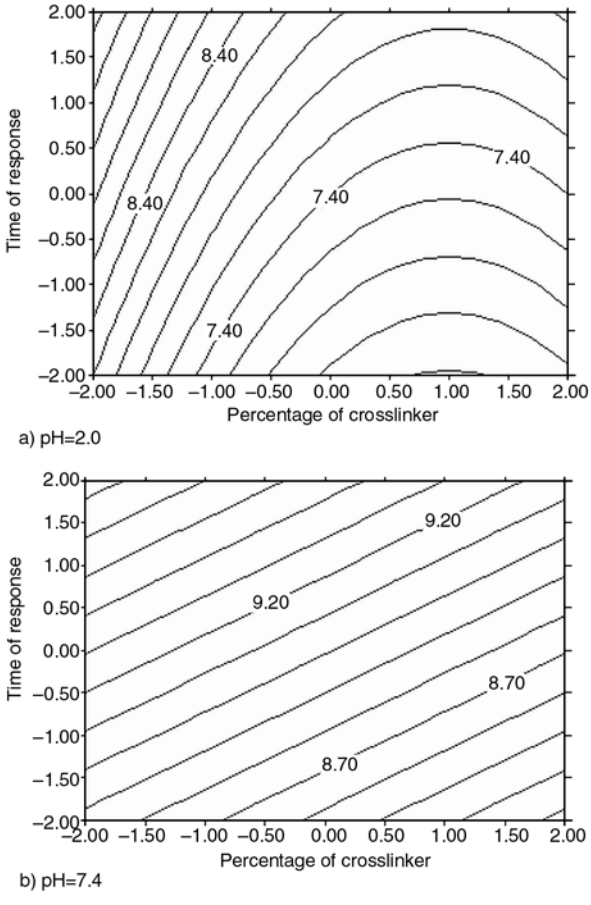

Figure 8. Contour plots (2D) showing the influence of concentration glutaraldehyde (X_2) and response time (X_4) on drug release a) $Y(2)$, b) $Y(7.4)$ for pH 2 and pH 7.4, respectively

ing in decreased rate of drug release. At the fixed value of crosslinker, as the response time increases, the drug release increases linearly because swelling is function of time.

The effects of concentration of drug, X_3 and response time, X_4 on drug release are shown in Figure 9. In Figure 9a, the drug release response surface is 'hillside' and varies in linear fashion with increasing concentration of drug as well as response time in acidic medium. However, the effect of response time seems to be more effective as compared to that of drug concentration. The maximum amount of drug release is $8.4 \cdot 10^{-4}$ g/ml at the higher values of concentration of drug and response time. In the basic medium, the drug release response is a linear function for the early values of concentration of drug and at all the values of response time as shown in Figure 9b. The response behavior becomes non linear at the higher values of concentration of drug.

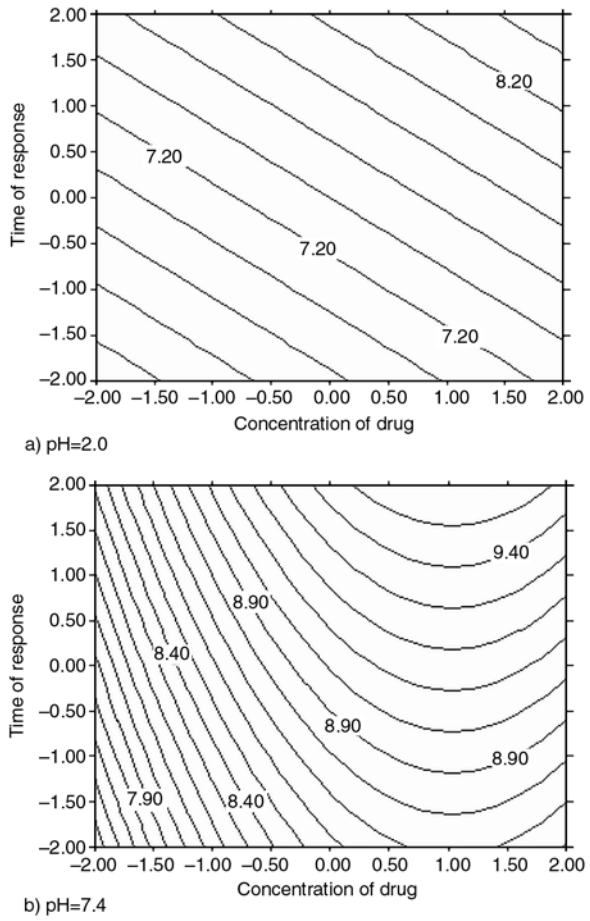

Figure 9. Contour plots (2D) showing the influence of concentration of drug (X_3) and response time (X_4) on drug release a) $Y(2)$, b) $Y(7.4)$ for pH 2 and pH 7.4, respectively

Figure 10 shows a linear correlation plots between the actual and predicted response variables. The linear correlation plots drawn between actual and predicted responses demonstrate reasonable values of R^2 (i.e. for $Y(2)$ $R^2 = 0.927$ and for $Y(7.4)$ $R^2 = 0.915$). The R-square (correlation coefficient) value provides a measure of how much of the variability in the observed response values can be explained by the experimental factors and their interactions. A good model explains most of the variations in the response. The closer the value of R-square to 1.0, the stronger the model and the better are the response predictions. Hence, high values of R-square indicate significant lack of fit ($P < 0.0001$) in both the cases.

The residual plots showing homogeneity of data for drug release are plotted in Figure 11. All the experimental data points are uniformly distributed around the mean of response variable showing the scatter of the residuals versus actual response values.

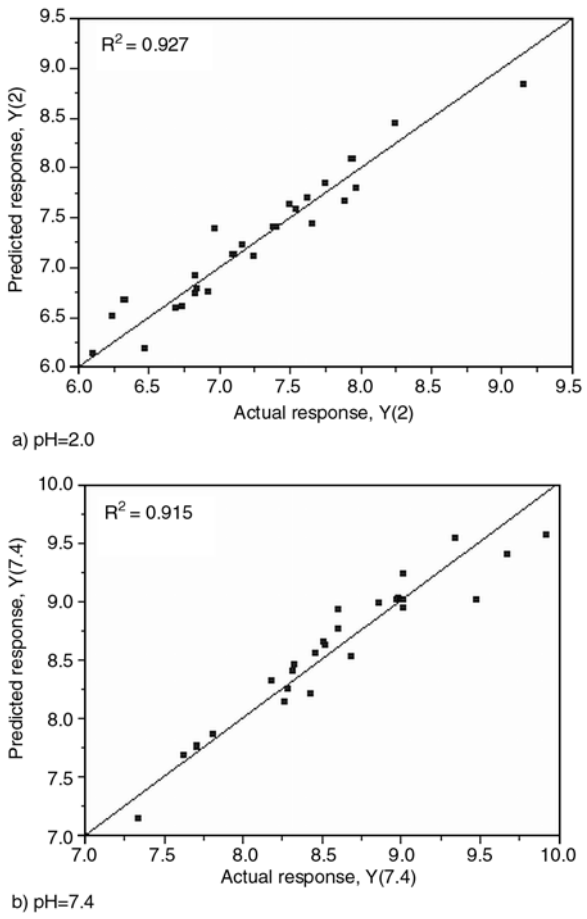

Figure 10. Linear correlation plots between actual and predicted response a) $Y(2)$, b) $Y(7.4)$ for pH 2 and pH 7.4, respectively

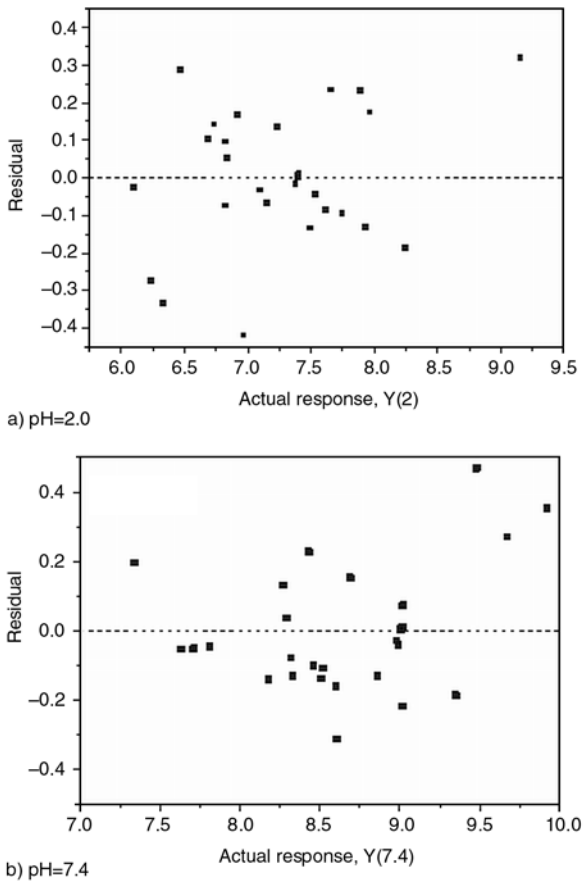

Figure 11. Response surface plots for drug release response a) $Y(2)$, b) $Y(7.4)$ for pH 2 and pH 7.4, respectively

4. Conclusions

Optimization of drug release from chitosan-alanine crosslinked beads using RSM, central composite design, is performed. On the basis of analysis of variance (ANOVA), a second order model is established, describing the effect of the amount of chitosan (X_1), the percentage of crosslinker i.e. glutaraldehyde (X_2), the concentration of drug loading (X_3) and the time of drug release (X_4) on drug release response. The data obtained, based on designed formulations, is fitted in second order model for drug release in acidic and basic media. Both the polynomials are found to be statistically significant ($P< 0.0001$), as determined by ANOVA. It is observed from the probability data of both the models that the probability values of the coefficients of X_1, X_2, X_3 and X_4 are less than 0.1, which is a significant value. It implies that all the four independent variables have great influence on the drug release response. ANOVA is used to evaluate the adequacy of the fitted model. The prediction from the model and the experimental results in this study conform to each other quite well, indicating the validity of the model. The obtained equations are plotted as contour. The increase in percentage of crosslinker and concentration of chitosan reduces the drug release response due to the formation of highly dense matrix. From the data obtained and contour plots, it may be concluded that the concentration of alanine has tremendous effect on the swelling and drug release properties of the matrix. As the concentration of alanine (which acts as spacer) increases, the density of the matrix decreases resulting in an increase in drug release. In all the cases, the drug release is maximum for chitosan concentration, $X_1 = 0.42$ g (Figures 4–6). The optimum drug level that can be loaded into the matrix corresponding to maximum drug release in basic medium is 100 mg (Figures 5b, 7b and 9b). It is observed that the concentration of drug has pronounced effect on drug release as compared to the concentration of crosslinker. For the predicted models, the range of percentage of glutaraldehyde for optimum drug release is 10–18% (Figures 4 and 8a). In general, the response time has shown a linear effect on drug release. As the response time increases, the percentage of swelling of the matrix increases and hence, the drug release increases linearly. It can be concluded that the response surface methodology (RSM) can be successfully used to optimize the drug release from chitosan–alanine crosslinked beads loaded with CPM.

References

[1] Bayomi M. A., Al-Suwayeh S. A., El-Helw A. M., Mesnad A. F.: Preparation of casein-chitosan microspheres containing diltiazem hydrochloride by an aqueous coacervation technique. Pharmaceutica Acta Helvetiae, **73**, 187–192 (1998).
DOI: 10.1016/S0031-6865(98)00020-X

[2] Genta I., Costatini M., Asti A., Conti B., Montanari L.: Influence of glutaraldehyde on drug release and mucoadhesive properties of chitosan microspheres. Carbohydrate Polymers, **36,** 81–88 (1998).
DOI: 10.1016/S0144-8617(98)00022-8

[3] Mi F-L., Shyu S-S., Kuan C-Y., Lee S-T., Lu K-T., Jang S-F.: Chitosan-polyelectrolyte complexation for the preparation of gel beads and controlled release of anticancer drug. I. Effect of phosphorous polyelectrolyte complex and enzymatic hydrolysis of polymer. Journal of Applied Polymer Science, **74**, 1868–1879 (1999).
DOI: 10.1002/(SICI)1097-4628(19991114)74:7<1868::AID-APP32>3.0.CO;2-N

[4] Martínez-Ruvalcaba A., Sánchez-Díaz J. C., Becerra F., Cruz-Barba L. E., González-Álvarez A.: Swelling characterization and drug delivery kinetics of polyacrylamide-co-itaconic acid/chitosan hydrogels. Express Polymer Letters, **3**, 25–32 (2009).
DOI: 10.3144/expresspolymlett.2009.5

[5] Tiwari A., Singh V.: Synthesis and characterization of electrical conducting chitosan-graft-polyaniline. Express Polymer Letters, **1**, 308–317 (2007).
DOI: 10.3144/expresspolymlett.2007.44

[6] Goosen M. F. A.: Applications and properties of chitosan in applications of chitin and chitosan. Technomic Publishing Company, Lancaster (1997).

[7] Gupta K. C., Kumar M. N. V. R.: Studies on semi-interpenetrating polymer network beads of chitosan-poly (ethylene glycol) for controlled release of drugs. Journal of Applied Polymer Science, **80**, 639–649 (2001).
DOI: 10.1002/1097-4628(20010425)80:4<639::AID-APP1140>3.0.CO;2-O

[8] Gupta K. C., Kumar M. N. V. R.: Semi-interpenetrating polymer network beads of crosslinked chitosan-glycine for controlled release of chlorpheniramine maleate. Journal of Applied Polymer Science, **76**, 672–683 (2002).
DOI: 10.1002/(SICI)1097-4628(20000502)76:5<672::AID-APP9>3.0.CO;2-F

[9] Kumari K., Kundu P. P.: Semiinterpenetrating polymer networks of chitosan and L-alanine for monitoring the release of chlorphenramine maleate. Journal of Applied Polymer Science, **103**, 3751–3757 (2007).
DOI: 10.1002/app.25432

[10] Kumari K., Kundu P. P.: Studies on *in vitro* release of CPM from semi-interpenetrating polymer network (IPN) composed of chitosan and glutamic acid. Bulletin of Materials Science, **31**, 159–167 (2008).
DOI: 10.1007/s12034-008-0028-y

[11] Kumari K., Raina K. K.,. Kundu P. P.: Studies on the cure kinetics of chitosan-glutamic acid using glutaraldehyde as crosslinker through differential scanning calorimeter. Journal of Applied Polymer Science, **108**, 681–688 (2008).
DOI: 10.1002/app.27695

[12] Myers R. H., Montgomery D. C.: Response surface methodology: Process and product optimization using designed experiments. Wiley, New York (1995).

[13] Singh B., Dahiya M., Saharan V., Ahuja N.: Optimizing drug delivery systems using systematic 'design of experiments'. Part II: Retrospect and prospects. Critical Reviews in Therapeutic Drug Carrier Systems, **22**, 215–293 (2005).
DOI: 10.1615/CritRevTherDrugCarrierSyst.v22.i3.10

[14] Singh B., Mehta G., Kumar R., Bhatia A., Ahuja N., Katare O. P.: Design, development and optimization of nimesulide-loaded liposomal systems for topical application. Current Drug Delivery, **2**, 143–153 (2005).
DOI: 10.2174/1567201053585985

[15] Aberturas M. R., Molpeceres J., Guzmán M., García F.: Development of a new cyclosporine formulation based on poly(caprolactone) microspheres. Journal of Microencapsulation, **19**, 61–72 (2002).
DOI: 10.1080/02652040110055270

[16] Lewis G. A., Mathieu D., Phan-Tan-Luu R.: Pharmaceutical experimental design. Marcel Dekker, New York (1999).

[17] Singh B., Ahuja N.: Response surface optimization of drug delivery system. in 'Progress in controlled and novel drug delivery systems' (ed.: Jain N. K.) CBS Publishers and Distributors, New Delhi (2004).

[18] Kincl M., Turk S., Vrecer F.: Application of experimental design methodology in development and optimization of drug release method. International Journal of Pharmaceutics, **291**, 39–49 (2005).

[19] Ko J. A., Park H. J., Park Y. S., Hwang S. J., Park J. B.: Chitosan microparticle preparation for controlled drug release by response surface methodology. Journal of Microencapsulation, **20**, 791–797 (2003).

[20] Kukreja T. R., Kumar D., Prasad K., Chauhan R. C., Choe S., Kundu P. P.: Optimization of physical and mechanical properties of rubber compounds by response surface methodology – Two component modeling using vegitable oil and carbon black. European Polymer Journal, **38**, 1417–1422 (2002).
DOI: 10.1016/S0014-3057(02)00005-8

[21] Turkoglu M., Sakr A.: Mathematical modeling and optimization of a rotary fluidized-bed coating process. International Journal of Pharmaceutics, **88**, 75–87 (1992).
DOI: 10.1016/0378-5173(92)90305-L

[22] Wu C. F. J., Hamada M.: Experiments planning, analysis, and parameter design optimization. Wiley, New York (2000).

[23] Açikgöz M., Kaş H. S., Orman M., Honcal A. A.: Chitosan microspheres of diclofenac sodium: I. Application of factorial design and evaluation of release kinetics. Journal of Microencapsulation, **13**, 141–160 (1996).
DOI: 10.3109/02652049609052903

eXPRESS Polymer Letters Vol.3, No.4 (2009) 219–225
Available online at www.expresspolymlett.com
DOI: 10.3144/expresspolymlett.2009.28

New fluorescent polymeric nanocomposites synthesized by antimony dodecyl-mercaptide thermolysis in polymer

F. Capezzuto[1], G. Carotenuto[1], F. Antolini[2], E. Burresi[2], M. Palomba[1], P. Perlo[3]*

[1]Institute of Composite and Biomedical Materials, P.le Tecchio, 80 – 80125 Napoli, Italy
[2]ENEA Research Center of Faenza, Dept. of Advanced Physical Technologies and New Materials Via Ravegnana 186 – 48018 Faenza (Ra), Italy
[3]FIAT Research Center, Strada Torino 50 – 10043 Orbassano (TO), Italy

Received 5 January 2009; accepted in revised form 21 February 2009

Abstract. In this work, the formation of semiconductive Sb_2S_3 nanoparticles inside amorphous polystyrene has been achieved by thermal degradation of the corresponding antimony dodecyl-mercaptide, $Sb(SC_{12}H_{25})_3$. The thermolysis of the dodecyl-mercaptide precursor was studied as both pure phase and mercaptide solution in polystyrene. The thermal decomposition of the antimony mercaptide precursor at 350°C, under vacuum, showed the formation of a mixture of antimony trisulfide (stibnite, Sb_2S_3) and zero-valent antimony (Sb) phase. X-ray Powder Diffraction (XRD) and Rietveld analysis carried out on the obtained nanostructured powder confirmed the presence of Sb and Sb_2S_3 phases in 10.4 wt% and 89.6 wt% amount, respectively. The same pyrolysis reaction was carried out in the polymer and the resulting nanocomposite material was characterized by X-ray diffraction (XRD), transmission electron microscopy (TEM), UV-VIS spectroscopy, and fluorescence spectroscopy. The nanocomposite structural characterization indicated the presence of well-dispersed nanoclusters of antimony and stibnite (15–30 nm in size) inside the amorphous polymeric phase. Optical measurements on the obtained nanocomposite films showed a strong emission at 432 nm upon excitation at 371 nm, probably related to the presence of Sb_2S_3 nanoclusters.

Keywords: *nanocomposites, stibnite, antimony, mercaptide, fluorescence*

1. Introduction

Polymer nanocomposites made of nanoparticles (spheres, rods, plates, etc.) embedded into a polymeric matrix extend the potentialities of polymers while maintaining the manufacturing and processing flexibility inherent to plastics [1–6]. In fact, the potential impact of polymeric nanocomposite materials lies in the synergistic combination of nanoparticles and polymers properties that can lead not only to the sum of the organic and inorganic phase characteristics, but also to new functionalities with respect to the single materials [6–9]. The advantages of these materials arise mainly from the filler size reduction to nanoscale, considering that the concomitant quantum confinement effects induce new physical phenomena [10, 11]. In fact, nanoparticles have unique optical and electronic properties not observed in the corresponding bulk materials [12, 13].

As already said, it is well known that the embedding of nanoscale fillers into a polymeric matrix offers the possibility to achieve materials with properties combination not realizable by the single components. In particular, the combination of fluorescent semiconductor nanoparticles with optical polymers yields to a new class of materials characterised by both fluorescence and transparency characteristics. The luminescent properties of semicon-

*Corresponding author, e-mail: giancaro@unina.it

ductor nanoparticles stem from the separation of the conductive and valence band due to the quantum-size effect. Nowadays, the luminescent properties of semiconductor nanoparticles are thoroughly studied for the development of new labelling systems for biomedical purposes [14] and for light-emitting devices applications [15–17]. Especially in the last case, the combination of nanoparticles and polymers is of special interest because the mechanical and electro-optical properties of polymers joined with the high stability of nanoparticles as light-emitters allow the set-up of industrially competitive systems for light-source production.

Antimony trisulfide, Sb_2S_3 is an interesting material, with unique optical properties and currently under study as potential photovoltaic material [18, 19]. Sb_2S_3 is a semiconductor which has been also studied for its high photosensitivity and thermoelectric power [20]. It has been used in television cameras with photoconducting targets, microwave devices, thermoelectric, electronic and optical devices, as well as in infrared (IR) spectroscopy [21]. The optical properties of the Sb-Sb_2S_3 system were studied by fluorimetry since this material shows photoluminescence characteristics [22]. In addition, sphere-like nanomaterials have excellent optical, physical and chemical properties that could be widely applied in biology, as fluorescence probes [23–25].

In this work, the synthesis of luminescent stibnite-antimony, Sb_2S_3-Sb, nanoparticles embedded into a polymer matrix, by thermolysis of antimony dodecyl-mercaptide, $Sb(SC_{12}H_{25})_3$, dissolved in polymer is reported. It has been shown that the thermal decomposition of mercaptides is a powerful synthesis method for a number of noble metals, semimetals and metal sulphide [26]. Sb_2S_3 nanomaterials can be synthesised by several methods namely hydrothermal method, refluxing polyol process, or in solution at room temperature, however the proposed synthesis allows the material preparation at quite mild temperature conditions (150–250°C), absolutely compatible with the thermal stability of common polymers. Here, the structural and morphological characteristics of the $Sb(SC_{12}H_{25})_3$ thermolysis product and the luminescent behaviour of the Sb_2S_3-Sb/polystyrene system are given.

2. Experimental

Antimony dodecyl-mercaptide, $Sb(SC_{12}H_{25})_3$, was prepared by adding drop-by-drop an alcoholic solution of dodecanethiol, $C_{12}H_{25}SH$ (Aldrich), to an antimony chloride solution, $SbCl_3$ (Aldrich, 99.9%) in ethanol (Fluka, 99.8%) at room-temperature, under stirring (see Equation (1)) [27]. Stoichiometric amounts of reactants were used. The mercaptide precipitation did not take place after reactants mixing, but a pH correction, by addition of ammonium hydroxide, $NH_3{\cdot}H_2O$ (Aldrich) was required (see Equation (2)). The mercaptide promptly precipitated in form of a white crystalline powder, which was separated by vacuum-filtration and then washed several times with ethanol. The antimony dodecyl-mercaptide was further purified from the NH_4Cl by-product by dissolution in chloroform followed by filtration and solvent evaporation (Equations (1) and (2)):

$$SbCl_3 + 3C_{12}H_{25}SH \rightleftharpoons Sb(SC_{12}H_{25})_3 + 3HCl \quad (1)$$

$$HCl + NH_4OH \rightarrow NH_4Cl + H_2O \quad (2)$$

The thermal decomposition of the obtained antimony dodecyl-mercaptide at 350°C, under vacuum (2 mbar), by using a hotplate, is expected to give an inorganic product made of a mixture of stibnite, Sb_2S_3, and antimony, Sb, powders. A preliminary study of the mercaptide thermal degradation has been carried out by Differential Scanning Calorimetry (DSC-TA Instruments 2920) from room-temperature to 150°C, at 10°C/min, under fluxing nitrogen, using sealed aluminium capsules. From the DSC and X-ray Powder Diffraction analysis of the inorganic powder product of the antimony dodecyl-mercaptide pyrolysis, it results that the processes developed during the thermal treatment took place in the following steps: (i) mercaptide melting at ca. 50°C, (ii) mercaptide decomposition to nanometric antimony (Sb) and antimony sulfide (Sb_2S_3) at ca. 150°C, and (ii) evaporation of the organic by-products, which refluxed inside the flask at ca. 300°C. After cooling down at room temperature, the inorganic phase was washed by chloroform and separated by centrifugation at 8000 rpm for 10 minutes.

In order to obtain stibnite-antimony/polystyrene nanocomposite films, $Sb(SC_{12}H_{25})_3$ was dissolved in chloroform and mixed with a chloroform solution of polystyrene (Aldrich, molecular weight

M_w = 230 000 gmol^{-1}). $Sb(SC_{12}H_{25})_3$/polystyrene blend consisting of 5% by weight of mercaptide component was prepared. The obtained system was cast onto a glass-substrate and allowed to dry at room temperature. The thermal annealing of the obtained $Sb(SC_{12}H_{25})_3$/polystyrene blend was performed at ca. 250°C, using a hot-plate, and it led to stibnite-antimony/polystyrene nanocomposite film. Both powder and nanocomposite films were investigated by X-ray Powder Diffraction (XRD). The Sb_2S_3-Sb powder (hand ground in an agate mortar) was loaded in an aluminium flat holder and the X-ray data were collected using a Philips conventional Bragg-Brentano vertical diffractometer with Cu-K_α radiation. The investigated 2Θ range was 5–80° in steps of 0.02° and 8 s per step. The phase identification was carried out by means of X' pert High Score software (data base ICDD PDF2 Sets 1-82). The observed data were refined with GSAS (Larson and Von Dreele). The nanocomposite film was investigated in the 2Θ range from 5 to 80° with a step size of 0.02° and 1 s per step by means of a Rigaku DMAX-IIIC, using Cu-K_α radiation, λ = 1.5418 Å.

The morphology of the Sb_2S_3-Sb powder mixture was examined by Scanning Electron Microscopy (SEM, Cambrige-S360) and the $Sb(SC_{12}H_{25})_3$/polystyrene nanocomposite film was investigated by Transmission Electron Microscopy (Philips EM208S microscope equipped with a MegaView Camera for digital imaging, using an accelerating voltage of 100 kV) and photoluminescence spectroscopy (Perkin-Elmer-LS55 spectrofluorometer using a pulsed xenon lamp as an excitation source). TEM specimens were prepared by dissolution of the nanocomposite material in chloroform and the obtained solution was cast on graphitized film supported on copper mesh grids.

3. Results and discussion

The DSC thermogram of pure $Sb(SC_{12}H_{25})_3$ shows an endothermic peak at 48°C, corresponding to the antimony dodecyl-mercaptide melting point. The nature of the inorganic products resulting from $Sb(SC_{12}H_{25})_3$ pyrolysis was investigated by X-ray Powder Diffraction (see Figure 1). In order to obtain an accurate and quantitative phase analysis, a Rietveld refinement was performed. Two main phases were identified: stibnite (Sb_2S_3, reference pattern N° 01-073-0393 crystal system Orthorhombic, space group Pnma, crystal lattice parameters a = 11.3107 Å, b = 3.8363 Å, c = 11.2285 Å, V = 487.22 Å^3) and antimony (Sb, reference pattern N° 01-085-1324, crystal system Rhombohedral, space group R-3m, crystal lattice parameters a = 4.3007 Å, b = 4.3007 Å, c = 11.2220 Å, V = 179.75 Å^3). A preliminary quantization of the two component amounts in the investigated powder mixture, carried out using the RIR ratio, displays 95 wt% stibnite and 5 wt% antimony. However, a more sophisticate phase quantization was carried out by using the Rietveld method with the GSAS program. The final agreement factors of the Rietveld refinement for the investigated stibnite/antimony mixture are R_{wp} = 16.7%, R_p = 12.9% and χ^2 = 1.6, with a phase estimation of 10.4 wt% Sb and 89.6 wt% Sb_2S_3. The refinement lattice parameters of these phases are: stibnite a = 11.3103 Å, b = 3.8367 Å, c = 11.2289 Å, V = 487.27 Å^3 and antimony a = 4.3073 Å, b = 4.3073 Å, c = 11.2752 Å, V = 181.16 Å^3. The result of the Rietveld method was obtained refining the background, both cells, profiles, intensities and orientation. As it can be seen, the calculated lattice crystal parameters of stibnite are in good agreement with the observed one, while the calculated lattice parameters of antimony are slightly higher with respect to the expected ones. Both methods show

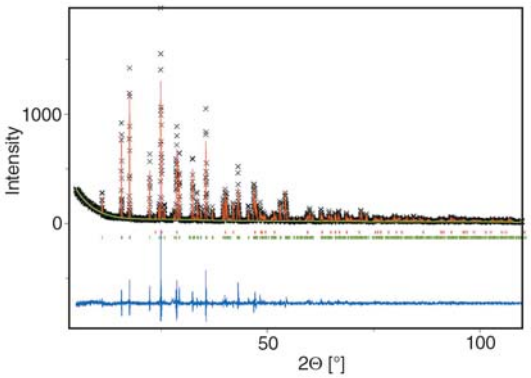

Figure 1. XRD pattern of the inorganic powder resulting from the $Sb(SC_{12}H_{25})_3$ thermolysis at 350°C, under vacuum. The observed and calculated XRD patterns are reported as black cross and red line. The difference between the calculated and experimental spectra is reported as a blue line. The red bars are the peak's markers of the antimony while the green bars represent the stibnite.

a)

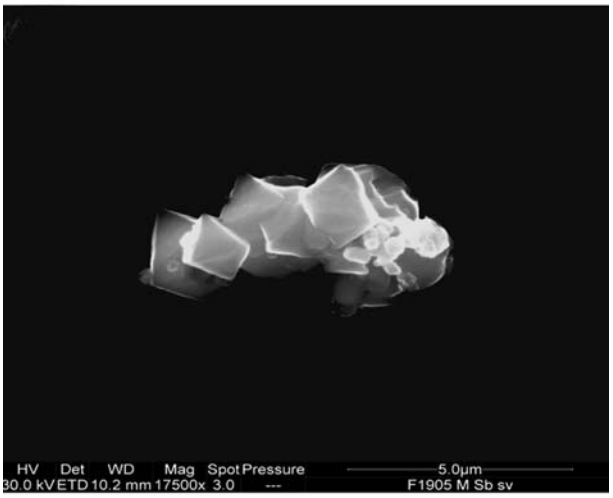

b)

Figure 2. Representative SEM micrograph of the powder product resulting from the $Sb(SC_{12}H_{25})_3$ thermolysis at 350°C, under vacuum: a) Sb_2S_3 prismatic crystals and b) Sb polyhedral crystals

that stibnite is the main phase, while the antimony is present only in small amount.

The SEM-micrograph of the inorganic phase Sb_2S_3/Sb (see Figure 2) shows two different solid phases: one, made of prismatic shaped crystals, corresponding to stibnite (Figure 2a) and the other one, made of aggregated polyhedral crystals, corresponding to zero-valent antimony (Figure 2b). The crystals size was evaluated from the SEM micrographies by image analysis using Sigma Scan Pro 5.0 and gave the following information: the prismatic stibnite crystals have a length ranging from 30 to 150 µm and ca. 10–20 µm in diameter, while the polyhedral antimony crystals have an average size of 2–3 µm.

After this preliminary study of pure antimony dodecyl-mercaptide thermal degradation, the mercaptide decomposition in polymer has also been investigated. The XRD pattern of stibnite-antimony/polystyrene nanocomposite film (see Figure 3) shows a broad reflection at ca. 20°, corresponding to the diffuse alone of amorphous polymer matrix and different peaks belonging to diffraction patterns of the inorganic nanostructured phase. The phase analysis of dodecyl-mercaptide decomposed in polystyrene allows the identification of two main phases: stibnite (Sb_2S_3, reference pattern N° 01-073-0393) and antimony (Sb, reference pattern N° 01-085-1324), just like in the case of pure dodecyl-mercaptide thermal decomposition.

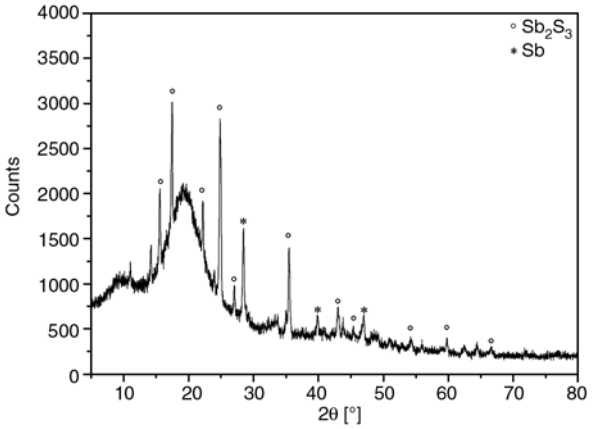

Figure 3. XRD pattern of the $Sb(SC_{12}H_{25})_3$/polystyrene blend thermally treated at 250°C

A representative TEM micrograph of the stibnite-antimony/polystyrene system is shown in Figure 4. TEM samples were prepared by dissolving 100 mg of nanocomposite in 20 ml of chloroform. A drop of the resulting solution was placed onto TEM copper grid support. As visible, the average size of the

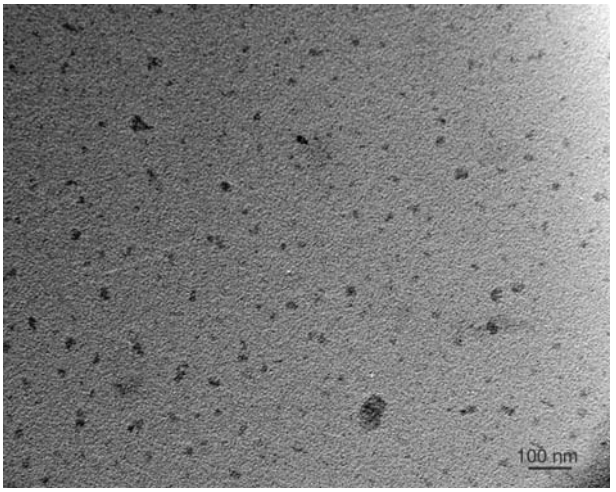

Figure 4. Typical TEM micrograph of the $Sb(SC_{12}H_{25})_3$/polystyrene thermally treated at 250°C

inorganic nanocrystals (stibnite and antimony clusters) was of ca. 15–30 nm.

The photoluminescence spectra of the nanocomposite antimony-stibnite/polystyrene films are shown in Figure 5. It can be seen that the excitation and emission peaks are shifted to higher wavelength values with respect to the corresponding peaks of the used pure polystyrene which exhibits a maximum of emission band at 389 nm for a maximum excitation at 296 nm. In fact, the emission band peak of the stibnite-antimony/polystyrene system appeared at 432 nm when excited at 371 nm which is the maximum of the absorption spectrum (see Figure 5). These spectra show a shape similar, to that of organic luminescent dyes, because the excitation and emission spectra result quite symmetric (mirror-like shaped peaks) [14]. This feature is rarely observed with nanoparticles, since nanocrystals usually exhibit a broad absorption with a narrow symmetric photoluminescence spectra (full-width at half maximum of 25–40 nm) [14]. The presence of the tail in the emission spectrum of the nanocomposite can be explained by taking into account the size distribution and the not uniform shape of the nanoparticles inside the polymer producing different emission spectra. As reported by other authors [28–30], the presence of surface traps, that modulates the emission of nanocrystals, should be also taken into consideration.

In order to exclude that the photoluminescence signal was related to the polystyrene presence, the emission spectrum of the nanocomposite was recorded at 296 nm, i.e. the excitation wavelength typical of polystyrene. As a result this experiment gives an emission signal with a maximum at 424 nm (data not shown). This photoluminescence band shows a lower intensity and a shift of the maximum with respect to the band of the nanocomposite obtained with λ_{exc} = 371 nm, excluding a possible role of the polystyrene matrix in the nanocomposite material photoluminescence. In addition, the approximate value of the nanocomposite energy band-gap ($E_g = hc/\lambda_{em}$) has been evaluated from the maximum emission peak wavelength in the PL spectra. The measured value of this energy band-gap is ca. 2.87 eV (λ_{em} = 432 nm) which is almost 1 eV higher than the Sb_2S_3 bulk-value (1.6 to 1.9 eV [31–32]). This result is in accordance with a well-known quantum-size effect observed with nanosized semiconductor materials [10, 11].

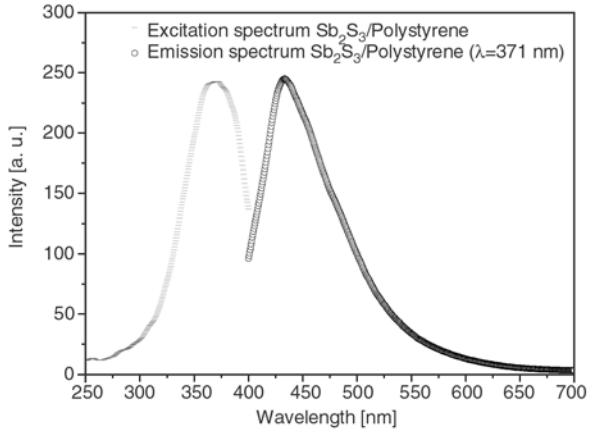

Figure 5. Photoluminescence spectra of an antimony-stibnite/polystyrene nanocomposite film

4. Conclusions

The antimony dodecyl-mercaptide thermolysis has been studied as a pure phase and as solution in polymer. In both cases the thermal decomposition of the mercaptide gave a mixture of antimony trisulfide (Sb_2S_3) and zero-valent antimony powder. The stibnite/antimony mixture obtained from the thermolysis of pure $Sb(SC_{12}H_{25})_3$ is made of 89.6 wt% Sb_2S_3 prismatic crystals (30–150 μm length and 10–20 μm in diameter) and 10.4 wt% of Sb aggregated polyhedral crystals (average size 2–3 μm). The antimony-stibnite/polystyrene nanocomposite, prepared by the thermolysis of $Sb(SC_{12}H_{25})_3$ dissolved in polystyrene, exhibits peculiar luminescent characteristics due to the stibnite nanocrystals with average dimensions ranging from 15 to 30 nm. The possibility to produce in situ polymer nanocomposites with new functionalities is of great importance for application in widespread fields and the here proposed synthesis method based on antimony dodecyl-mercaptide thermolysis in polystyrene is compatible with all current polymer manufacturing technologies.

Acknowledgements

The authors would like to thank to Prof. G. Artioli (Dipartimento di Mineralogia e Petrologia Università di Padova, Italia) and Dr. M. Dapiaggi (Dipartimento di Scienze della Terra 'Ardito Desio', Università di Milano I, Italia) for many stimulating discussions on XRD science.

References

[1] Carotenuto G., Nicolais L.: Nanocomposites, metal-filled. in 'Encyclopedia of Polymer Science and Technology' (ed.: Mark H. F.) Wiley, New York, Vol 10, 235–254 (2003).

[2] Mayer A. B. R.: Formation of noble metal nanoparticles within a polymeric matrix: Nanoparticle features and overall morphologies. Materials Science and Engineering: C, **6**, 155–166 (1998). DOI: 10.1016/S0928-4931(98)00049-6

[3] Carotenuto G., Nicolais L., Perlo P., Martorana B.: Method of production of polymer/metal or metal sulphide composites which uses metal mercaptides. U.S. Patent 7329700, USA (2007).

[4] Vecchione R., Carotenuto G., Casuscelli V., Esposito F., Leonardi S., Nicolais L., Volpe M. V.: Process for the preparation of a composite polymeric material. U.S. Patent 20060121262, USA (2006).

[5] Cardone G., Carotenuto G., Longo A., Perlo P., Ambrosio L.: Synthesis of gold nano-plates by mercaptide thermolysis in poly(vinyl acetate). Express Polymer Letters, **1**, 604–607 (2007). DOI: 10.3144/expresspolymlett.2007.82

[6] Caseri W.: Nanocomposites of polymers and metals or semiconductors: Historical background and optical properties. Macromolecular Rapid Communications, **21**, 705–722 (2000). DOI: 10.1002/1521-3927(20000701)21:11<705::AID-MARC705>3.0.CO;2-3

[7] Godovsky D. J.: Device applications of polymer-nanocomposites. Advances in Polymer Science, **153**, 163–205 (2000). DOI: 10.1007/3-540-46414-X

[8] Chen W., Joly A. G., Malm J. O., Bovin J. O., Wang S. J.: Full-color emission and temperature dependence of the luminescence in poly-*P*-phenylene ethynylene-ZnS/Mn^{2+} composite particles. The Journal of Physical Chemistry B, **107**, 6544–6551 (2003). DOI: 10.1021/jp034476r

[9] Šajinović D., Šaponjic Z. V., Cvjetićanin N., Marinović-Cincović M., Nedeljković J. M.: Synthesis and characterization of CdS quantum dots-polystyrene composite. Chemical Physics Letters, **329**, 168–172 (2000). DOI: 10.1016/S0009-2614(00)00990-8

[10] Gubin S. P., Kataeva N. A., Khomutov G. B.: Promising avenues of research in nanoscience: Chemistry of semiconductor nanoparticles. Russian Chemical Bulletin, **54**, 827–852 (2005). DOI: 10.1007/s11172-005-0331-3

[11] Alivisatos A. P.: Semiconductor clusters, nanocrystals, and quantum dots. Science, **271**, 933–937 (1996). DOI: 10.1126/science.271.5251.933

[12] Link S., El-Sayed M. A.: Shape and size dependence of radiative, non-radiative and photothermal properties of gold nanocrystals. International Reviews in Physical Chemistry, **19**, 409–453 (2000).

[13] Burda C., Chen X., Narayanan R., El-Sayed M. A.: Chemistry and properties of nanocrystals of different shapes. Chemical Reviews, **105**, 1025–1102 (2005). DOI: 10.1021/cr030063a

[14] Medintz I. L., Uyeda H. T., Goldman E. R., Mattoussi H.: Quantum dot bioconjugates for imaging, labelling and sensing. Nature, **4**, 435–446 (2005). DOI: 10.1038/nmat1390

[15] Huang H., Dorn A., Bulovic V., Bawendi M. G.: Electrically driven light emission from single colloidal quantum dots at room temperature. Applied Physics Letters, **90**, 23110–23111 (2007). DOI: 10.1063/1.2425043

[16] Rao C. N. R., Govindaraj A., Vivekchand S. R. C.: Inorganic nanomaterials: Current status and future prospects. Annual Reports on the Progress of Chemistry, Section A, **102**, 20–45 (2006). DOI: 10.1039/b516174f

[17] Li Y., Rizzo A., Cingolati R., Gigli G.: Bright white-light-emitting device from ternary nanocrystal composites. Advanced Materials, **18**, 2545–2548 (2006). DOI: 10.1002/adma.200600181

[18] Versavel M. Y., Haber J. A.: Lead antimony sulfides as potential solar absorbers for thin film solar cells. Thin Solid Films, **515**, 5767–5770 (2007). DOI: 10.1016/j.tsf.2006.12.077

[19] Versavel M. Y., Haber J. A.: Structural and optical properties of amorphous and crystalline antimony sulfide thin-films. Thin Solid Films, **515**, 7171–7176 (2007). DOI: 10.1016/j.tsf.2007.03.043

[20] Roy B., Chakraborty B. R., Bhattacharya R., Dutta A. K.: Electrical and magnetic properties of antimony sulphide (Sb_2S_3) crystals and the mechanism of carrier transport in it. Solid State Communications, **25**, 937–940 (1978). DOI: 10.1016/0038-1098(78)90306-X

[21] Chokalingam M. J., Nagaraja Rao K., Rangarajan R., Suryanarayana C. V.: Studies on sintered photoconductive layers of antimony trisulphide. Journal of Physics D: Applied Physics, **3**, 1641–1644 (1970). DOI: 10.1088/0022-3727/3/11/311

[22] Arivuoli D., Gnanam F. D., Ramasamy P.: Growth and microhardness studies of chalcogenides of arsenic, antimony and bismuth. Journal of Materials Science Letters, **7**, 711–713 (1988). DOI: 10.1007/BF00722076

[23] Wu Q-S., Zhang G-X., Ding Y-P.: Soft-template synthesis and optical properties of Sb_2S_3 semiconductor quasi-nanospheres. Journal of Nanoparticle Research, **8**, 737–742 (2006). DOI: 10.1007/s11051-005-4965-8

[24] Taylor J. R., Fang M. M., Nie S.: Probing specific sequences on single DNA molecules with bioconjugated fluorescent nanoparticles. Analytical Chemistry, **72**, 1979–1986 (2000). DOI: 10.1021/ac9913311

[25] Wu J. S., Dhara S., Wu C. T., Chen K. H., Chen Y. F., Chen L. C.: Growth and optical properties of self-organized Au_2Si nanospheres pea-podded in a silicon oxide nanowire. Advanced Materials, **14**, 1847–1850 (2002).
DOI: 10.1002/adma.200290017

[26] Hu Y., Chen J., Chen W., Lin X., Li X.: Synthesis of novel nickel sulfide submicrometer hollow spheres. Advanced Materials, **15**, 726–729 (2003).
DOI: 10.1002/adma.200304687

[27] Carotenuto G., Martorana B., Perlo P., Nicolais L.: A universal method for the synthesis of metal and metal sulfide clusters embedded in polymer matrices. Journal of Materials Chemisty, **13**, 2927–2930 (2003).
DOI: 10.1039/b310898h

[28] Mehrotra R. C., Gupta V. D., Chatterjee S.: A study of alkylthioantimonites $Sb(SR)_3$. Australian Journal of Chemistry, **21**, 2929–2932 (1968).

[29] Hines M. A., Guyot-Sionnest P.: Synthesis and characterization of strongly luminescing ZnS-capped CdSe nanocrystals. The Journal of Physical Chemistry, **100**, 468–471 (1996).
DOI: 10.1021/jp9530562

[30] Murray C. B., Norris D. J., Bawendi M. G.: Synthesis and characterization of nearly monodisperse CdE (E = sulfur, selenium, tellurium) semiconductor nanocrystallites. Journal of the American Chemical Society, **115**, 8706–8715 (1993).
DOI: 10.1021/ja00072a025

[31] Pigau N.: Structural characterization and optical properties of annealed Sb_2S_3 thin films. Romanian Journal of Physics, **53**, 209–215 (2008).

[32] Vedeshwar A. G.: Optical properties of amorphous and polycrystalline stibnite (Sb_2S_3) films. Journal de Physique III, **5**, 1161–1172 (1995).
DOI: 10.1051/jp3:1995183

eXPRESS Polymer Letters Vol.3, No.4 (2009) 226–234
Available online at www.expresspolymlett.com
DOI: 10.3144/expresspolymlett.2009.29

Effect of electron beam irradiation and poly(vinyl pyrrolidone) addition on mechanical properties of polycaprolactone with empty fruit bunch fibre (OPEFB) composite

N. A. Ibrahim[1], S. N. A. Ahmad[1], W. M. Z. W. Yunus[1], K. Z. M. Dahlan[2]*

[1]Chemistry Department, Faculty of Science, Universiti Putra Malaysia, UPM Serdang, 43400 Selangor, Malaysia
[2]Malaysian Nuclear Agency, Bangi 43000 Kajang, Malaysia

Received 7 January 2009; accepted in revised form 23 February 2009

Abstract. Biodegradable composites or green composites were prepared by melt blending technique using polycaprolactone and oil palm empty fruit bunch fibre (OPEFB). Since OPEFB is not compatible with PCL a binder, poly(vinyl pyrrolidone), (PVP) was used to improve the interaction between PCL and OPEFB. The composites produced were irradiated using electron beam to improve the mechanical properties. The tensile, flexural and impact strengths of PCL/OPEFB composites were improved by addition of 1% by weight of PVP and irradiated with 10 kGy of electron beam. The FTIR spectra indicate a slight increase of frequencies at C=O peaks from 1730 to 1732 cm^{-1} after irradiation indicates some interaction between C=O and O–H. The surface morphology of the facture surface obtained from tensile test shows no fibre pull out indicating good adhesion between the OPEFB and PCL after addition of PVP.

Keywords: *polymer composites, biodegradable polymers, mechanical properties*

1. Introduction

In recent years, the research and development of green polymeric materials has attracted more attention due to the concerns related to the environmental pollution by non degradable plastic wastes. Natural fibre reinforced composites using thermoplastic such as polypropylene and polyethylene as a matrix has been widely use in automotive application but the composites are partially biodegradable. Thus the formulation of composites with matrices, which originate from biodegradable raw material such as polycaprolactone should be investigated.

Polycaprolactone (PCL) is an aliphatic polyester, with adequate mechanical properties and good degradability [1–3]. PCL also has excellent biocompatibility, flexibility and has been used as a plasticizer. PCL is degraded by hydrolysis of its ester linkages in physiological conditions (such as in the human body) and has therefore received a great deal of attention for use as an implantable biomaterial. Major difficulties in using this polymer are poor availability, poor process ability, low toughness, high price and low moisture stability [4, 5]. The 60°C melting point is also too low for many applications. Thus reinforcing with natural fibres is one possibility to reduce the cost, to improve stiffness and to enhance thermal stability. In addition the use of natural fibre such as oil palm empty fruit bunch fibre as filler also improves mechanical properties of biodegradable polymers.

Oil palm empty fruit bunch fibre (OPEFB) is one of the major solid wastes produced by oil palm indus-

*Corresponding author, e-mail: norazowa@science.upm.edu.my

try. However the primary drawback of using natural fibres for reinforcement is the poor interfacial adhesion between polar-hydrophilic OPEFB and non polar-hydrophobic plastics. The reinforcement of thermoplastic by means of cellulosic fibres significantly improves stiffness and strength while it drastically reduces the composite toughness [8–10]. A number of methods have already existed today for improving the interfacial interaction between lignocellulosics and thermoplastics [10]. Among them: (i) the chemical modification of a lignocellulosic, either by condensation or free radical reaction [11–19] (ii) the use of modified thermoplastic containing a compound capable of interacting with a lignocellulosic [20–23], (iii) the addition of a third component with the ability to interact simultaneously at the interface with the thermoplastic and the lignocellulosic (compatibiliser) [24–27].

Chemical analysis of OPEFB shows that OPEFB consist of 65% cellulose and 19% lignin [6]. Oil palm fibre has relatively high strength and stiffness, low density and causes no skin irritations on contact. Many investigations have been made on the potential of natural fibres as reinforcement for composite but these composites use thermoplastics which are non biodegradable polymers as a matrix [7–9]. These composites have found applications in furniture, packaging, building and automobile industries [10].

Poly(*N*-vinyl-2-pyrrolidone) (PVP) is widely used in different aspects, such as additives to cosmetics, coatings and biomedicines due to its excellent biocompatibility and hydrophilicity [28–32]. PVP binds to polar molecules exceptionally well owing to its polarity. Rovira-Bru *et al*. [30] has used PVP as a zirconia surface modifier. It was reported the maximum adsorption capacity of protein decreased by up to about 76%. On the other hand, a chemical crosslinking method has been used by Kang *et al.* [33]. PVP was immobilized within chlorinated poly(vinyl chloride) membrane to improve its liquid permeation behaviours [34].

This paper describes the preparation and characterization of new biodegradable composites from oil palm empty fruit bunch fibre and polycaprolactone. The interfacial adhesion between the polymer matrix and the filler was improved by the radiation method via electron-beam irradiation in the presence of poly(vinyl pyrrolidone) as the compatibiliser.

2. Experimental

2.1. Materials

Polycaprolactone from Solvay Caprolactone was purchased from Colour Pigment (M) Sdn. Bhd. The compatibiliser used in this study, poly(vinylpyrrolidone) (PVP) was from Merck Schuchardt OHG, Germany. Oil palm empty fruit bunch fibre (OPEFB) was obtained from Sabutek (M) Sdn. Bhd., Perak, Malaysia. The OPEFB fibre was washed by soaking in distilled water for 24 hour to remove the excessive wax and other impurities. The fibre was then rinsed with hot water (60°C) and acetone prior to drying at 60°C in an oven. The fibre was ground to particle size of 200 μm by using crusher machine.

2.2. Sample preparation

The composites OPEFB:PCL were prepared in 40:60 by weight. The compatibiliser (PVP) was added during the mixing which is ranging from 1 to 5% by weight. PVP was mixed with OPEFB prior the blending as both are hydrophilic.

2.3. Electron beam irradiation

Melt blending was carried out at 70°C and 50 rpm rotor speed in Haake rheomixer. The blends were then compression moulded under a pressure of 14.7 MPa at 70°C and 6 mm thick. The sheets were immediately cooled between two plates of a cold press at 25°C. The moulded sheets were irradiated using an electron beam (EB) machine EPS Model-3000 at 5–40 kGy at room temperature with one side irradiation. After irradiation, the samples were reheated until melt and compressed moulded into 1 and 3 mm thick sheets for mechanical testing. The accelerator energy of the EB is 2 MeV, beam current of 2 mA at 5 kGy/pass.

2.4. Tensile properties

The tensile strength, tensile modulus and elongation at break were measured by using Instron Universal Testing Machine 4301 at 5 mm/min of crosshead speed in accordance to ASTMD638 [36]. Seven samples were used for the tensile test and an average of five results was taken as the resultant value.

2.5. Flexural properties

The flexural strength and flexural modulus were measured with Instron Universal Testing Machine 4301 according to ASTM D790 [37]. The size of the samples tested is 127×12.7×3 mm. The crosshead speed is 1.3 mm/min and the support span length is 48 mm.

2.6. Impact properties

To evidence the effect of the curing time on the toughening properties of the adhesives, the Izod impact test was carried out according to ASTM D256 standard using an impact tester (IZOD Impact Tester) [38]. The sample size is 63.5×12.7×3 mm, the notch length is 2.54 mm.

2.7. Fourier-transform infrared analysis

The FTIR spectra of the composites samples were recorded on Fourier-transform IR Spectrophotometer (Perkin-Elmer Spectrum BX). Samples were compressed into thin film before scanning from 4000 to 400 cm^{-1}.

2.8. Scanning electron microscopy

The morphology of tensile fracture surface of the composites was observed by scanning electron microscope (SEM) at room temperature. A JEOL (model JSM-6300F) SEM with field emission gun and accelerating voltage of 10 kV was used. A gold coating of a few nanometres in thickness was coated on tensile fracture surfaces. The samples were viewed perpendicular to the fractured surface.

3. Results and discussion

Composites with good mechanical properties can be obtained when the filler is well dispersed in the matrix. In addition the filler and the matrix should be compatible, thus addition of PVP which acts as the binder to the filler (OPEFB) helped to improve the mechanical properties of the composites. Interaction and adhesion between the OPEFB and PCL can also be improved by irradiation of electron beam which induced crosslinking in the presence of PVP.

3.1. Effect of radiation dose and PVP on tensile properties

Radiation processing concerns molecular weight increase by irradiation induced crosslinking and decrease in molecular weight when the radiation tends to promote degradation by chain scission reaction and the process depends on the absorbed dose [39]. Figures 1 and 2 show the effect of absorbed dose on tensile strength and modulus respectively. From this study 10 kGy gives the optimum absorbed dose to produce composites with good mechanical properties.

Figure 3 depicts the comparison of tensile strength between irradiated (10 kGy) and non-irradiated

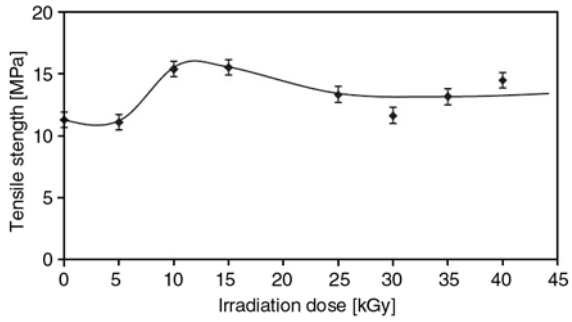

Figure 1. Tensile strength of OPEFB:PCL (40:60) composites with 10% of PVP content at various irradiation dose

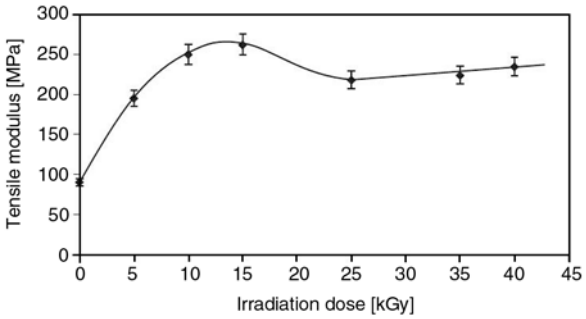

Figure 2. Tensile modulus of OPEFB:PCL (40:60) composites with 10% of PVP content at various irradiation dose

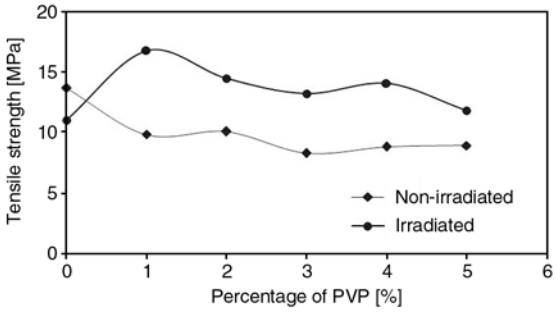

Figure 3. Tensile strength of irradiated and non-irradiated OPEFB:PCL composites at various PVP content

OPEFB/PCL composites with and without PVP. Tensile strength of composites decreased with the addition of PVP in non-irradiated composites indicating that no improvement in interaction between OPEFB and PCL. Irradiation of the composites with 10 kGy of electron beam improved the tensile strength significantly. The addition of 1% PVP in OPEFB/PCL composite has enhanced the crosslink density resulted in an increase in tensile strength [1]. The drops in tensile strength with the increase of PVP may be due to the formation of excessive crosslinking in the composites which results in embrittlement of the samples. Only 1% of PVP is needed to improve the tensile strength by 71% after the irradiation.

Figure 4 shows almost similar results with tensile strength where irradiation gives higher modulus. A high tensile modulus means that the material is rigid – more stress is required to produce a given amount of strain which means it resists deformation or stretch. The tensile modulus increased significantly with the addition of 1% PVP after irradiation as shown in Figure 4. The increase in tensile modulus is due to the inherent the stiffness of the polymer matrix and of the filler, and to the crosslinking that made the polymer more rigid, as revealed by a slight decreased in elongation at break (Figure 5).

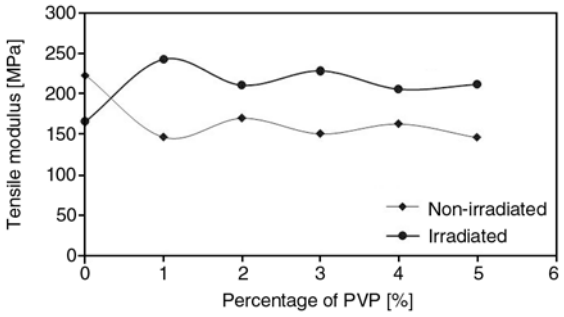

Figure 4. Tensile modulus of irradiated and non-irradiated OPEFB:PCL composites at various PVP content

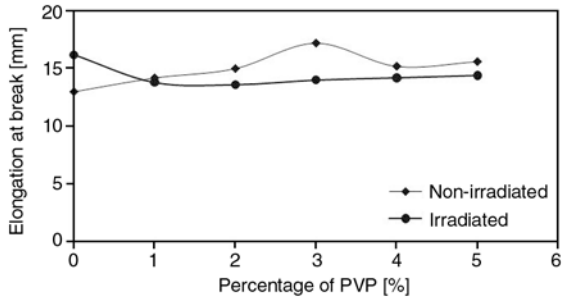

Figure 5. Elongation at break of irradiated and non-irradiated OPEFB:PCL composites at various PVP content

The improvement in interaction between OPEFB and PCL are also indicated by the increase in the stiffness of the composites.

Figure 5 shows that elongation at break for irradiated composites is slightly lower than compound without irradiation. This is due to better stiffness and strength attributed to the strong adhesion between fibre and polymer matrix. Consequently, the toughness of the composites is reduced, resulting in lower elongation at break. Higher toughness is obtained from weak interfacial adhesion as shown by non-irradiated composites. Weak interfacial bonding resulted in energy adsorption mechanism, i.e. bond breakage at the fibre/matrix interface and pull out fibre caused higher toughness in the composites [40].

3.2. Flexural properties

Flexural strength of the composites which were subjected to electron-beam irradiation is 15% higher (Figure 6) than that of the non-irradiated compound at 1% of PVP. The trends for both compounds are quite constant. Therefore, they remain nearly unaffected by the amount of compatibiliser, PVP. However, the overall results for irradiated samples are slightly higher, caused by the better adhesion between the fibre and matrix which provides an increase in stress transfer from the matrix to the filler, thus increased stress at failure and the higher values for flexural strength [41]. Flexural modulus (Figure 7) shows almost similar trend with flexural strength which means irradiation caused the composites to become stiffer, attributed to mild crosslinking reaction in the composites. Thus, electron beam irradiation results in significant improvement in tensile properties as well as flexural properties of the composites.

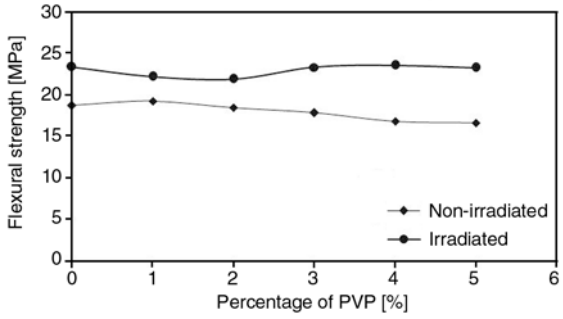

Figure 6. Flexural strength of irradiated and non-irradiated OPEFB:PCL composites at various PVP content

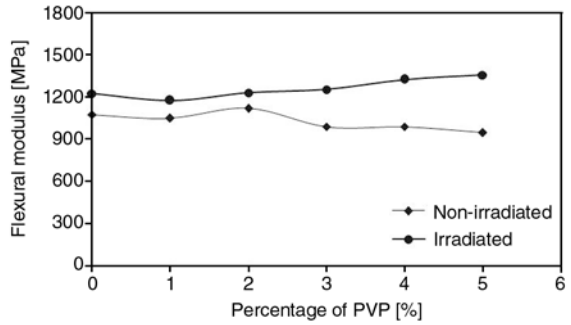

Figure 7. Flexural Modulus of irradiated and non-irradiated OPEFB:PCL composites at various PVP content

3.3. Impact properties

It was reported earlier that with increasing filler contents both unnotched and notched impact strength decreased linearly. The presence of wood-fibres in the polymer matrix provides points of stress concentrations, thus providing sites for crack initiations. Another reason for decrease in impact strength could be the stiffening of the polymer chains due to bonding between wood-fibres and matrix. For high impact properties, in fact, a slightly weaker adhesion between fibre and polymer is desirable [41]. However, this hypothesis could only be used in the case of low filler content. For the composites with poor interfacial adhesion between fibre and matrix, the toughness of composites will decrease abruptly with increasing of fibre content and remains constant at the particular point. This can be observed in Figures 8 and 9 for both unnotched and notched composites. The impact strength of irradiated composites was higher than those without irradiation. This may be due to the improved interaction between fibre and matrix after the irradiation. For the unnotched composites, the optimum impact strength was achieved at 1% of

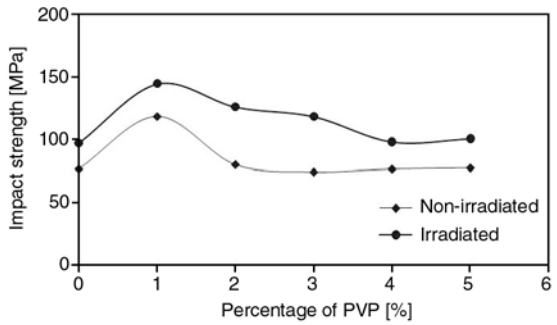

Figure 8. Unnotched impact strength of irradiated and non-irradiated OPEFB:PCL composites at various PVP content

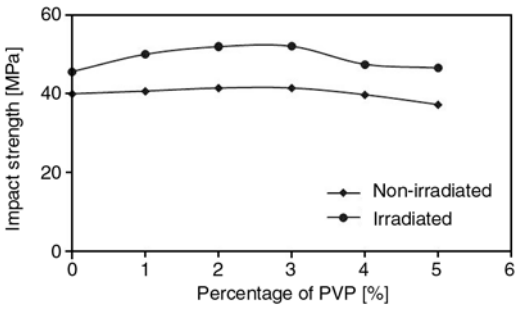

Figure 9. Notched impact strength of irradiated and non-irradiated OPEFB:PCL composites at various PVP content

compatibiliser. As for the notched samples, a slight change was observed which is the impact strength increased with the irradiation.

3.4. Fourier transform infra red (FTIR) analysis

FTIR spectroscopy is a technique that is sensitive to specific intermolecular interaction [42]. Kim and Choi [43] observed shifting of peaks in IR spectra when their blends have a strong interaction such as hydrogen bonding. In this study FTIR spectroscopy was used to monitor the absorption peak shifts in specific regions to determine the known functional group interactions of the PCL with OPEFB or PVP. The regions of interest are 1750–1700 cm^{-1} and 3600–3000 cm^{-1} for C=O and O–H stretch respectively. Figure 10 shows the FTIR spectra of irradiated and non-irradiated OPEFB/PCL composites. The C=O peaks appear at 1730 cm^{-1} for both OPEFB:PCL and OPEFB:PCL:PVP 1% spectra indicating there is no extra interaction or new bond formed with the C=O group before irradiation. After irradiation, there is a slight peak shifting appears at C=O for the irradiated sample compared

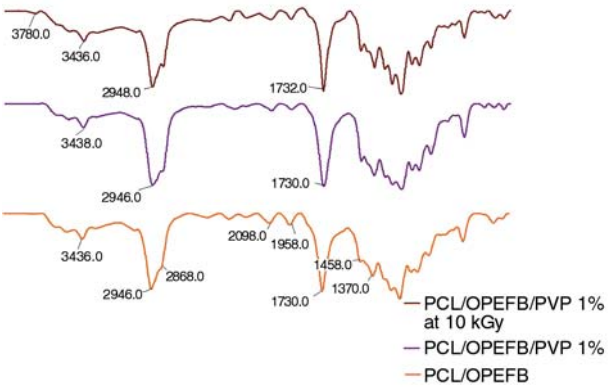

Figure 10. FTIR spectra of OPEFB/PCL composites

to the samples prior irradiation which is 1732 and 1730 cm^{-1} respectively, thus indicating some interactions occurs at the carbonyl group.

3.5. Morphology

Figures 11a–11c show tensile fracture surfaces for the composites. In the case of without compatibiliser and irradiation, many cavities could be seen where the fibre has been pulled-out (Figure 11a), attributed by poor fibre/matrix adhesion. The holes proximity also indicates that fibre could not provide an efficient stress transfer from the matrix to the filler causing them to have lower mechanical properties in response to stress. Figure 11b also indicates the almost similar result with the former, where many cavities are to be seen compared to Figure 11c. From the micrographs, more fibre-breakage could be seen in the composites incorporating PVP and irradiation, causing them to have better fibre matrix adhesion which is in agreement with the mechanical properties reported above. As suggested by Adolfsson *et al.* [35] PVP binds to polar molecules exceptional well owing to its polarity.

4. Conclusions

OPEFB/PCL composites were successfully prepared by melt blending technique. Some prepara-

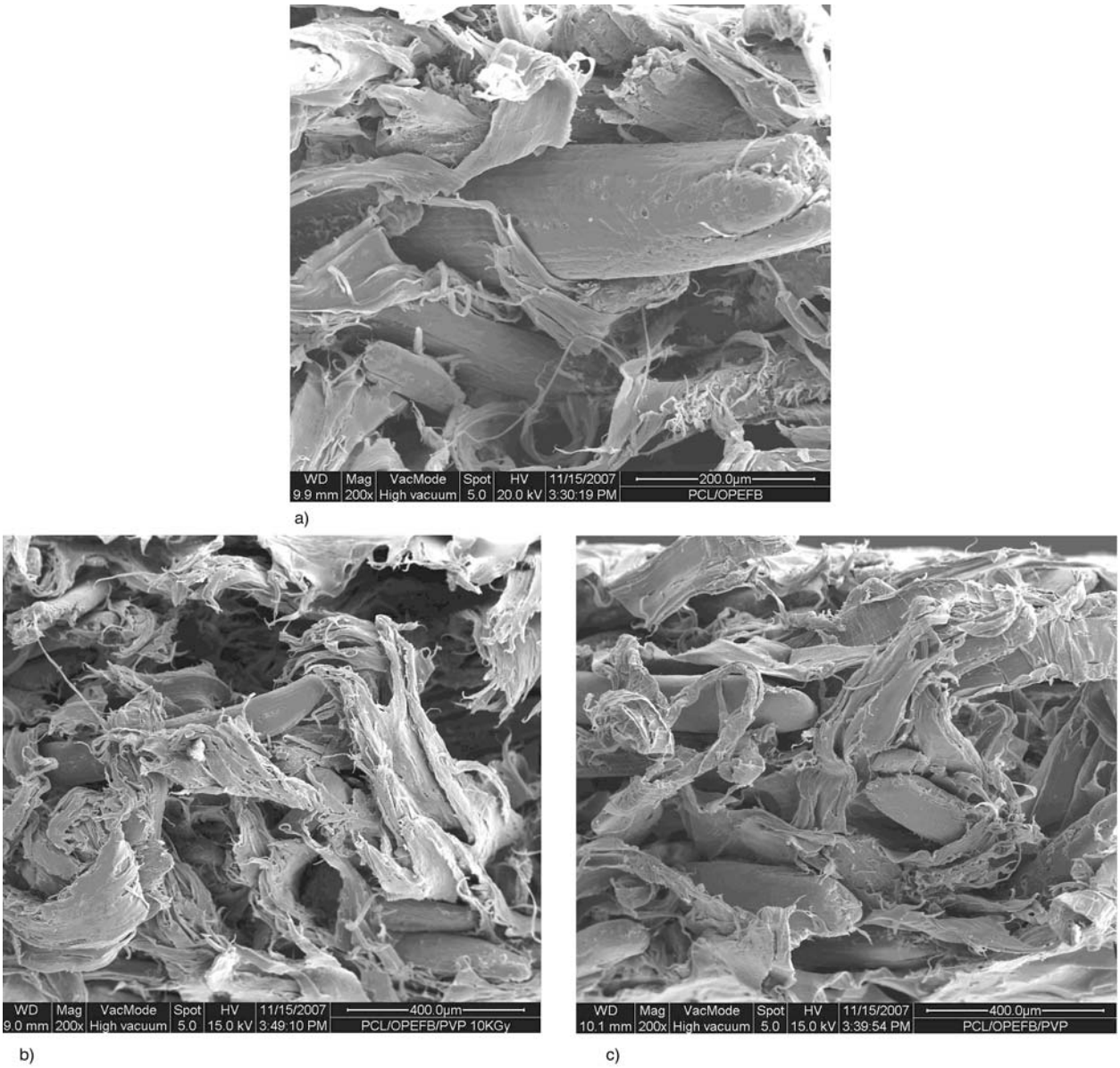

Figure 11. SEM micrographs tensile fracture surface of OPEFB/PCL composites (200×): a) OPEFB/PCL, b) OPEFB/PCL/PVP 1%, c) OPEFB/PCL/PVP 1% at 10 kGy

tion conditions such as absorbed dose and amount of PVP were investigated. The mechanical properties of the composites such as tensile, flexural and impact properties have improved significantly with irradiation in occurrence of compatibiliser, indicating a possible crosslinking of the polymer at low dose of 10 kGy and 1% PVP. The tensile strength of PCL/OPEFB without PVP and treatment is 10.3 MPa whereas after addition of PVP and treatment the tensile strength increased to 16.7 MPa indicating good stress transfer from OPEFB to PCL matrix. PVP acts as binder and cross-linker in the presence of electron beam irradiation provide good adhesion or interaction between OPEFB and PCL. Scanning electron microscopic analysis on the fractured surface of the tensile test also indicates good adhesion between OPEFB and PCL.

Acknowledgements

The authors would like to thank the Ministry of Science, Technology and Innovation (MOSTI) for the National Science Fellowship Award that has made this research work possible.

References

[1] Abdel-Rehim H. A., Yoshii F., Kume T.: Modification of polycaprolactone in the presence of polyfunctional monomers by irradiation and its biodegradability. Polymer Degradation and Stability, **85**, 689–695 (2004).
DOI: 10.1016/j.polymdegradstab.2004.03.010

[2] Shinoda H., Asou Y., Kashima T., Kato T., Tseng Y., Yagi T.: Amphiphilic biodegradable copolymer, poly(aspartic acid-co-lactide): Acceleration of degradation rate and improvement of thermal stability for poly(lactic acid), poly(butylenes succinate) and poly(ε-caprolactone). Polymer Degradation and Stability, **80**, 241–250 (2003).
DOI: 10.1016/S0141-3910(02)00404-4

[3] Todo M., Park S-D., Takayama T., Arakawa K.: Fracture micromechanisms of bioabsorbable PLLA/PCL polymer blends. Engineering Fracture Mechanics, **74**, 1872–1883 (2007).
DOI: 10.1016/j.engfracmech.2006.05.021

[4] Chen L., Ni Y., Bian X., Qiu X., Zhuang X., Chen X., Jing X.: A novel approach to grafting polymerization of ε-caprolactone onto starch granules. Carbohydrate Polymer, **60**, 103–109 (2005).
DOI: 10.1016/j.carbpol.2004.11.028

[5] Wang L., Ma W., Gross R. A., McCarthy S. P.: Reactive compatibilization of biodegradable blends of poly(lactic acid) and poly(ε-caprolactone). Polymer Degradation and Stability, **59**, 161–168 (1998).
DOI: 10.1016/S0141-3910(97)00196-1

[6] Sreekala M. S., Kumaran M. G., Sabu T.: Oil palm fibres: Morphology, chemical composition, surface modification, and mechanical properties. Journal of Applied Polymer Science, **66**, 821–835 (1997).
DOI: 10.1002/(SICI)1097-4628(19971031)66:5<821::AID-APP2>3.0.CO;2-X

[7] Rozman H. D., Saad M. J., Mohd Ishak Z. A.: Flexural and impact properties of oil palm empty fruit bunch (EFB)-polypropylene composites-the effect of maleic anhydride chemical modification of EFB. Polymer Testing, **22**, 335–341 (2003).
DOI: 10.1016/S0142-9418(02)00109-5

[8] Kokta B. V., Chen R., Daneault C., Valade J. L.: Use of wood fibres in thermoplastic composites. Polymer Composites, **4**, 229–232 (1983).
DOI: 10.1002/pc.750040407

[9] Woodhams R. T., Thomas G., Rodger D. K.: Wood fibres as reinforcing fillers for polyolefins. Polymer Engineering and Science, **24**, 1166–1171 (1984).
DOI: 10.1002/pen.760241504

[10] Bledzki A. K., Gassan J.: Composites reinforced with cellulose based fibers. Progress in Polymer Science, **24**, 221–274 (1999).
DOI: 10.1016/S0079-6700(98)00018-5

[11] Gardea-Hernández G., Ibarra-Gómez R., Flores-Gallardo S. G., Hernández-Escobar C. A., Pérez-Romo P., Zaragoza-Contreras E. A.: Fast wood fibre esterification. I. Reaction with oxalic acid and cetyl alcohol. Carbohydrate Polymers, **71**, 1–8 (2008).
DOI: 10.1016/j.carbpol.2007.05.014

[12] Bledzki A. K., Mamun A. A., Lucka-Gabor M., Gutowski V. S.: The effects of acetylation on properties of flax fibre and its polypropylene composites. Express Polymer Letters, **2**, 413-422 (2008).
DOI: 10.3144/expresspolymlett.2008.50

[13] George J., Sreekala M. S., Thomas S.: A review on interface modification and characterization of natural fibre reinforced plastic composites. Polymer Engineering and Science, **41**, 1471–1485 (2001).
DOI: 10.1002/pen.10846

[14] Gupta K. C., Sahoo S.: Grafting of acrylonitrile and methyl methacrylate from their binary mixture on cellulose using ceric ions. Journal of Applied Polymer Science, **79**, 767–778 (2001).

[15] Nakamura R., Goda K., Noda J., Ohgi J.: High temperature tensile properties and deep drawing of fully green composites. Express Polymer Letters, **3**, 19–24 (2009).
DOI: 10.3144/expresspolymlett.2009.4

[16] Mohanty A. K., Mubarak A. K., Hinrichsen G.: Surface modification of jute and its influence on performance of biodegradable jute-fabric/biopol composites. Composites Science and Technology, **60**, 1115–1124 (2000).
DOI: 10.1016/S0266-3538(00)00012-9

[17] Redondo S. U. A., Radovanovic E., Gonçalves M. C., Yoshida I. V. P.: Eucalyptus kraft pulp fibres as an alternative reinforcement of silicone composites: I. Characterization and chemical modification of eucalyptus fibre with organosilane coupling agent. Journal of Applied Polymer Science, **85**, 2573–2579 (2002). DOI: 10.1002/app.10905

[18] Román-Aguirre M., Márquez-Lucero A., Zaragoza-Contreras E. A.: Elucidating the graft copolymerization of methyl methacrylate onto wood-fibre. Carbohydrate Polymers, **55**, 201–210 (2004). DOI: 10.1016/j.carbpol.2003.09.008

[19] Thiebaud S., Borredon M. E., Baziard G., Senocq F.: Properties of wood esterified by fatty-acid chlorides. Bioresource Technology, **59**, 103–107 (1997). DOI: 10.1016/S0960-8524(96)00160-5

[20] Chauhan G. S., Guleria L. K., Misra B. N., Kaur I.: Polymers from renewable resources. II. A study in the radio chemical grafting of poly(styrene-alt-maleic anhydride) onto cellulose extracted from pine needles. Journal of Polymer Science Part A: Polymer Chemistry, **37**, 1763–1769 (1999). DOI: 10.1002/(SICI)1099-0518(19990615)37:12<1763:: AID-POLA5>3.0.CO;2-S

[21] Fung K. L., Li R. K. Y., Tjong S. C.: Interface modification on the properties of sisal fibre reinforced polypropylene composites. Journal of Applied Polymer Science, **85**, 169–176 (2002). DOI: 10.1002/app.10584

[22] Matías M. C., De la Orden M. U., González Sánchez C., Martínez Urreaga J.: Comparative spectroscopic study of the modification of cellulosic materials with different coupling agents. Journal of Applied Polymer Science, **75**, 256–266 (2000). DOI: 10.1002/(SICI)1097-4628(20000110)75:2<256::AID-APP8>3.0.CO;2-Z

[23] Navarro Cassu S., Felisberti M. A.: In situ compatibilisation of polystyrene and polyurethane blends by using poly(styrene-*co*-maleic anhydride) as reactive compatibiliser. Journal of Applied Polymer Science, **82**, 2514–2524 (2001). DOI: 10.1002/app.2102

[24] Feng D., Caulfiel D. F., Sanadi A. R.: Effect of compatibiliser on the structure-property relationships of kenaf-fibre/polypropylenecomposites. Polymer Composites, **22**, 506–517 (2001). DOI: 10.1002/pc.10555

[25] Martínez Urreaga J., Matías M. C., De la Orden M. U., Lechuga Munguía M. A., González Sánchez C.: Effects of coupling agents on the oxidation and darkening of cellulosic materials used as reinforcements for thermoplastic matrices in composites. Polymer Engineering and Science, **40**, 407–417 (2000). DOI: 10.1002/pen.11174

[26] Oksman K., Lindberg H., Holmgren A.: The nature and location of SEBS-MA compatibiliser in polyethylene-wood flour composites. Journal of Applied Polymer Science, **69**, 201–209 (1998). DOI: 10.1002/(SICI)1097-4628(19980705)69:1<201::AID-APP23>3.0.CO;2-0

[27] Rana A. K., Mandal A., Mitra B. C., Jacobson R., Rowell R., Baneerjee A. N.: Short jute fibre-reinforced polypropylene composites: Effect of compatibiliser. Journal of Applied Polymer Science, **69**, 329–338 (1998). DOI: 10.1002/(SICI)1097-4628(19980711)69:2<329::AID-APP14>3.0.CO;2-R

[28] Mosqueda-Jimenez D. B., Narbaitz R. M., Matsuura T., Chowdhury G., Pleizier G., Santerre J. P.: Influence of processing conditions on the properties of ultrafiltration membranes. Journal of Membrane Science, **231**, 209–224 (2004). DOI: 10.1016/j.memsci.2003.11.026

[29] Mosqueda-Jimenez D. B., Narbaitz R. M., Matsuura T.: Impact of membrane surface modification on the treatment of surface water. Journal of Environmental Engineering, **130**, 1450–1459 (2004). DOI: 10.1061/(ASCE)0733-9372(2004)130:12(1450)

[30] Rovira-Bru M., Giralt F., Cohen Y.: Protein adsorption onto zirconia modified with terminally grafted polyvinylpyrrolidone. Journal of Colloid and Interface Science, **235**, 70–79 (2001). DOI: 10.1006/jcis.2000.7355

[31] Torchilin V. P., Levchenko T. S., Whiteman K. R., Yaroslavov A. A., Tsatsakis A. M., Rizos A. K., Michailova E. V., Shtilman M. I.: Amphiphilic poly-*N*-vinylpyrrolidones: Synthesis, properties and liposome surface modification. Biomaterials, **22,** 3035–3044 (2001). DOI: 10.1016/S0142-9612(01)00050-3

[32] Higuchi A., Shirano K., Harashima M., Yoon B. O., Hara M., Hattori M., Imamura K.: Chemically modified polysulfone hollow fibres with vinylpyrrolidone having improved blood compatibility. Biomaterials, **23**, 2659–2666 (2002). DOI: 10.1016/S0142-9612(01)00406-9

[33] Kang J. S., Kim K. Y., Lee Y. M.: Preparation of PVP immobilized microporous chlorinated poly(vinyl chloride) membranes on fabric and their hydraulic permeation behaviour. Journal of Membrane Science, **214**, 311–321 (2003). DOI: 10.1016/S0376-7388(02)00597-5

[34] Yu H-Y., Xu Z-K., Xie Y-J., Liu Z-M., Wang S-Y.: Flux enhancement for polypropylene microporous membrane in a SMBR by the immobilization of poly(*N*-vinyl-2-pyrrolidone) on the membrane surface. Journal of Membrane Science, **279**, 148–155 (2006). DOI: 10.1016/j.memsci.2005.11.046

[35] Adolfsson A., Caramella C., Nyström C.: The effect of milling and addition of dry binder on the interparticulate bonding mechanisms in sodium chloride tablets. The International Journal of Pharmaceutics, **160**, 187–195 (1998).
DOI: 10.1016/S0378-5173(97)00307-4

[36] ASTM D638-03: Standard test method for tensile properties of plastics (2004).

[37] ASTM D790-03: Standard test method for flexural properties of unreinforced and reinforced plastics and electrical insulating materials (2003).

[38] ASTM D256-90b: Standard test method for impact resistance of plastics and electrical insulating materials (2004).

[39] Chmielewski A. G., Haji-Saeid M., Ahmed S.: Progress in radiation processing of polymers. Nuclear Instruments and Methods in Physics Research B: Beam Interactions with Materials and Atoms, **236**, 44–54 (2005).
DOI: 10.1016/j.nimb.2005.03.247

[40] Ismail H., Rosnah N., Rozman H. D.: Curing characteristics and mechanical properties of short oil palm fibre reinforced rubber composite. Polymer International, **38**, 4059–4064 (1997).
DOI: 10.1016/S0032-3861(96)00993-7

[41] Karmarkar A., Chauhan S. S., Modak J. M., Chanda M.: Mechanical properties of wood-fibre reinforced polypropylene composites: Effect of a novel compatibiliser with isocyanate functional group. Composites Part A: Applied Science and Manufacturing, **38**, 227–233 (2007).
DOI: 10.1016/j.compositesa.2006.05.005

[42] Wong S., Shanks R., Hodzic A.: Interfacial improvements in poly(3-hydroxybutyrate)-flax fibre composites with hydrogen bonding additives. Composites Science and Technology, **64**, 1321–1330 (2004).
DOI: 10.1016/j.compscitech.2003.10.012

[43] Kim B. K., Choi C. H.: Melt blends of poly(methyl methacrylate) with a phenoxy. Polymer, **37**, 807–812 (1996).
DOI: 10.1016/0032-3861(96)87257-0

eXPRESS Polymer Letters Vol.3, No.4 (2009) 235–244
Available online at www.expresspolymlett.com
DOI: 10.3144/expresspolymlett.2009.30

Phase structure and tensile creep of recycled poly(ethylene terephthalate)/short glass fibers/impact modifier ternary composites

A. Pegoretti[1], J. Kolarik[2], M. Slouf[2]*

[1]Department of Materials Engineering and Industrial Technologies, and INSTM Research Unit, University of Trento, 38100 Trento, Italy
[2]Institute of Macromolecular Chemistry ASCR, v. v. i., 162 06 Prague 6, Czech Republic

Received 8 January 2009; accepted in revised form 25 February 2009

Abstract. Binary and ternary composites of recycled poly(ethylene terephtalate) (rPET), short glass fibres (SGF) and/or impact modifier (IM) were prepared by melt compounding and injection moulding. SEM images of rPET/IM fracture surfaces indicated that IM particles of about 1–2 μm in diameter were uniformly distributed in the rPET matrix, but with a poor adhesion level. Microphotographs of PET/SGF composites evidenced brittle fracture proceeding through the matrix and strong adhesion between components. In ternary composites SGF were evenly distributed, while IM particles were no longer detectable.
Tensile creep of rPET and prepared composites was investigated under short and long term testing conditions at various stress levels. Main part of the tensile creep corresponded to the elastic time-independent component, while the time-dependent component was rather limited even at relatively high stresses. While SGF accounted for a significant decrease in the overall creep compliance, the incorporation of IM induced a small decrease in the compliance and a non-linear viscoelastic behavior. In ternary composites, the reinforcing effects of SGF was dominating. Under a constant stress, the logarithm of compliance grew linearly with the logarithm of time. The creep rate, which resulted to be generally very small for all tested materials, was slightly reduced by SGF and increased by IM.

Keywords: *polymer composites, poly(ethylene terephthalate), recycling, creep*

1. Introduction

Due to the rapid growth in its use, poly(ethylene terephthalate) (PET) has become one of the most important engineering polymers in the past two decades [1, 2]. PET is used widely in several massive applications such as textile fibres for apparel, films for packaging, bottles and containers for beverage drinks [3]. While neat (non-reinforced) PET has a rather limited use as an engineering plastic, short fibre reinforced PET is increasingly adopted for high demanding applications, like automobile components, lighting products, power tools, material handling equipment, sporting goods and housewares [2]. As a result of environmental pressures and for economical reasons, several strategies have been explored for physical or chemical recycling of post-consumer PET waste [1, 4–6]. Physical recycling of PET waste usually involves melting of solid flakes or granules in an extruder for pelletization into chips or for direct melt processing into value-added product. Through melt compounding in a twin screw extruder, recycled PET (rPET) chips can be used to obtain engineering plastics

*Corresponding author, e-mail: Alessandro.Pegoretti@unitn.it

such as blends/alloys or fibre reinforced compounds [7–16].

Many applications of thermoplastics are limited by their poor dimensional stability under long-lasting dead loads (constant external forces). Thus, systematic studies of the creep stability over appropriate intervals of time, stress and temperature are of great practical importance [17, 18]. As generally known, the creep of thermoplastics can be reduced by various types of reinforcing agents. Short glass fibres rank among very efficient discontinuous reinforcements, but their incorporation is usually accompanied by a significant decrease in toughness (impact resistance). For this reason, ternary composites have been developed which combine the effects of reinforcing and toughening components [19–22]. In view of the wide structural variability of ternary composites, it is necessary to acquire detailed information on their mechanical (physical) properties in correlation to their composition. A deficiency of many thermoplastics, in particular crystalline ones, consists in non-linear viscoelastic behaviour, which means that the produced strain rises more than acting stress (the compliance rises with stress). In creep experiments it is manifested by creep rate increasing in the course of the exposition, particularly after long creep periods, say 1000–10 000 min.

The objective of this communication is to study (i) phase structure, (ii) short-term creep and (iii) long-term creep of recycled poly(ethylene terephthalate) (PET) and its binary and ternary composites containing short glass fibers (SGF) and/or impact modifier (IM).

2. Format for the creep compliance of thermoplastics

Creep strain $\varepsilon(t,\sigma,T)$ depending on time t, stress σ and temperature T is usually viewed as consisting of three components [17, 18], as shown by Equation (1):

$$\varepsilon(t,\sigma,T)=\varepsilon_e(\sigma,T)+\varepsilon_v(t,\sigma,T)+\varepsilon_p(t,\sigma,T) \tag{1}$$

where $\varepsilon_e(\sigma,T)$ is the elastic (instantaneous, time-independent) component, $\varepsilon_v(t,\sigma,T)$ is the viscoelastic (reversible, time-dependent) component, and $\varepsilon_p(t,\sigma,T)$ is the plastic (irreversible, time-dependent) component.

In practical applications of thermoplastics, the conditions should be avoided where $\varepsilon_p(t,\sigma,T) > 0$ because any plastic deformation usually accounts for irreversible damage of end-products. Therefore, the tensile compliance $D(t,\sigma,T) = \varepsilon(t,\sigma,T)/\sigma$ corresponding to reversible deformation reads as shown by Equation (2):

$$D(t,\sigma,T) = D_e(\sigma,T) + D_v(t,\sigma,T) \tag{2}$$

Storage of experimental creep data in a graphical form is impractical, though it is widely used [23]. If the creep curves can be fitted by an equation, then evaluation of the creep rate, interpolation or extrapolation of the creep deformation, and quantitative description of the effects of external variables are facilitated. The creep compliance is generally viewed as a product of independent functions of time or stress or temperature, i.e., $D(t,\sigma,T) = C_p\, g_1(t)\, g_2(\sigma)\, g_3(T)$, determined *a posteriori* by fitting experimental data. Of numerous empirical functions proposed for $g_1(t)$ and $g_2(\sigma)$, the Equation (3) was found suitable for both short- and long-term tensile creeps of polypropylene and its blends [24–26]:

$$D(t,\sigma)=W(\sigma)\left(\frac{t}{\tau_{rm}}\right)^n \tag{3}$$

where $W(\sigma)$ is a function of the stress, τ_{rm} is the mean retardation time, and $0 \le n \le 1$ is the creep curve shape parameter reflecting the distribution of retardation times. We assume that the retardation time τ_{rm} is controlled by the available fractional free volume whose changes obey the Equation (4):

$$\log a_\varepsilon(t)=\log\left[\frac{\tau_{rm}(f_2)}{\tau_{rm}(f_1)}\right] \tag{4}$$

where $\log a_\varepsilon(t)$ is a shift factor and $f_2 > f_1$ are the fractional free volumes related to deformations $\varepsilon_2 > \varepsilon_1$. Obviously, if the free volume changes are small during creep measurements, the value of $\log a_\varepsilon(t)$ is negligible.

Combining Equations (3) and (4) we obtain the Equation (5) [24]:

$$\log D(t,\sigma) = [\log W(\sigma) - n\log\tau_{rm} - n\log a_\varepsilon(t)] + n\log(t) = \log C(t,\sigma) + n\log(t) \tag{5}$$

3. Experimental

3.1. Materials

Recycled poly(ethylene terephthalate) (rPET) was produced by Eco Selekta Italia Srl (Salorno, Italy) from bottles used for beverages (density ISO 1183(A): 1.328 g/cm^3; MVR ISO 1133 = 115 ml/10 min; intrinsic viscosity ISO 1628-5 = 0.70 dl/g).

A commercial nucleating agent (Procaster by Polichem) was used (3.5 wt% related to rPET) in order to obtain fully crystallized rPET matrix under the selected moulding conditions.

Short (chopped strand) E-glass fibres (SGF) type 952 produced by Saint Gobain – Vetrotex were used as a reinforcing agent in percentage of 15 and 30 wt%. Filament diameter was 10 μm, fibre length 4.5 mm. The fibres are surface treated with a proprietary sizing agent specifically designed for thermoplastic polyester and polycarbonate resin systems. According to previous investigations [10], the fibre, added in the feeding zone of the extruder, degraded from their initial length to average fibre lengths of 0.71±0.14 mm and 0.55±0.08 mm for rPET-15GF and rPET-30GF, respectively.

A commercial core/shell acrylic impact modifier (IM) (Paraloid™ EXL by Rohm and Haas) was added (15 wt%) in some formulations to improve the impact properties of rPET and its composites.

All components, i.e., rPET, nucleating agent, short glass fibres and/or impact modifier, were mixed in a single screw extruder (Eco Extruder, model EEGT/35/L-D36/ESI) working at 160 rpm and at temperature in the range 280–310°C. Produced pellets were used for feeding a Sandretto injection moulding machine, model 310/95, (average barrel temperature range: 270–300°C; injection pressure: 20 MPa; mould temperature: 130°C) to produce ASTM D638 dumb-bell specimens (length: 210 mm; thickness: 3.3 mm; gauge length: 80 mm; gauge width: 12.8 mm) for the measurements of mechanical properties. Specimens used for creep studies were stored for more than six months at room temperature to avoid any interfering effect of the physical aging during measurements.

3.2. Electron microscopy

Injection moulded dumb-bell specimens were fractured in the middle of their length in liquid nitrogen. Fracture surfaces, which were perpendicular to the injection direction, were sputtered with a 4 nm layer of Pt in a vacuum sputter coater (SCD 050, Balzers) and observed in a scanning electron microscope (SEM; Vega TS 5130, Tescan). All SEM micrographs are secondary electron images, taken at 30 kV.

3.3. Tensile creep measurements

Tensile measurements were performed by using a home-made experimental apparatus equipped with a mechanical stress amplifier (lever) 11:1. The initial length of the test specimens was about 80 mm; their cross-section was 12.8 mm×3.3 mm. The displacement was measured with a mechanical gauge with an accuracy of about 2 μm, i.e., of about 0.0025%. Mechanical conditioning before each creep measurement consisted in applying a stress (for 1 min), which produced a strain larger than the expected final strain attained in the following measurement; the recovery period after the mechanical conditioning was more than 1 h. All creep tests were implemented at room temperature, i.e., 21–23°C.

Short-term tensile creep measurements in the interval 0.1–100 min were performed with one test specimen at four gradually increasing stress levels (between 5 and 30 MPa) in order to estimate the linearity limit between stress and strain. Each short-term creep measurement was followed by a 22 h recovery before another creep test (at an increased stress) was initiated. Long-term tensile creep experiments under a selected stress extended from 0.1 to 10 000 min.

4. Results and discussion

4.1. Phase structure of PET/SGF/IM composites

Microphotographs of the rPET/IM fracture surfaces (Figure 1a) show that IM particles of about 1–2 μm in diameter are uniformly distributed in the rPET matrix. The adhesion between rPET and IM is weak because imprints (holes) of many torn-off particles can be observed. Fracture surfaces of PET/SGF composites evidence (Figures 1b and 1c) that the brittle fracture mainly proceeds through the matrix. As no fractured (protruding) fibres or circular holes as imprints of pulled out fibres can be seen

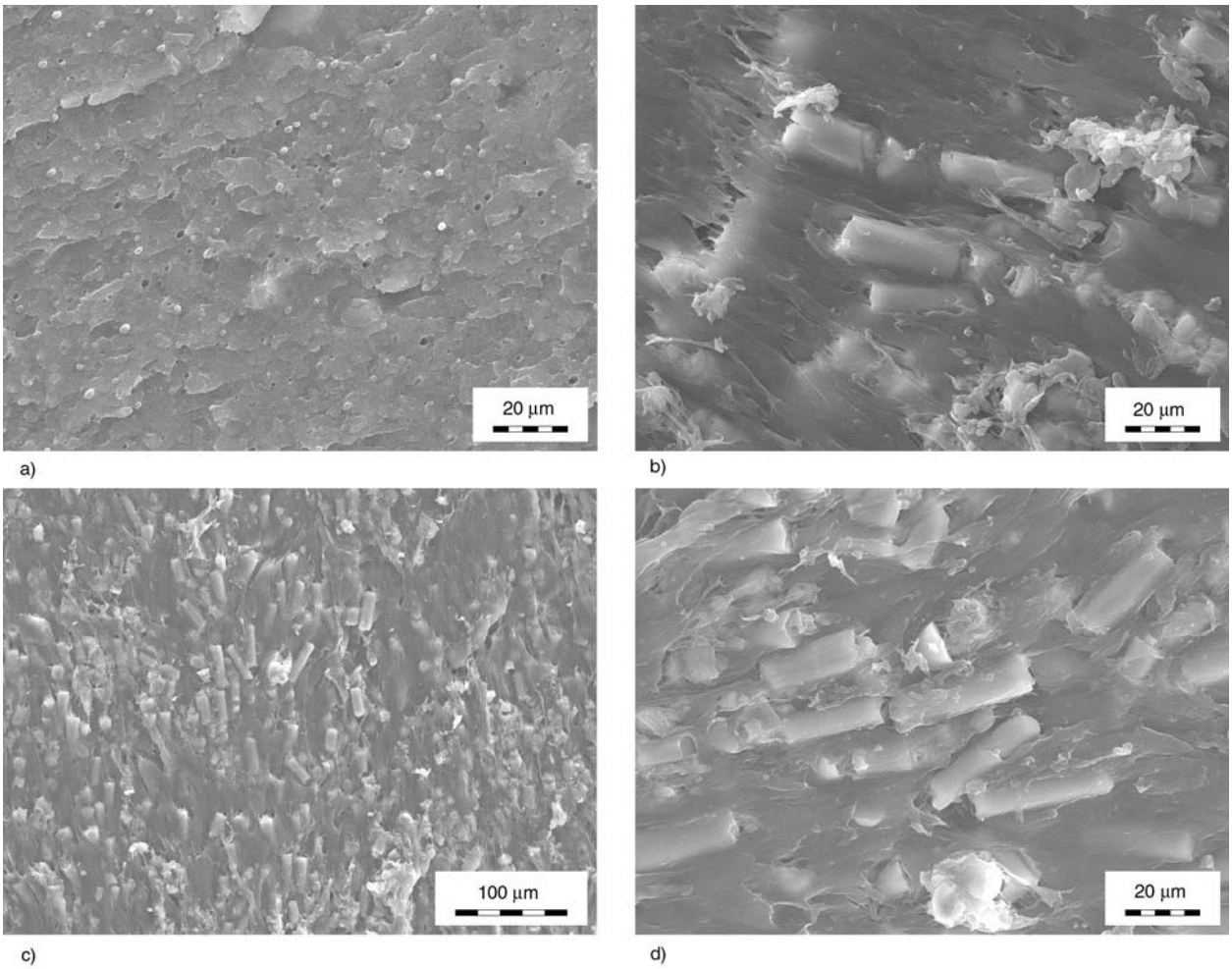

Figure 1. SEM microphotographs of fracture surfaces of binary systems: a) rPET/IM15; b) rPET/SGF15; c) and d) rPET/SGF30

on fracture surfaces, it is evident that the adhesion between rPET and SGF is strong. SEM images of fractured surfaces of ternary composites (Figure 2) clearly visualize SGF, while the identification of the IM particles is no longer possible, probably because the fracture path is controlled by SGF rather than IM particles. Other possible reasons could be related to the fact that the presence of glass fibers may induce higher shear stresses in the melt during compounding thus enabling a substantial reduction of the dimensions of IM particles below the resolution of the SEM observations. Moreover a localization of the IM at the fiber-matrix interface could also be supposed. As commonly encountered in injection moulded SGF reinforced thermoplastics [27], a skin-core microstructure was observed, with a prevalent orientation of SGF in the direction of injection moulding in the outer (skin) layers (see Figures 1d and 2c).

4.2. Short-term tensile creep of PET/SGF/IM composites

It can be expected that incorporation of a reinforcing component will increase the elastic modulus of the material and suppress viscoelastic character of the creep. With regard to expected lower compliance of the prepared composites, it was inevitable to perform the creep experiments at relatively high stresses in order to produce reasonable strains. Otherwise, the relative accuracy of creep measurements would be low and the effect of stress would remain unspecified, which would be a serious shortcoming from the viewpoint of possible applications. Therefore, this communication deals mainly with experiments performed at relatively high stresses, which may be of practical importance.

Tensile compliance $D(t)$ of rPET (Figure 3) is virtually independent of applied stress (up to 30 MPa), which indicates linear viscoelastic behavior. Main

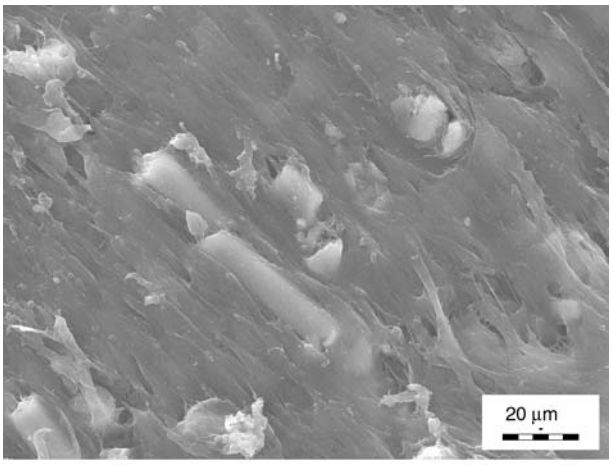

a)

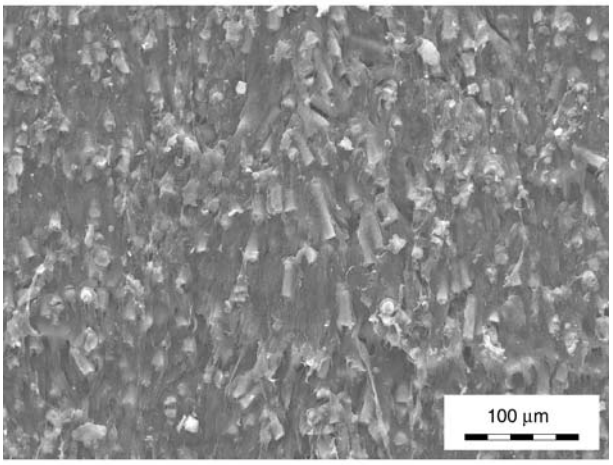

b)

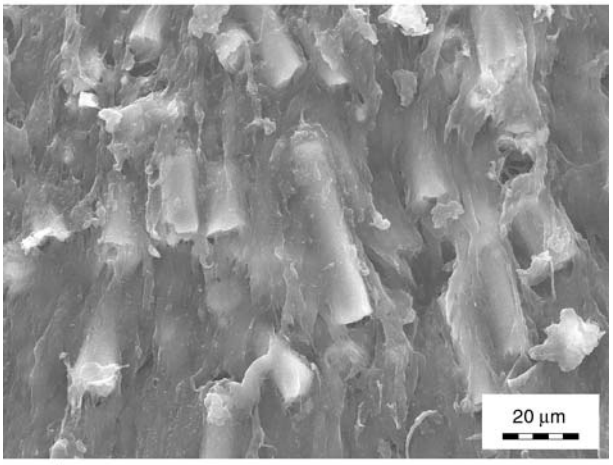

c)

Figure 2. SEM microphotographs of fracture surfaces of ternary composites: a) rPET/SGF15/IM15; b) and c) rPET/SGF30/IM15

part of the compliance corresponds to the elastic time-independent component, which occurs immediately after loading. Viscoelastic component $D_v(t)$ is low, representing only a few percent of $D(t)$; for this reason, the $D_v(t)$ vs. log t plots are somewhat irregular.

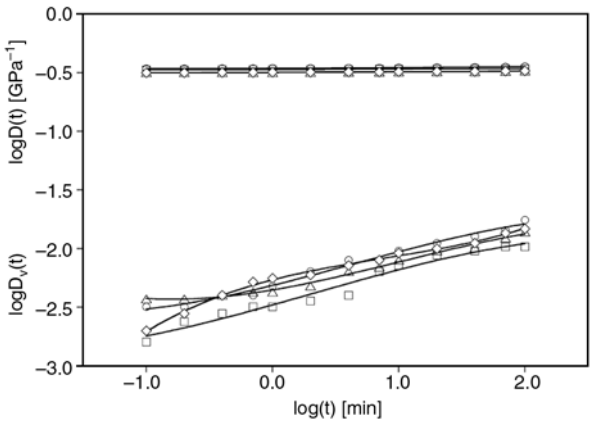

Figure 3. Short-term creep of rPET: effect of stress on compliance $D(t)$ (upper part) and its viscoelastic component $D_v(t)$ (lower part). Lines are polynomial regressions. Applied tensile stress [MPa]: (○) 7.40; (□) 14.81; (▽) 22.21; (◇) 29.62.

The effect of four selected stress levels on the time dependencies of $D(t)$ of binary and ternary systems is summarized in Figures 4–8 and in Table 1. As expected, the binary composites with 15 and 30 wt% of SGF (samples rPET/SGF15 and rPET/SGF30) have a much lower compliance than rPET, but they display stress-strain non-linearity because their compliance noticeably rises with applied stress. Also the creep rate characterized by the parameter n (Table 1) is higher than that found for the rPET matrix. On the other hand, the effect of applied stress on $D_v(t)$ is somewhat irregular, because the values of $D_v(t)$ are very low. In contrast, the incorporation of 15 wt% of IM into PET (sample rPET/IM15) brings about an increase in

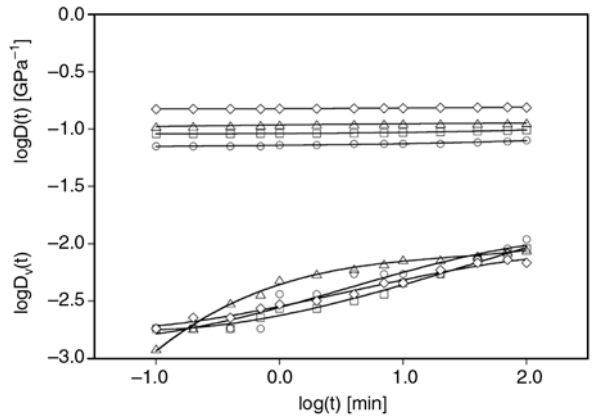

Figure 4. Short-term creep of rPET/SGF15: effect of stress on compliance $D(t)$ (upper part) and its viscoelastic component $D_v(t)$ (lower part). Lines are polynomial regressions. Applied tensile stress [MPa]: (○) 6.73; (□) 13.46; (▽) 20.19; (◇) 26.91.

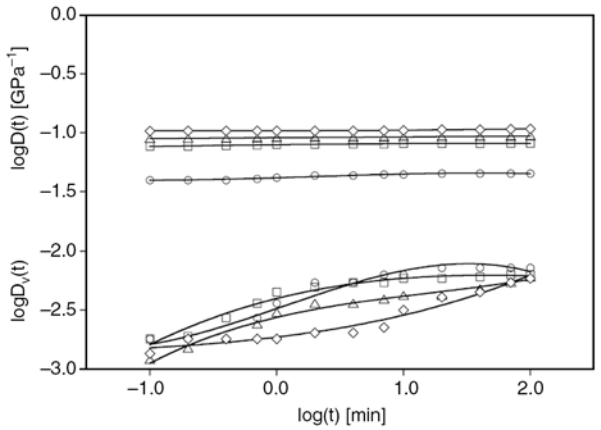

Figure 5. Short-term creep of rPET/SGF30: effect of stress on compliance $D(t)$ (upper part) and its viscoelastic component $D_v(t)$ (lower part). Lines are polynomial regressions. Applied tensile stress [MPa]: (○) 6.73; (□) 13.46; (▽) 20.19; (◇) 26.91.

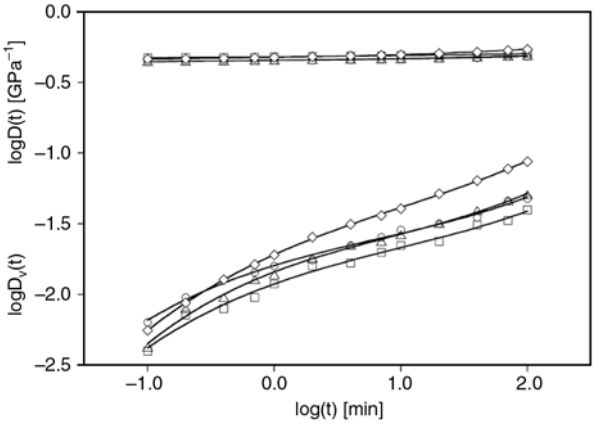

Figure 6. Short-term creep of rPET/IM15: effect of stress on compliance $D(t)$ (upper part) and its viscoelastic component $D_v(t)$ (lower part). Lines are polynomial regressions. Applied tensile stress [MPa]: (○) 7.47; (□) 14.94; (▽) 22.42; (◇) 29.89.

the compliance, but the latter is insensitive to the applied stress as it is observed for the neat rPET. However, the parameter n (Table 1) is much higher than that of rPET (although the absolute values of n still remain low), thus indicating an augmented creep rate.

Comparing the creep stability of the prepared composites we can say that the compliance of the ternary composites rPET/SGF15/IM15 and rPET/SGF30/IM15 is noticeably lower than that of rPET. Creep patterns of ternary composites are different from the previous ones in that they show decrease in $D(t)$ and $D_v(t)$ with rising stress (samples

Table 1. Effect of tensile stress on the parameters characterizing the short-term compliance of composites rPET/SGF/IM

Sample	SGF content [wt%]	IM content [wt%]	Applied stress [MPa]	log C	n	R^2
rPET	0	0	7.40	–0.4618	0.0057	0.9328
			14.81	–0.4733	0.0041	0.9371
			22.21	–0.4987	0.0045	0.9013
			29.62	–0.4972	0.0054	0.9732
rPET/SGF15	15	0	6.73	–1.1406	0.0164	0.8979
			13.46	–1.0369	0.0112	0.8781
			20.19	–0.9653	0.0100	0.9659
			26.91	–0.8217	0.0055	0.9457
rPET/SGF30	30	0	6.73	–1.3812	0.0226	0.9109
			13.46	–1.1039	0.0087	0.8906
			20.19	–1.0431	0.0071	0.9698
			26.91	–0.9824	0.0059	0.8327
rPET/IM15	0	15	7.47	–0.3437	0.0124	0.9588
			14.94	–0.3180	0.0098	0.9612
			22.42	–0.3425	0.0138	0.9613
			29.89	–0.3204	0.0228	0.9445
rPET/SGF15/IM15	15	15	7.47	–0.6046	0.0084	0.9289
			14.95	–0.6597	0.0065	0.9590
			22.42	–0.6812	0.0059	0.9578
			29.90	–0.6979	0.0073	0.9703
rPET/SGF30/IM15	30	15	7.40	–0.7426	0.0056	0.9487
			14.80	–0.8053	0.0055	0.8965
			22.20	–0.8580	0.0049	0.8892
			29.61	–0.8847	0.0080	0.9763

C, n: parameters of Equation (5); R: correlation coefficient

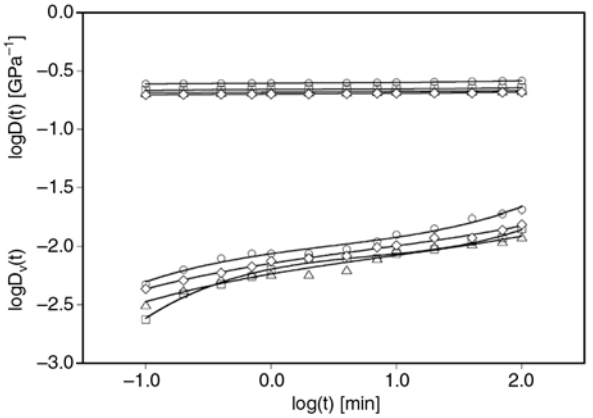

Figure 7. Short-term creep of rPET/SGF15/IM15: effect of stress on compliance $D(t)$ (upper part) and its viscoelastic component $D_v(t)$ (lower part). Lines are polynomial regressions. Applied tensile stress [MPa]: (O) 7.47; (□) 14.94; (▽) 22.42; (◇) 29.89.

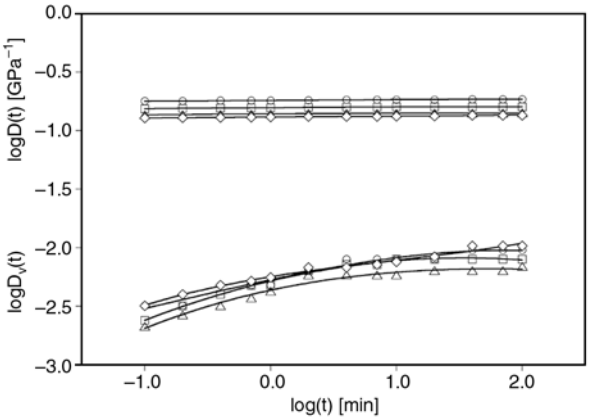

Figure 8. Short-term creep of rPET/SGF30/IM15: effect of stress on compliance $D(t)$ (upper part) and its viscoelastic component $D_v(t)$ (lower part). Lines are polynomial regressions. Applied tensile stress [MPa]: (O) 7.40; (□) 14.80; (▽) 22.20; (◇) 29.61.

rPET/SGF15/IM15 and rPET/SGF30/IM15). This effect is more pronounced in the composite with 30 wt% of SGF than in the composite with 15 wt% of SGF. Thus we can presume that the unexpected result could be related to a 'strain hardening' of the composite structure or to a strain-induced fibre orientation effect. In other words, the presence of IM seems to enhance strain hardening of single rPET macromolecules (orientation of single macromolecules of the polymer matrix) and/or strain-induced orientation of SGF (orientation of whole fibres in the matrix); these processes probably lead to energy dissipation and decrease in tensile compliance. The creep rate of ternary composites is decreasing as the SGF content increases, while the creep rate of rPET/SGF30/IM15 composites is virtually the same as rPET.

4.3. Long-term tensile creep of PET/SGF/IM composites

The results obtained for the long-term creep tests (Figures 9 and 10, Table 2) are in a good agreement with those obtained for the short-term creep. The compliance is substantially reduced by SGF and

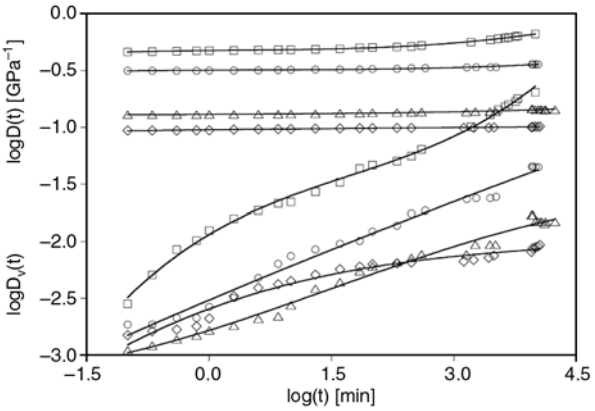

Figure 9. Long-term creep of rPET composites: effect of SGF and IM on compliance $D(t)$ (upper part) and its viscoelastic component $D_v(t)$ (lower part). Lines are polynomial regressions. (O) rPET, applied tensile stress 22.21 MPa; (□) rPET/IM15, applied tensile stress 20.82 MPa; (▽) rPET/SGF15, applied tensile stress 20.19 MPa; (◇) rPET/SGF30, applied tensile stress 20.19 MPa.

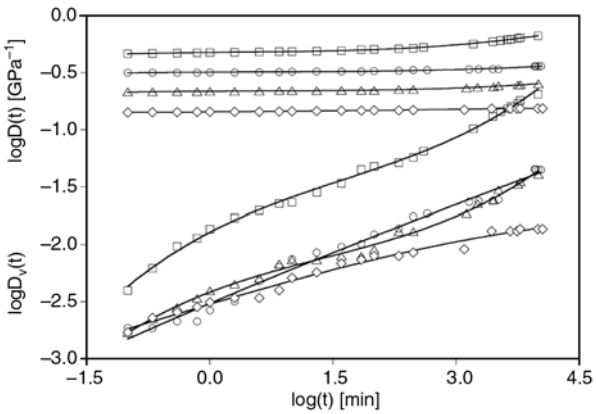

Figure 10. Long-term creep of rPET composites: effect of SGF and IM on compliance $D(t)$ (upper part) and its viscoelastic component $D_v(t)$ (lower part). Lines are polynomial regressions. (O) rPET, applied tensile stress 22.21 MPa; (□) rPET/IM15, applied tensile stress 20.82 MPa; (▽) rPET/SGF15/IM15, applied tensile stress 20.93 MPa; (◇) rPET/SGF30/IM15, applied tensile stress 20.72 MPa.

Table 2. Effect of the composition on the parameters characterizing the long-term compliance of composites rPET/SGF/IM

Sample	SGF content [wt%]	IM content [wt%]	Applied stress [MPa]	log C	n	R^2
rPET	0	0	22.21	–0.5008	0.0108	0.8384
rPET/SGF15	15	0	20.19	–0.8450	0.0081	0.8814
rPET/SGF30	30	0	20.19	–1.0219	0.0068	0.9600
rPET/IM15	0	15	20.92	–0.3326	0.0297	0.8581
rPET/SGF15/IM15	15	15	20.93	–0.6678	0.0128	0.8368
rPET/SGF30/IM15	30	15	20.72	–0.8442	0.0075	0.9640

noticeably enhanced by IM. Thus the composite with 30 wt% of SGF and 15 wt% of IM (rPET/SGF30/IM15) has approximately the same compliance as the composite with 15% of SGF (rPET/SGF15). The creep rate is also reduced by SGF, but markedly enhanced by IM. The creep rate of ternary composites decreases with the content of SGF, but its values are rather close the value found for rPET.

A noticeable upswing of the log$D(t)$ with log(t) plot for longer creep periods ($t > 1000$ min), which was typical of the rPET/IM blends described in a previous communication [8], can be seen also for the sample rPET/IM15. On the other hand, all composites (binary and ternary) containing SGF show a linear log$D(t)$ vs. log(t) dependence in almost all the measured time interval. Thus a positive effect of SGF can be seen in that the creep rate does not rise at long creep periods.

The recovery following the long-term creep would require extremely long periods of experimental time (about 70 days). As possible plastic deformation (flow) is proportional to the creep time, it should be 100 times larger in the long-term creeps than in the corresponding short-term creeps. While no permanent deformation was detected after the recovery of short-term creeps, a very small residual deformation (of selected specimens) was observed after 20 days of the recovery in the creep apparatus. Thus, we believe that no irreversible deformation was produced in the executed long-term creep experiments.

5. Conclusions

Microphotographs of the rPET/IM fracture surfaces showed that the IM particles of about 1–2 μm in diameter were uniformly distributed in the PET matrix, but their adhesion to PET was weak because imprints (holes) of many torn-off particles can be seen. Fracture surfaces of rPET/SGF composites evidenced brittle fracture mainly proceeding through the matrix. Absence of pulled out fibres confirmed strong adhesion between rPET and SGF. SEM images of fractured surfaces of ternary composites clearly visualized SGF evenly distributed, while the IM particles were no longer visible, probably because the paths of fracture surfaces was controlled by SGF rather than IM particles.

Main part of the tensile creep of rPET and prepared composites corresponded to the elastic time-independent component, while the time-dependent component was rather limited even at relatively high stresses. SGF accounted for a significant decrease in the compliance, non-linear stress-strain behaviour and a small increase in the creep rate. In contrast, the incorporation of IM provoked an increase in the compliance and creep rate, even if the linear viscoelastic behaviour of the rPET matrix was preserved.

In prepared ternary composites, the reinforcing effect of SGF was dominating. All composites containing SGF showed a linear log$D(t)$ vs. log$t$ dependence throughout the whole experimental time interval. Thus a positive effect of SGF could be seen in that the creep rate did not rise at long creep periods. The creep rate, which was generally very small for all tested materials, was slightly reduced by SGF and increased by IM. Creep patterns of the ternary composites rPET/SGF/IM showed a decrease in $D(t)$ and $D_v(t)$ with rising stress, which could be tentatively related to a 'strain hardening' of the composite structure.

References

[1] Awaja F., Pavel D.: Recycling of PET. European Polymer Journal, **41**, 1453–1477 (2005). DOI: 10.1016/j.eurpolymj.2005.02.005

[2] Aharoni S. M.: Probable future trends in various classes of thermoplastic polyesters. in 'Handbook of thermoplastic polyesters: Homopolymers, copolymers, blends, and composites' (ed.: Fakirov S.) Wiley, Weinheim, Vol 2, 1321–1338 (2002). DOI: 10.1002/3527601961.ch29

[3] Gupta V. B., Bashir Z.: PET fibers, films, and bottles. in 'Handbook of thermoplastic polyesters: Homopolymers, copolymers, blends, and composites' (ed.: Fakirov S.) Wiley, Weinheim, Vol 1, 317–388 (2002). DOI: 10.1002/3527601961.ch7a

[4] Karger-Kocsis J.: Recycling options for post-consumer PET and PET-containing wastes by melt blending. in 'Handbook of thermoplastic polyesters: Homopolymers, copolymers, blends and composites' (ed.: Fakirov S.) Wiley, Weinheim, Vol 2, 1291–1318 (2002). DOI: 10.1002/3527601961.ch28a

[5] Nadkarni V. M.: Recycling of polyesters. in 'Handbook of thermoplastic polyesters: Homopolymers, copolymers, blends, and composites' (ed.: Fakirov S.) Wiley, Weinheim, Vol 2, 1224–1249 (2002). DOI: 10.1002/3527601961.ch26

[6] Spychaj T.: Chemical recycling of PET: Methods and products. in 'Handbook of thermoplastic polyesters: Homopolymers, copolymers, blends, and composites' (ed.: Fakirov S.) Wiley, Weinheim, Vol 2, 1251–1290 (2002). DOI: 10.1002/3527601961.ch27

[7] Kolarik J., Pegoretti A.: Indentation creep of heterogeneous blends poly(ethylene-terephthalate)/impact modifier. Polymer Testing, **23**, 113–121 (2004). DOI: 10.1016/S0142-9418(03)00069-2

[8] Pegoretti A., Kolarik J., Gottardi G., Penati G.: Heterogeneous blends of recycled poly(ethylene terephthalate) with impact modifier: Phase structure and tensile creep. Polymer International, **53**, 984–994 (2004). DOI: 10.1002/pi.1488

[9] Pegoretti A., Kolarik J., Peroni C., Migliaresi C.: Recycled poly(ethylene terephthalate)/layered silicate nanocomposites: Morphology and tensile mechanical properties. Polymer, **45**, 2759–2767 (2004). DOI: 10.1016/j.polymer.2004.02.015

[10] Pegoretti A., Penati A.: Recycled poly(ethylene terephthalate) and its short glass fibres composites: Effects of hygrothermal aging on the thermo-mechanical behaviour. Polymer, **45**, 7995–8004 (2004). DOI: 10.1016/j.polymer.2004.09.034

[11] Pegoretti A., Penati A.: Effect of hygrothermal aging on the molar mass and thermal properties of recycled poly(ethylene terephthalate) and its short glass fibres composites. Polymer Degradation and Stability, **86**, 233–243 (2004). DOI: 10.1016/j.polymdegradstab.2004.05.002

[12] Dodds N., Gibson A. G., Huang Y. H., Walker R., Sharpe A., Porteous A.: Reinforced thermoplastic pipe using recycled PET reinforcement. Plastics Rubber and Composites, **34**, 324–328 (2005). DOI: 10.1179/174328905X59764

[13] de M. Giraldi A., Bartoli J. R., Velasco J. I., Mei L. H. I.: Glass fibre recycled poly(ethylene terephthalate) composites: Mechanical and thermal properties. Polymer Testing, **24**, 507–512 (2005). DOI: 10.1016/j.polymertesting.2004.11.011

[14] Giraldi A., de Jesus R. C., Mei L. H. I.: The influence of extrusion variables on the interfacial adhesion and mechanical properties of recycled PET composites. Journal of Materials Processing Technology, **162**, 90–95 (2005). DOI: 10.1016/j.jmatprotec.2005.02.046

[15] Cornier-Ríos H., Sundaram P. A., Celorie J. T.: Effect of recycling on material properties of glass-filled polyethylene terephthalate. Journal of Polymers and the Environment, **15**, 51–56 (2007). DOI: 10.1007/s10924-006-0045-0

[16] Kracalik M., Pospišil L., Šlouf M., Mikešova J., Sikora A., Šimonik J., Fortelný I.: Effect of glass fibers on rheology, mechanical properties of recycled thermal and PET. Polymer Composites, **29**, 915–921 (2008). DOI: 10.1002/pc.20467

[17] Nielsen L. E., Landel R. F.: Mechanical properties of polymers and composites. Marcel Dekker, New York (1994).

[18] Crawford R. J.: Plastics engineering. Elsevier, Amsterdam (1998).

[19] Wong S. C., Sui G. X., Yue C. Y., Mai Y-W.: Characterization of microstructures and toughening behavior of fiber-containing toughened nylon 6,6. Journal of Materials Science, **37**, 2659–2667 (2002). DOI: 10.1023/A:1015808814451

[20] Laura D. M., Keskkula H., Barlow J. W., Paul D. R.: Effect of rubber particle size and rubber type on the mechanical properties of glass fiber reinforced, rubber-toughened nylon 6. Polymer, **44**, 3347–3361 (2003). DOI: 10.1016/S0032-3861(03)00221-0

[21] Tjong S. C., Xu S. A., Mai Y. W.: Tensile deformation mechanism of polyamide 6,6/SEBS-g-MA blend and its hybrid composites reinforced with short glass fibers. Journal of Materials Science, **38**, 207–215 (2003).

[22] Garakani M. M., Arefazar A., Nazockdast H.: Study on morphological, rheological, and mechanical properties of PP/SEBS-MA/SGF hybrid composites. Journal of Applied Polymer Science, **104**, 2704–2710 (2007). DOI: 10.1002/app.25700

[23] Boyer H. E.: Atlas of creep and stress-rupture curves. ASM International, Metals Park (1988).

[24] Kolarik J.: Tensile creep of thermoplastics: Time-strain superposition of non-iso free-volume data. Journal of Polymer Science Part B: Polymer Physics, **41**, 736–748 (2003).
DOI: 10.1002/polb.10422

[25] Kolarik J., Pegoretti A., Fambri L., Penati A.: Prediction of non-linear long-term tensile creep of heterogeneous blends: Rubber-toughened polypropylene/ poly(styrene-co-acrylonitrile). Journal of Applied Polymer Science, **88**, 641–651 (2003).
DOI: 10.1002/app.11586

[26] Kolarik J., Fambri L., Pegoretti A., Penati A., Goberti P.: Prediction of the creep of heterogeneous polymer blends: Rubber-toughened polypropylene/ poly(styrene-co-acrylonitrile). Polymer Engineering and Science, **42**, 161–169 (2002).
DOI: 10.1002/pen.10937

[27] Karger-Kocsis J.: Microstructural aspects of fracture in polypropylene and its filled, chopped fiber and fiber mat reinforced composites. in 'Polypropylene. Structure, blends and composites' (ed.: Karger-Kocsis J.) Chapmann and Hall, London, Vol 3, 142–201 (1995).

eXPRESS Polymer Letters Vol.3, No.4 (2009) 245–255
Available online at www.expresspolymlett.com
DOI: 10.3144/expresspolymlett.2009.31

Diffusion behavior of water in polyamide 6 organoclay nanocomposites

N. Abacha[1*], *M. Kubouchi*[2], *T. Sakai*[3]

[1]Department of Chemical Engineering, Kyoto University, Kyoto university-Katsura, Nishikyo-ku, Kyoto 615-8510, Japan
[2]Department of Chemical Engineering, Tokyo Institute of Technology 2-12-1 O-okayama, Meguro-ku, Tokyo 152-8552, Japan
[3]Department of Industrial Engineering and Management, Nihon University 2-1 Izumi-cho 1-Chome, Narashino-shi, Chiba 275-8575, Japan

Received 1 December 2008; accepted in revised form 26 February 2009

Abstract. Research on polymer-layered silicate nanocomposites is currently an expanding field of study because they exhibit a wide range of improved properties over their unmodified starting polymers. Polyamide 6 (PA6)/organoclay nanocomposites have been prepared by exfoliating the organoclay montmorillonite via melt mixing. The exfoliation within the nanocomposites has been monitored using X-ray diffraction (XRD) and transmission electron microscopy (TEM). Water absorption of PA6 nanocomposites and its mechanical performance when saturated with water at temperatures ranging from 40 to 60°C were investigated.
It was found that the organoclay up to 8 wt% was completely exfoliated and well distributed within PA6 matrix as observed by TEM and XRD analysis. Addition of organoclay did not affect the crystallinity of PA6, and better mechanical performances were obtained. It was found that the barrier properties of the neat PA6 exhibited both higher diffusion coefficient and higher maximum water uptake as compared to the filled polymer. For all investigated temperatures the diffusion coefficient was found to decrease as function of organoclay loading. However, the maximum uptake was found to increase without reaching that of neat PA6. A relationship between temperature and diffusion coefficient was also established.

Keywords: *nanocomposites, organoclay, polyamide 6, diffusion, water absorption*

1. Introduction

In recent years, research on polymer nanocomposites has attracted great interest and is currently an expanding field of study due to the wide range of improved properties over their pristine polymers [1, 2]. These nanocomposites exhibit superior properties such as enhanced strength, reduced gas permeability, and improved flame retardancy [3].
Nylons or polyamides are high performance engineering materials; they are semi-crystalline thermoplastics with attractive physical and mechanical properties that provide a wide range of important end-use performances in many industrial applications.
An original report from the Toyota research team [1] demonstrated such thermal and mechanical properties achieved from polyamide 6 montmorillonite (MMT) composite while another report from Vaia *et al*. [4] suggested that it is possible to melt mix polymers with silicates.
One common property to all polyamides is that they are hygroscopic; they absorb water from the environment, both from the air and from liquid water. This is an important factor to be considered

*Corresponding author, e-mail: nabil.abacha@gmail.com

during material pre-selection, parts design, mechanical performance prediction and optimization. The equilibrium moisture content of PA6 at 23°C in a 50% relative humidity environment is around 2.5 wt% and at 100% relative humidity as high as 9 wt% [5].

In general, the moisture content in nylon is a key variable affecting processing (polymerization, compounding, molding, welding, etc.) and end-use performances (mechanical, dimensional, surface appearance, etc.). The absorbed water in polymer behaves as a plasticizer, which affects material properties such as strength, stiffness, decrease of T_g, modulus and yield stress, while elongation at break as well as toughness, and ductility increase.

PA6 is often filled with mineral fillers or short fibers such as glass, carbon or aramid fibers to increase the modulus. However, layered silicate nanocomposites provide several advantages compared to these traditional filled compounds, such as lower amounts of fillers, therefore, lower density, increased barrier properties, improved transparency and better surface appearance can be observed.

Nanocomposites consisting of exfoliated silicate layers in PA6 can be produced by *in-situ* polymerization, in which organically modified silicate layers were swollen by the monomer i.e. PA6 (or ε-caprolactam) and exfoliated during polymerization [6–8], or by dispersion in the melt state by high shear mixing in a twin-screw extruder [9, 10–11]. Because of the large aspect ratio and surface area of the exfoliated silicate layers they act as efficient barriers against transport through the material [12]. Despite the importance of the influence of moisture in practical applications, only a few papers containing data for mechanical properties of moisture-conditioned nanocomposites have been published [13, 14]. Hence, for a complete understanding of PA6 nanocomposites it is important to understand the mechanism of moisture absorption and its influence on nanocomposites' mechanical properties.

In this paper the influence of the amounts of layered silicate on water diffusion coefficient and maximum amount of absorbed water is described. In addition, the influence of penetrant uptake on the mechanical properties is measured and discussed.

2. Experimental

2.1. Materials and preparation method

A commercially available polyamide 6 (UBE1013B) provided from UBE Industries Ltd (Japan) was used as a test material. The organoclay I.34TCN was from Nanocor, Inc. (USA); it is a methyl dihydroxyethyl hydrogenated tallow ammonium treated montmorillonite.

The PA6/nanocomposites were prepared via melt mixing method. The PA6 and organoclay were mixed using a KRC-S1 co-rotating twin-screw extruder having an L/D = 10.2. The extruder was operated at temperature in the feeding zone of 150°C and in all other zones where heated to 240°C, the screw speed was set to 200 RPM. Different master batches having respectively 2, 4, 6, and 8 wt.% organoclay were thus prepared. The granules obtained by extrusion were injection molded in a laboratory injection molding machine to a rectangular shape having dimension 5×2×2 mm. Before any processing or testing specimens were dried in oven at 50°C for at least 100 hours to ensure that they reached a constant weight condition.

2.2. Sorption process

Diffusion behavior of deionized water was investigated by immersing the specimens in deionized water at 40, 50, and 60°C. Samples were periodically removed, wiped with filter paper to remove excess of the water and then kept at room temperature for 1h before the weight was recorded. This weight is considered to be the wet one. Further analyses were carried out immediately after weight was recorded. Water content was determined using the Equation (1):

$$M_t[\%] = \frac{W_t - W_0}{W_0} \cdot 100 \quad (1)$$

where M_t, W_t and W_0 are the water content at a given time, weight of the sample at the time of the measurement and initial weight, respectively.

2.3. Characterization

X-ray diffraction (XRD) experiments were performed on a Philips Xpert MPD PW3050 X-ray diffractometer with a CuK_α as a radiation source

(λ = 1.54 Å), operated at 40 kV and 30 mA. Samples were scanned at diffraction angles (2θ's) from 2 to 10° at a scan speed of 0.016°/s.

Transmission electron microscopy coupled to energy dispersive X-ray spectrometer TEM/EDS photographs were taken with a JEOL JEM 2010F using an acceleration voltage of 200 kV.

Three point bending test was done according to ASTM D790 using a Shimadzu Autograph AGS-1KNJ machine.

3. Results and discussion

3.1. Morphology

The X-ray diffraction patterns of organoclay and PA6-organoclay nanocomposites are shown in Figure 1 for the 2θ range from 1 to 9°. The XRD pattern relative to pristine organoclay displays a strong diffraction peak at 2θ = 5° corresponding to a basal spacing, d_{001}, of 18 Å. This peak is no more observed on the X-ray diffraction curves of nylon-6 nanocomposites containing up to 8 wt%. The disappearance of such peak within the nanocomposites samples revealed that up to these contents of organoclay, the silicate platelets were well dispersed and well exfoliated within the PA6 matrix.

The evolution of the silicate layers dispersion in the PA6 matrix as a function of the clay content is confirmed by TEM analysis (Figure 2).

A detailed morphological analysis of the nanocomposites has been carried out using TEM micrographs for sample containing 2 wt% (Figure 2), even if little amount of individual exfoliated sheets have been counted in the analysis, most of the tactoids do not contain more than five sheets. This result is consistent with the X-rays diffraction analysis.

The increase in exfoliation during melt processing is due to the stresses in the extruder that break the organoclay particles into stacks of platelets or tactoids which can be subsequently sheared apart to make smaller platelet stacks. Shear stresses are an important element in these events. Finally, TEM evidence suggests that the platelets on the surface

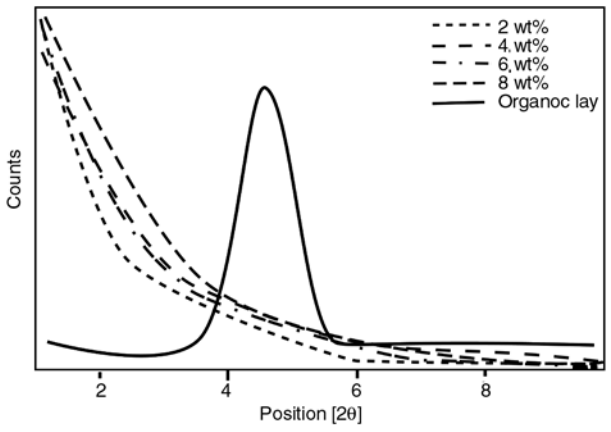

Figure 1. XRD patterns of the different PA6/organoclay nanocomposites

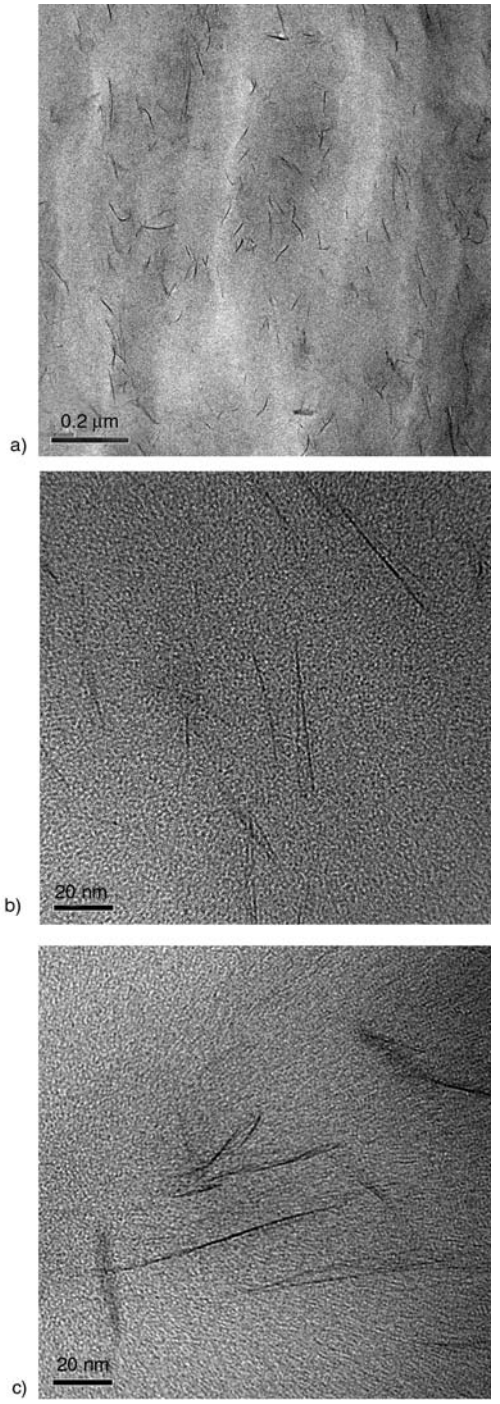

Figure 2. TEM micrograph of PA6 containing 2 wt% organoclay at different magnification

peel apart by a combination of diffusion of polymer chains and shear which is aided by the fact that individual platelets are not rigid but are quite able to bend away. Of course, the latter step only occurs if the polymer has some affinity for the organoclay surface (a property of both MMT and the organic treatment) and this process may require longer time.

3.2. Effects of clay on polyamide 6 crystallization

Crystalline lamellae are considered to be impermeable to small molecules. It is thus important to take into account any crystalline change in the polymer matrix in presence of clays in order to understand the evolution of the transport phenomenon. In this study, the crystalline structures of the neat PA6 and the PA6-based nanocomposites were investigated by X-ray diffraction (XRD) and differential scanning calorimeter (DSC).

One might expect that the small clay platelets would act as nucleating agents for crystallization of the PA6 matrix. PA6 crystallizes in either α or γ forms [15] resulting from different spatial arrangement in the hydrogen bonding between the oxygen in the carbonyl group of one chain and the hydrogen attached to the nitrogen in the neighboring chain, PA6 exhibits crystalline structure with two types of stable crystalline forms, monoclinic α-crystalline form and monoclinic γ-crystalline form [15, 16]. Formation of the γ-type crystals is favored by low temperatures, stress, and to some extent the presence of clay [17]. For injection-molded bars, the γ-form predominates in the skin, while a mixture of α and γ exist in the core [17].

It was found that the addition of silicates favored the formation of the γ-crystalline phase, suggesting that the formation of γ-crystalline phase of PA6 follows a heterogeneous nucleation mechanism [15]. From the point of view of spacing, the *d*-spacing of α-crystalline phase in the PA6/organoclay nanocomposites are larger than that of γ-crystalline phase in pure PA6, meaning that lattice arrangement in the PA6/organoclay nanocomposites is more ordered than that in pure PA6.

Figure 3 gives the XRD patterns of the injection-molded PA6 and its nanocomposites in the 2θ range from 4 to 40°. All curves showed a major diffraction peak at angular position 21.5°. This diffraction

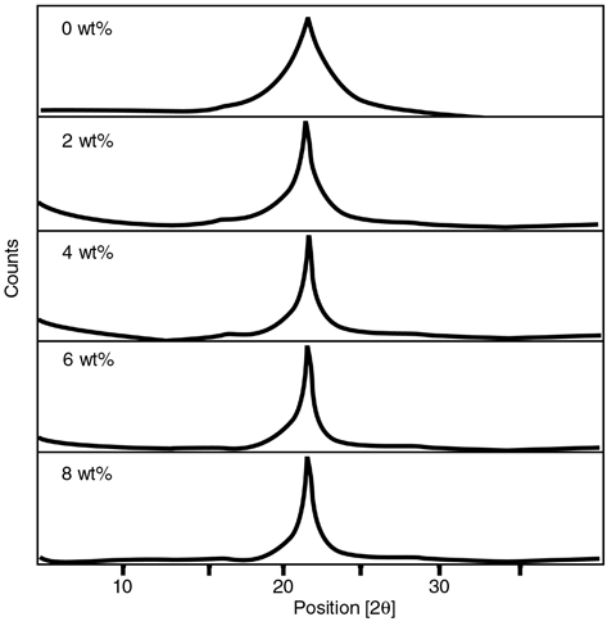

Figure 3. Wide XRD patterns of PA6/organoclay nanocomposites

peak can be assigned to the composition of (001) reflection of the PA6 γ-form crystals [18, 19]. However, it was not be possible to conclude if only γ phase exist and that the addition of the organoclay did not influence the crystallinity of PA6. All formulations present a single peak with different broadness as observed in Figure 3, thus, according to XRD results, it can be concluded that both α and γ phases coexist in the neat PA6 and nanocomposites. The introduction of the organoclay in polyamide matrix slightly enhances α-phase formation but does not lead to major modifications in the whole crystallinity index [19]. Nanocomposites containing commercially relevant concentrations of clay, i.e. 3–5 wt%, have comparable crystallization times and temperatures as the pure polyamide with a similar processing history [20].

DSC data were used to complete this qualitative analysis. Figure 4 shows the DSC scan of the neat PA6 and its nanocomposites. A larger endothermic peak could be observed at around $T = 226$°C which is associated with the melting of both α and γ form crystals of PA6 as compared to the neat PA6 which shows a single sharp peak. The broadness of the peak is due to the effect of the organoclay on the crystallinity of PA6 similar effect was reported by Picard *et al*. [20] where they found that the percent crystallinity was not affected by the addition of the organoclay however, Murase *et al*. [21] find that

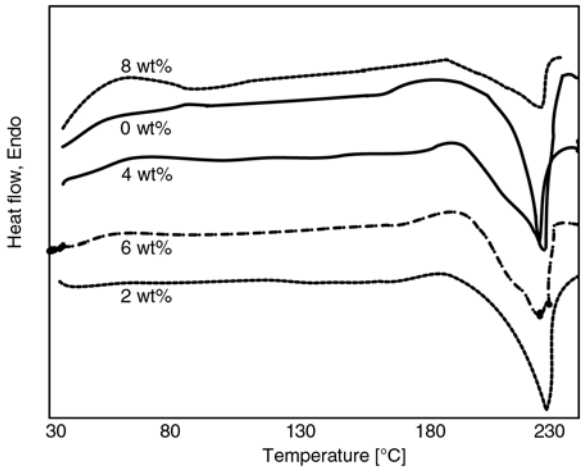

Figure 4. DSC thermograms of PA6/organoclay nanocomposites

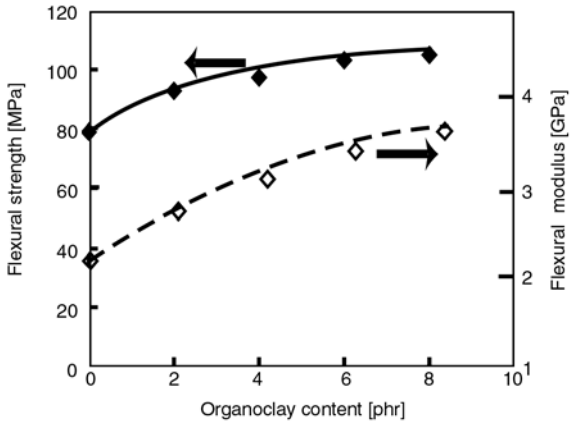

Figure 5. Flexural modulus and flexural strength of PA6 as function of organoclay content

crystallinity value of nylon-6 are much affected by the type of clay incorporated into the polyamide.

It can be concluded form both DSC and XRD measurement that no major modification of the PA6 crystallinity did occur by the introduction of the organoclay even if an alteration of the peak was observed which may be due to the increase of the γ phase. It is believed that the organoclay did not affect the crystallinity of the PA6 which may not alter the moisture absorption as the diffusion may just occur in the amorphous region of PA6 and not within the crystalline ones and the only effect will be the one of the organoclay and the way to prevent the diffusion of water within the matrix.

3.3. Strength evaluation

Three points bending test of neat PA6 and that of PA6/nanocomposites was performed, this bending test will help to evaluate the strength of specimens either before or when immersed in a specific water. It gives also an idea about the degree of degradation of the polyamide as well as the degree of enhancement of the organoclay. By measuring the mechanical properties one can determine the extent of damage that may be caused by the absorption of liquid within polymer. Knowing that this damage may be mainly due to the plasticizing effect, hence, the measurement of mechanical properties have to be done at both states: wet (sample immediately removed from the water) and dry state (immersed sample dried for enough time to enable complete drying). If the strength or modulus recovers to the initial state one can postulate that no degradation did occur on the other hand if recovery is not 100% achieved this will be attributed to the degradation of the sample. Addition of organoclay may enhance the mechanical properties and also avoid to some degree the degradation of the polymer matrix.

Nevertheless in this study just wet condition were measured, as shown in Figure 5 illustrating the flexural modulus and the flexural strength of the different formulations. It is observed that both flexural modulus and strength increased as the organoclay content increases, this is mainly due to the benefit of the clay as reinforcing agent and also to the well dispersion and exfoliation of the organoclay. This is may be due to the constraint of the polymer chains by their interaction with the clay surfaces [22].

The extent of the enhancement is directly related to the degree of exfoliation. For PA6, recent research has demonstrated that comparable levels of exfoliation and performance, at least in terms of stress-strain behavior, can be achieved by melt processing as found by the chemical approach [13]. It is important to appreciate that additional effects caused by matrix-filler interactions, including changes in matrix crystal structure or chain mobility, may also be involved because of the high surface areas and small dimensions. The increased modulus could be contributed to the reduced mobility of a constrained polymer phase close to the silicate layers. The large surface area of the exfoliated platelets is considered to be responsible for this constrained polymer phase with a higher modulus [23].

3.4. Diffusion behavior of water in PA6/organoclay nanocomposites

Polyamides are well known to be hygroscopic materials and that they absorb water easily even at room temperature.

Weight change of PA6 and PA6/organoclay nanocomposite as function of immersion time in deionized water at 40°C as function of square root time is shown in Figure 6. It is observed that after a linear increase, the equilibrium is reached at about 140 h of immersion time in the case of the immersion at 40°C. Similar behavior is observed at elevated temperature with shorter immersion time needed in order to reach the weight change equilibrium.

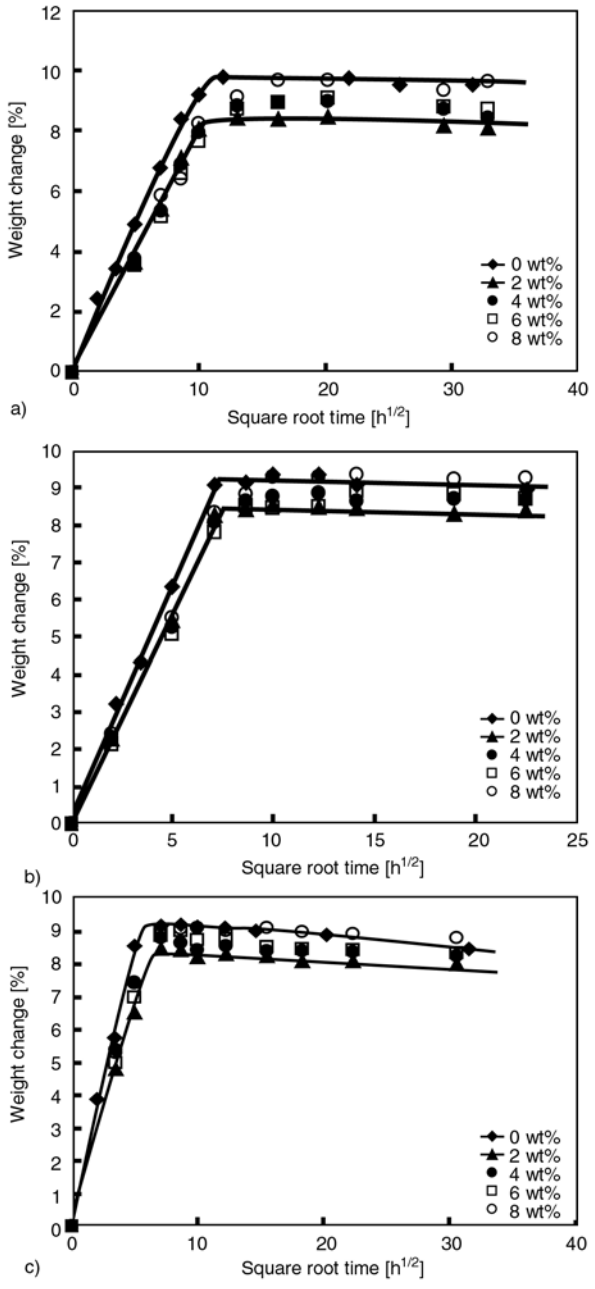

Figure 6. Weight change of PA6 and PA6/organoclay nanocomposites at a) 40°C, b) 50°C and c) 60°C

Moisture absorption is generally considered to be independent of moisture concentration, the diffusion of moisture is generally considered to obey Fick's law [24, 25], see Equation (2):

$$\frac{M_t}{M_\infty} = \left[1 - \sum_0^\infty \frac{8}{(2n+1)^2\pi^2} \exp\left(\frac{-D(2n+1)^2\pi^2 t)}{4l^2}\right)\right] \quad (2)$$

where M_t is the mass gain at reduced time and M_∞ is the maximum mass gain at the equilibrium state and l is half the thickness of the polymer sample.

The solution for Fick's law short times then reduces to the Equation (3) for the initial stage of diffusion:

$$\frac{M_t}{M_\infty} = 2\left(\frac{Dt}{\pi l^2}\right)^{1/2} \quad (3)$$

In the initial stage of the absorption, up to approximately $M_t/M_\infty = 0.5$ the increase in mass shows a linear relationship with the square root of time [26–28].

As observed, the plot of M_t/M_∞ vs. $t_{1/2}/2l$ is linear at the initial stage and the diffusivity can be calculated from its slope, hence, the diffusion behavior of water may be considered to follow the Fickian type diffusion. Diffusion coefficient could be determined from the slope of the normalized weight change using Equation (3).

Table 1 summarizes the diffusion coefficient at different temperatures. The diffusion coefficients D can be used to compare the diffusion rate in the unfilled polymer to the nanocomposites one, and to estimate how much time total moisture saturation of a sample takes, depending on the dimensions.

It is observed from the plotted data of the diffusion coefficient in Figure 7 that the diffusion coefficient decreased as the amount of organoclay increased, according to the values are reported in Table 1 the diffusion coefficient falls to about a half in the case of immersion at 40°C, on the other hand the equilibrium weight change is not so much affected, the highest decrease is obtained with the lowest filling content, and as the organoclay content increases this equilibrium increases even despite the fact that it remains below that of the unfilled PA6. These

Table 1. Diffusion parameter for PA6 and PA6/organoclay nanocomposites

Formulation	40°C		50°C		60°C	
	M_∞ [%]	D [m^2/s]·10^{-12}	M_∞ [%]	D [m^2/s]·10^{-12}	M_∞ [%]	D [m^2/s]·10^{-12}
0 wt%	9.547454	2.25693	9.356305	3.81366	9.004974	7.91952
2 wt%	8.259288	1.86913	8.433146	3.77303	8.152024	5.44119
4 wt%	8.759826	1.56598	8.728609	3.29763	8.401829	6.47927
6 wt%	8.876960	1.36672	8.672343	2.99715	8.606046	5.24040
8 wt%	9.564869	1.25389	9.282899	2.95311	9.000577	5.31154

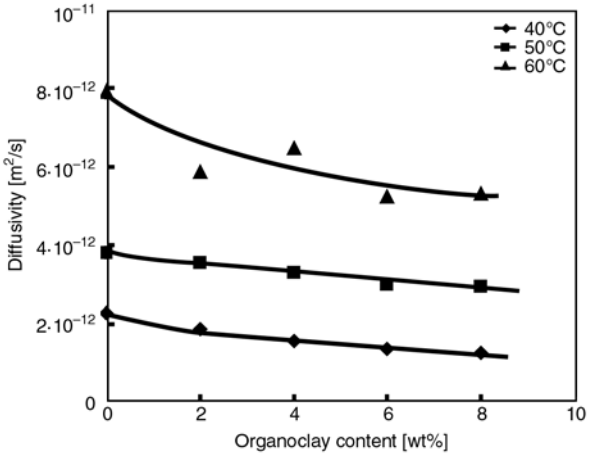

Figure 7. Diffusion coefficient at different temperature as function of organoclay content

results point to the effect of hydrophilic clay on the equilibrium water uptake i.e. even if the clay is treated to be hydrophobic and organically treated to have the ability to exfoliate within the polymer matrix some of the hydrophilicity may remain, that will attract water and thus the final water absorption may reach that of the unfilled polymer when considering longer immersion time.

The excellent resistance to water permeation of the PA6 organoclay nanocomposites is caused mainly by the decrease in diffusion coefficient (D) compared with nylon-6. A dispersion of impermeable filler and crystallite decrease the diffusion coefficient by increasing the average path length required to transport the specimen [29].

The rate of water absorption in PA6 nanocomposites is reduced compared to the unfilled polymer because of the impermeable silicate layers in the polymer. These layers increase the path-length for diffusion through the polymer. The increase in the path length predicts better barrier properties for nanocomposites. The maximum amount of water that can be absorbed by PA6 nanocomposites is not too much reduced; only the rate of absorption is reduced due to the lower diffusion coefficient [29, 30].

The speed of water absorption in PA6 nanocomposites is reduced compared to the unfilled polymer because of the impermeable silicate layers in the polymer. These layers increase the path-length for diffusion through the polymer [30]. This increased path length predicts the better barrier properties of nanocomposites very well [31]. In PA6 the water is absorbed in the amorphous phase, because the crystalline part is inaccessible for water [30]. The amorphous fraction is not much different in nanocomposites as evidenced by XRD and DSC and therefore the amount of absorbed water can reach approximately the same level as in unfilled polyamide, if sufficient time is available [30].

Temperature plays a very important role in the diffusion of penetrant molecules through polymeric membranes. Diffusion, like reaction rates, may be thought of as an activated process following an expression of the Arrhenius form given by Equation (4):

$$D = D_0 \exp\left(-\frac{E_D}{RT}\right) \tag{4}$$

where the activation energy E_D depends on the polymer and size of the penetrant. The diffusion behavior is found to be temperature dependent as illustrated in Figure 8. It is found that the coefficient of diffusion becomes lower as temperature decreases, diffusion coefficient can be formulated as: $D_T = 0.0025e^{-6528.9/T}$ where D_T is the diffusion coefficient [m^2/s] and T is temperature [K].

Activation energy (E) could be estimated from the diffusion coefficient equation (Equation (4)) the data are reported in Table 2. It is found that the activation energy globally increases as the organoclay content increases.

Table 2. Activation energy for PA6 and PA6/organoclay nanocomposites

Formulation	Activation energy E [kJ/mol]
0 wt%	54.28
2 wt%	46.43
4 wt%	61.54
6 wt%	58.31
8 wt%	62.65

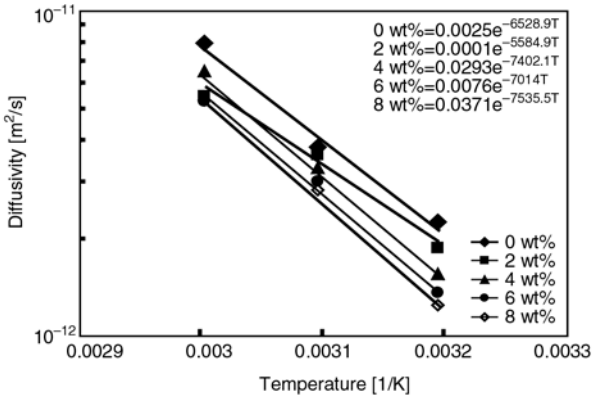

Figure 8. Relation between diffusivity and temperature of PA6/organoclay nanocomposites

It noticed that the diffusion coefficient increases as function of the immersion temperature; this is due to the fact that increasing the temperature leads to a decrease of the interaction energy. Exception is observed for the data 2 wt% where a decrease is observed this mainly due to the fact that at this concentration and at immersion temperature of 60°C showed the lowest diffusion coefficient, which did alter the calculation of the activation energy done via curve fitting as seen in Figure 8.

In the case of the PA6/organoclay nanocomposites, there are mainly two interaction groups: the interaction of water molecules with the amide groups of the PA6, i.e. matrix and the interaction of water molecules with the hydrophilic clay group i.e. the filler. Although the clay has been modified to be more organophilic, it may still interact and bind to water molecules, even if, this interaction does not dominate the sorption process of water in the nanocomposites.

3.5. Influence of water on mechanical properties

The evaluation of the mechanical properties in terms of bending test showed that an increase in both modulus and strength occurred in the dry condition, however, the tests under wet condition are performed on samples that are immediately removed immersion test.

Figure 9 illustrates the retention of the flexural strength of PA6 and that of PA6/organoclay nanocomposites as function of immersion time and at different immersion temperature. It is noticed a sharp decrease in the flexural strength as well as in the flexural modulus (not reported in this paper). This decrease levels off within about 25 h in the case for all investigated temperature which clearly shows the sensitivity of the PA6 towards water content. Nevertheless the presence of the organoclay may retain higher flexural strength as seen in Figure 9b (magnification of Figure 9a) it is observed that the neat PA6 has the lowest retention of the flexural strength as compared to the filled.

It is known that the absorbed moisture decreases T_g of PA6 and other polyamides because the water molecules interfere with the hydrogen bonds between the polymer chains and this increases the chain mobility. The reduced T_g in the presence of water results in a strong reduction of the amorphous modulus in the temperature range around T_g, which leads to a decrease of the modulus of the semi-crystalline polymer. Because of the reduction of the matrix modulus, also polyamide nanocomposites suffer from a modulus reduction after moisture conditioning. In addition, the increased mobility reduces the yield stress and increases the ductility and elongation at break.

The loss of mechanical performance i.e. the decrease in the flexural modulus occurs early in the diffusion process with the maximum loss realized much in advance of saturation. Initial uptake of water results in plasticization of the polymer matrix such that further ingression of water into the void spaces within the sample does not significantly alter the mechanical performance. The initial loss of performance, prior to the plateau, may be associated with the diffusion front progression through the sample. Further weight gain after this point may be attributed to the continued filling of voids spaces with water.

When the samples are moisture conditioned, the modulus of PA6 and the nanocomposites is significantly reduced. The reduction of the modulus in the presence of water is common to all polyamides to a certain degree, and it is caused by the plasticizing action of water molecules in polyamides [32] PA6

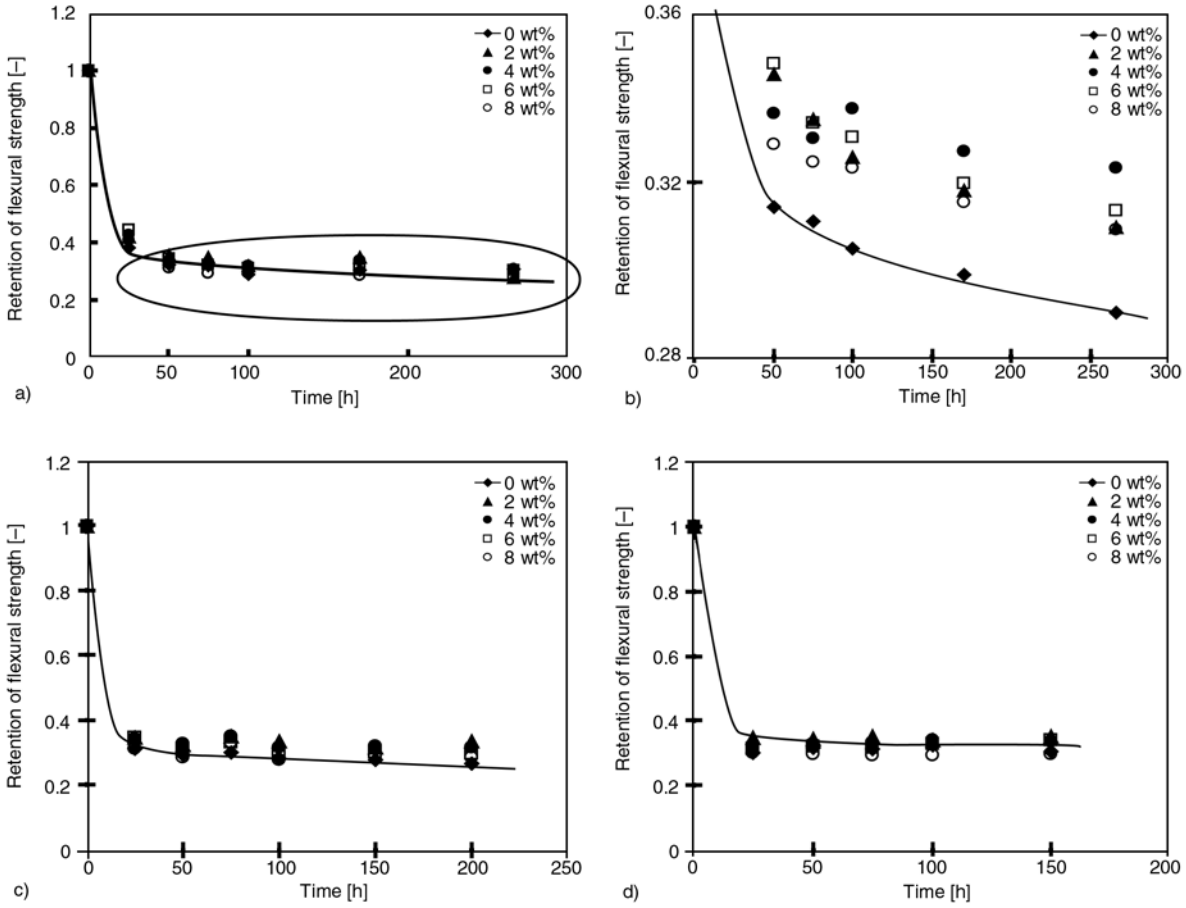

Figure 9. Retention of flexural strength of PA6/organoclay nanocomposites – wet condition – as function of immersion time at: a) and b) 40°C, c) 50°C and (d) 60°C

has a glass transition temperature around 60°C in dry conditions, but in moisture conditioned samples this can decrease to room temperature and below [33].

4. Conclusions

The investigation of the formation of a nanocomposites structure of the dispersed organoclay within PA6 matrix was done in addition to the study of the behavior of the diffusion of water within these nanocomposites materials. It was found that the organoclay was fully exfoliated and well dispersed within PA6 matrix for all the investigated organoclay content. An enhancement of the mechanical performance as function of organoclay content was obtained in terms of bending test where an increase of both flexural strength and flexural modulus were obtained. The immersion into water revealed that lower maximum weight change is obtained when immersed into water and that the diffusion coefficient of water is decreased by a half at some condition however the weight change was found to increase as function of organoclay content but remains lower than the neat resin. Better mechanical properties were achieved with the addition of organoclay and despite the sharp decrease in the mechanical properties of the immersed sample, the nanocomposites ones showed higher retention compared to the neat PA6.

References

[1] Usuki A., Kojima Y., Kawasumi M., Okada M., Fukushima Y., Kurauchi T., Kamigaito O.: Synthesis of nylon 6-clay hybrid. Journal of Materials Research, **8**, 1179–1184 (1993).
DOI: 10.1557/JMR.1993.1179

[2] Wang M. S., Pinnavaia T.: Clay-polymer nanocomposites formed from acidic derivatives of MMT and an epoxy resin. Chemistry of Materials, **6**, 468–474 (1994).
DOI: 10.1021/cm00040a022

[3] Lan T., Pinnavaia T.: Clay-reinforced epoxy nanocomposites. Chemistry of Materials, **6**, 2216–2219 (1994).
DOI: 10.1021/cm00048a006

[4] Vaia R. A., Ishii H., Giannelis E. P.: Synthesis and properties of two-dimensional nanostructures by direct intercalation of polymer melts in layered silicates. Chemistry of Materials, **5**, 1694–1696 (1993). DOI: 10.1021/cm00036a004

[5] Devaux E., Bourbigot S., Achari A. E.: Crystallization behavior of PA-6 Clay nanocomposite hybrid. Journal of Applied Polymer Science, **86**, 2416–2423 (2002). DOI: 10.1002/app.10920

[6] Kojima Y., Usuki A., Kawasumi M., Okada A., Kurauchi T., Kamigaiyo O.: Synthesis of nylon 6-clay hybrid by MMT intercalated with ε-caproalctum. Journal of Polymer Science Part A: Polymer Chemistry, **31**, 983–986 (1993). DOI: 10.1002/pola.1993.080310418

[7] Kojima Y., Usuki A., Kawasumi M., Okada A., Kurauchi T., Kamigaiyo O.: One-pot synthesis of nylon 6-clay hybrid. Journal of Polymer Science Part A: Polymer Chemistry, **31**, 1755–1758 (1993). DOI: 10.1002/pola.1993.080310714

[8] Kojima Y., Usuki A., Kawasumi M., Okada A., Fukushima Y., Kurauchi T., Kamigaiyo O.: Mechanical properties of nylon 6-clay hybrid. Journal of Materials Research, **8**, 1185–1189 (1993). DOI: 10.1557/JMR.1993.1185

[9] Akkapeddi M. K.: Glass fiber reinforced polyamide-6 nanocomposites. Polymer Composites, **21**, 576–585 (2000). DOI: 10.1002/pc.10213

[10] Kohan M. I.: Nylon plastics handbook. Hanser Verlag, Munich (1995).

[11] Vaia R. A., Giannelis E. P.: Polymer melt intercalation in organically-modified layered silicates: Model predictions and experiment. Macromolecules, **30**, 8000–8009 (1997). DOI: 10.1021/ma9603488

[12] Giannelis E. P.: Polymer-layered silicate nanocomposites. Advanced Materials, **8**, 29–35 (1996). DOI: 10.1002/adma.19960080104

[13] LeBaron P. C., Wang Z., Pinnavaia T. J.: Polymer-layered silicate nanocomposites: An overview. Applied Clay Science, **15**, 11–29 (1999). DOI: 10.1016/S0169-1317(99)00017-4

[14] Kawasumi M., Hasegawa N., Kato M., Usuki A., Okada A.: Preparation and mechanical properties of polypropylene-clay hybrids. Macromolecules, **30**, 6333–6338 (1997). DOI: 10.1021/ma961786h

[15] Jiang T., Wang Y-H., Yeh J-T., Fan Z-Q.: Study on solvent permeation resistance properties of nylon6/clay nanocomposite. European Polymer Journal, **41**, 459–466 (2005). DOI: 10.1016/j.eurpolymj.2004.10.024

[16] Holmes D. R., Bunn C. W., Smith D. J.: The crystal structure of polycaproamide: Nylon 6. Journal of Polymer Science, **17**, 159–177 (1955). DOI: 10.1002/pol.1955.120178401

[17] Jacobs P. M., Jones F. R.: Diffusion of moisture into two-phase polymers. Journal of Materials Science, **24**, 2331–2336 (1989). DOI: 10.1007/BF00638044

[18] Abastari, Sakai T., Sembokuya H., Kubouchi M., Tsuda K.: The reciprocal influence between ion transport and degradation of PA66 in acid solution. Polymer Degradation and Stability, **91**, 2595–2604 (2006). DOI: 10.1016/j.polymdegradstab.2006.05.018

[19] Picard E., Vermogen A., Gérard J-F., Espuche E.: Barrier properties of nylon 6-montmorillonite nanocomposites membranes prepared by melt blending: Influence of the clay content and dispersion state. Journal of Membrane Science, **292**, 133–144 (2007). DOI: 10.1016/j.memsci.2007.01.030

[20] Fornes T. D., Paul D. R.: Crystallization behavior of nylon 6 nanocomposites. Polymer, **44**, 3945–3961 (2003). DOI: 10.1016/S0032-3861(03)00344-6

[21] Murase S., Inoue A., Miyashita Y., Kimura N., Nishio Y.: Structural characteristics and moisture sorption behavior of nylon-6/clay hybrid films. Journal of Polymer Science Part B: Polymer Physics, **40**, 479–487 (2002). DOI: 10.1002/polb.10106

[22] Shelley J. S., Mather P. T., DeVries K. L.: Reinforcement and environmental degradation of nylon-6/clay nanocomposites. Polymer, **42**, 5849–5858 (2001). DOI: 10.1016/S0032-3861(00)00900-9

[23] Vlasveld D. P. N., Groenewold J., Bersee H. E. N., Mendes E., Picken S. J.: Analysis of the modulus of polyamide-6 silicate nanocomposites using moisture controlled variation of the matrix properties. Polymer, **46**, 6102–6113 (2005). DOI: 10.1016/j.polymer.2005.04.087

[24] Crank J.: The mathematics of diffusion. Clarendon Press, Oxford (1956).

[25] Crank J., Park G. S.: Diffusion in polymer. Academic Press Londonn (1968).

[26] Weiping L., Hoa S. V., Pugh M.: Water uptake of epoxy-clay nanocomposites: Model development. Composites Science and Technology, **68**, 156–163 (2008). DOI: 10.1016/j.compscitech.2007.03.041

[27] Kim J-K., Hu C., Ricky S. C. W., Sham M-L.: Moisture barrier characteristics of organoclay-epoxy nanocomposites. Composites Science and Technology, **65**, 805–813 (2005). DOI: 10.1016/j.compscitech.2004.10.014

[28] Abacha N., Kubouchi M., Sakai T., Tsuda K.: Diffusion behavior of water and sulfuric acid in epoxy/organoclay nanocomposites. Journal of Applied Polymer Science, **112**, 1021–1029 (2009). DOI: 10.1002/app.29482

[29] Kojima Y., Usuki A., Kawasumi M., Okada A., Kurauchi T., Kamigaiyo O.: Sorption of water in nylon 6-clay hybrid. Journal of Applied Polymer Science, **49**, 1259–1264 (1993).
DOI: 10.1002/app.1993.070490715

[30] Vlasveld D. P. N., Groenewold J., Bersee H. E. N., Picken S. J.: Moisture absorption in polyamide-6 silicate nanocomposites and its influence on the mechanical properties. Polymer, **46**, 12567–12576 (2005).
DOI: 10.1016/j.polymer.2005.10.096

[31] Vlasveld D. P. N., Groenewold J., Bersee H. E. N., Mendes E., Picken S. J.: Analysis of the modulus of polyamide-6 silicate nanocomposites using moisture controlled variation of the matrix properties. Polymer, **46**, 6102–6113 (2005).
DOI: 10.1016/j.polymer.2005.04.087

[32] Struik L. C. E.: The mechanical and physical ageing of semicrystalline polymers: 1. Polymer, **28**, 1521–1533 (1987).
DOI: 10.1016/0032-3861(87)90353-3

[33] Kohan M. I.: Nylon plastics handbook. Hanser, Munich (1995).

eXPRESS Polymer Letters Vol.3, No.4 (2009) 256–266
Available online at www.expresspolymlett.com
DOI: 10.3144/expresspolymlett.2009.32

Zinc chelates as new activators for sulphur vulcanization of acrylonitrile-butadiene elastomer

M. Przybyszewska[1], M. Zaborski[1], B. Jakubowski[2], J. Zawadiak[2]*

[1]Institute of Polymer and Dye Technology, Technical University of Lodz, Stefanowskiego 12/16, Lodz 90-924, Poland
[2]Department of Chemistry, The Silesian University of Technology, Krzywoustego 4, Gliwice 44-100, Poland

Received 12 January 2009; accepted in revised form 26 February 2009

Abstract. The goal of this work was to apply several zinc chelates as activators for sulphur vulcanization of acrylonitrile-butadiene elastomer (NBR), in order to find alternatives for the conventionally used zinc oxide. In this article, we discuss the effects of different zinc complexes on the cure characteristics, crosslinks distribution in the elastomer network and mechanical properties of acrylonitrile-butadiene rubber.
Zinc chelates seem to be good substitutes for zinc oxide as activators for sulphur vulcanization of NBR rubber, without detrimental effects on the crosslinking process and physical properties of the obtained vulcanizates. Moreover, application of zinc complexes allows to reduce the amount of zinc ions in rubber compounds by 40% compared to conventionally crosslinked vulcanizates with zinc oxide. It is a very important ecological goal since zinc oxide is classified as toxic to aquatic species and its amount in rubber products must be reduced below 2.5% at least. From a technological point of view it is a very important challenge.

Keywords: *rubber, nanocomposites, networks, vulcanization, zinc complexes*

1. Introduction

Zinc is one of the most widespread metals on Earth. It occurs naturally in the environment at moderate levels and is essential for humans to function properly. Its deficiency in the human body has a detrimental effect on growth and immunity. However, there are some aquatic species that seem very sensitive to zinc ions, so some soluble zinc compounds have been classified as toxic to aquatic species.
Since April 2004, the European Union has classified zinc oxide (ZnO) as dangerous for the environment and has legislated that its application in rubber technology be reduced and controlled [1]. From an ecological point of view, ZnO content must be kept as low as possible.
Zinc oxide is one of the basic components of rubber compounds. It acts as an activator for rubber crosslinking by sulphur or sulphur donors [2, 3], increasing the amount of bound sulphur and the efficiency of the crosslinking system [4]. The mechanism of the crosslinking process in the presence of ZnO is well known: it reacts with accelerators to form highly active zinc salt [5]. Complexes of Zn^{2+} ions with accelerators are believed to be more reactive than the free accelerator and allow sulphur insertion to occur more rapidly [6]. Next, the complexes interact with sulphur or sulphur donors, generating the active sulphurating agent, which reacts with allylic sites of rubber chains to form crosslink precursors [7]. Forming these rubber bound intermediates is a key stage in accelerated sulphur vulcanization. The crosslink precursor can react with another polymer chain to generate a crosslink.

*Corresponding author, e-mail: magdalena.przybyszewska@p.lodz.pl

There is discussion about the role of ZnO in the crosslinking process. According to Nieuwenhuizen [8], the surface of ZnO acts both as a reactant and a catalytic reaction template, by activating and bringing together reactants. The particles of accelerators, sulphur, and fatty acids diffuse through the polymer matrix and are adsorbed on the surface of zinc oxide, forming intermediate complexes. From this point of view, the dispersion of ZnO in the elastomer matrix is the most important parameter. Mark *et al.* [9] proved that adding zinc oxide affects different stages of the vulcanization process. It increases the rate of formation of the crosslink precursors, but also decreases the rate of final crosslink formation. Chapman and Porter [10] investigated the role of the zinc activator in accelerated vulcanization of natural rubber (NR). According to their studies, zinc oxide has little effect on the vulcanization rate, but increases the crosslinking efficiency. Moreover, when zinc oxide is present, sulphuration is mainly caused by substituting allylic hydrogen atoms, rather than by combining substitution and addition to the C=C double bonds. In this way, crosslink shortening is catalyzed, a network with a greater proportion of mono- and disulphidic crosslinks is formed, and the reversion is reduced. The presence of zinc oxide also leads to a small increase in scorch safety and cure time [1]. Zinc oxide can also be used as a crosslinking agent, e.g., of carboxylic rubbers [5, 11] and elastomers containing halogen groups [12]. Moreover, ZnO is sometimes applied as filler in elastomers, although some technological problems are encountered during preparation of mixtures (weak dispersion) [13]. There is also evidence that zinc oxide has a significant influence on physical properties of vulcanizates, such as heat build-up and abrasion resistance.

Since zinc cations from zinc oxide react with accelerators and cause active zinc-accelerator complexes (the key step in the vulcanization process), in order to increase the activity of zinc oxide, the availability of zinc ions should be increased. Due to the crystalline structure of ZnO, some ions are inside crystals and have limited accessibility. In order to reduce the amount of zinc compounds in rubber technology, it is necessary to incorporate more chemically active zinc into the elastomer matrix, in the form of reactive complexes.

In this work, we applied zinc chelates with 1,3-diketones as activators for crosslinking of acrylonitrile-butadiene rubber (NBR). It is believed that zinc chelates can be dispersed more easily in the elastomer matrix and that the accessibility of zinc ions is higher, although applications of such activators have not yet been reported.

2. Experimental section

2.1. Materials

Acrylonitrile-butadiene rubber NBR (Nipol DN 4050) containing 40 wt% of acrylonitrile was obtained from Zeon-Europe GmbH. Its Mooney viscosity was (ML1+4 (100°C): 46–60). It was cured with sulphur in the presence of 2-mercaptobenzothiazole (MBT). Nanosized zinc oxide with specific surface area 42.5 m^2/g and average particle size 234 nm (Qinetiq Nanomaterials Limited, Hampshire) together with stearic acid (Sigma-Aldrich) was applied as standard activator. As new activators of sulphur vulcanization, zinc chelates with 1,3-diketones as well as zinc acetylacetonate (Riedel-de Haën) were used. Zinc chelates with 1,3-diketones were synthesized using commercially available diketones according to the following procedure. Diketone was dissolved in acetone, then the water solution of potassium hydroxide was added to form potassium salt of diketone. The mixture was heated until it started to boil and water solution of zinc chloride was added. Afterwards, the mixture was heated for 1 h forming a precipitate of zinc chelate. The structures of the zinc complexes are given in Figure 1.

2.2. Preparation and characterization of rubber compounds

Rubber compounds with the formulations given in Table 1 were prepared using a laboratory two-roll mill. The samples were cured at 160°C until they developed a 90% increase of torque (measured using oscillating disc rheometer produced by ZACH METALCHEM). The tensile properties of vulcanizates were determined according to ISO-37 with a universal machine ZWICK 1435. The crosslinking density of vulcanizates was determined by equilibrium swelling in toluene, based on the Flory-Rehner equation [14] using Huggins

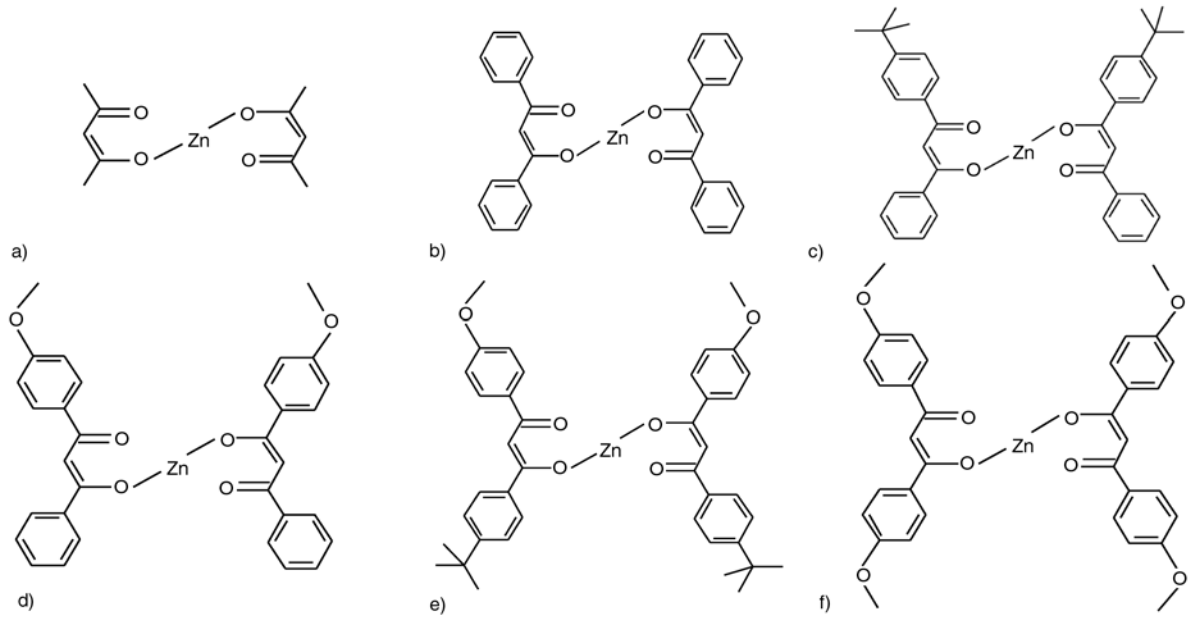

Figure 1. Zinc containing activators: a) zinc acetylacetonate AAC-Zn, b) zinc 1,3-diphenylpropane-1,3-dione BM-Zn, c) zinc 1-(4′-t-butylphenyl)-3-phenylpropane-1,3-dione BBM-Zn, d) zinc 1-(4′-methoxyphenyl)-3-phenylpropane-1,3-dione MBM-Zn, e) zinc 1-(4′-t-butylphenyl)-3-(4″-methoxyphenyl)propane-1,3-dione MBBM, f) zinc 1,3-bis-(4′methoxyphenyl)propane-1,3-dione MMBM-Zn

Table 1. Composition of the NBR based rubber compounds [phr]

Compound	M1	M2	M3	M4	M5	M6	M7
NBR	100	100	100	100	100	100	100
Sulphur	2	2	2	2	2	2	2
Accelerator (MBT)	2	2	2	2	2	2	2
Nano ZnO	2	–	–	–	–	–	–
Stearic acid	2	–	–	–	–	–	–
Zinc chelates	–	3[a]	3[b]	3[c]	3[d]	3[e]	2[f]

where a – BM-Zn, b – BBM-Zn, c – MBM-Zn, d – MBBM-Zn, e – MMBM-Zn, f – AAC-Zn

parameter of elastomer-solvent interaction $\mu = 0.381 + 0.671V_r$ (Equation (1)):

$$\nu_e = -\frac{\ln(1-V_r)+V_r+\mu V_r^2}{V_0\left(V_r^{\frac{1}{3}}-\frac{V_r}{2}\right)} \quad (1)$$

where ν_e crosslinking density, V_r volume fraction of elastomer in swollen gel, V_0 molar volume of solvent [mol/cm^3].

2.3. Surface properties of zinc chelates

The surface properties of zinc chelates were determined based on zeta potential measurements using a Zetasizer 2000 apparatus. The zeta potentials of zinc complex suspensions in water were measured as a function of pH. The concentration of suspensions was 0.02 g/l, and the pH was adjusted by adding HCl or NaOH solution.

2.4. Stability of zinc complexes

Stability of the examined zinc complexes was estimated based on the heat of zinc complex formation, which was calculated using HyperChem Release 7 software. It allowed to explore the structure and stability of zinc complex molecules using quantum mechanics. The HyperChem was used to create the starting geometries and refine molecular configurations of zinc complex structure. The molecules were constructed and converted to 3D structures. Next, the torsion angles between molecules fragments were varied and a full optimization of the structure geometry was performed to find the most stable one, which exhibits the lowest energy. After geometry optimization, the semi-empirical method

AM1 was applied to calculate the heat of formation of the possible zinc complex molecular structures.

2.5. Heterogeneity of elastomer network

The distribution of crosslinks in the elastomer network was estimated based on solvent freezing point depression of solvent confined in the polymer gel. Thermograms of solidification were recorded on a Differential Scanning Calorimetry (DSC) instrument (Perkin-Elmer DSC 7) by decreasing the temperature from 30 to –90°C at a rate of 10°C/min. Prior to this measurement, samples were swollen in benzene for 24 hours [15].

2.6. Dispersion of zinc chelates in elastomer matrix

The distribution of activator particles (zinc oxide and zinc complexes) was estimated using Scanning Electron Microscopy with a SEM microscope LEO 1530.

3. Results and discussion

3.1. Surface properties of zinc complexes

The zeta potential is an electrokinetic potential measured on the surface of a particle in solution. A charged surface results in the formation of an electric double layer, and the zeta potential is the potential between the charged surface and the electrolyte solution [16]. We examined the zeta potential of water-zinc chelates suspensions versus pH (Figure 2).

From the zeta potential measurements, we determined the isoelectric point (IEP) of zinc chelates. IEP is the pH value at which the zeta potential is equal zero. It is not a description of the absolute basicity or acidity of solid surface, but a description of their relative strength. A high IEP value indicates that the surface shows more basic functionality compared with its acidic functionality. On the contrary, a low IEP surface reveals less basic functionality comparing with its acidic functionality [13]. IEP is mainly related to the Brönsted acid-base definition. The higher IEP corresponds to stronger affinity to protons. However, IEP is also a measure of Lewis acidity or basicity, because when the oxide surface adsorbs a proton, the electron (or electron density) is transferred from oxygen to proton. Therefore, a strong proton acceptor is also a strong electron donor [16].

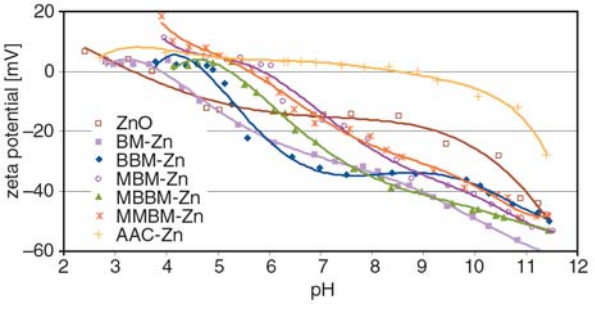

Figure 2. Zeta potential of zinc chelates

Table 2. Isoelectric points of zinc complexes

Zinc complex	Isoelectric point (IEP)
Nano ZnO	3.7
BM-Zn	4.2
BBM-Zn	4.9
MBM-Zn	5.8
MBBM-Zn	5.3
MMBM-Zn	5.7
AAC-Zn	8.7

The isoelectric point (IEP) of zinc oxide was determined at pH 3.8, whereas the IEP for zinc chelates was determined within the pH range from 4.2 (for BM-Zn) to 5.8 (for MBM-Zn) and at pH 8.7 for zinc acetylacetonate AAC-Zn. This indicates acid properties of zinc complex surfaces (especially BM-Zn and BBM-Zn), similar to pure ZnO (the isoelectric point is about pH 3.7; a negative zeta potential was determined in almost the whole range of measured pH) and basic properties of zinc acetylacetonate (a positive zeta potential and IEP at pH 8.7). Results are given in Table 2.

It should be noticed that zinc complexes with the most similar to zinc oxide surface properties exhibited the highest activity in crosslinking process. This could be due to their similar ability to interact with other components of crosslinking system (accelerator, sulphur) or with elastomer matrix.

3.2. Stability of zinc complexes

The stability of zinc complexes is considered to determine the effectiveness of zinc ions and the tendency of complexes to form intermediate active sulphurating agents during vulcanization. We therefore calculated the heat of zinc complex formation. It is known that the higher the heat of formation, the lower the stability of the compound. We also estimated the stability of a zinc complex with accel-

Table 3. Heat of zinc complex formation

Zinc complex	Heat of formation [kJ/mol]
BM-Zn	206.5
BBM-Zn	140.9
MBM-Zn	–114.8
MBBM-Zn	–271.7
MMBM-Zn	–437.0
AAC-Zn	–395.1
Zn-MBT	544.5

erator (2-mercaptobenzothiazole), which is formed during vulcanization when zinc oxide is present in the rubber compound (see results in Table 3).

In the more stable chelates, zinc ions have a reduced availability and lower tendency to form the zinc-accelerator complex during vulcanization process. Therefore, due to the lowest stability of 1,3-diphenylpropane-1,3-dione and 1-(4′-t-butylphenyl)-3-phenylpropane-1,3-dione (BM-Zn and BBM-Zn respectively), these were expected to influence the crosslinking process the most.

Zinc complexes exhibit lower heat of formation and higher stability than Zn-MBT complex, which is formed when zinc oxide is used as activator. Therefore, this system should be more accelerated than BM-Zn or BBM-Zn. However, the reduced availability of zinc ions in ZnO crystals comparing to zinc chelates causes the decrease in the rate of formation of zinc-accelerator complex during vulcanization process. As a result the cure rate of rubber compounds containing zinc oxide is smaller than BM-Zn or BBM-Zn chelates.

3.3. Effect of zinc complexes on vulcanization

The influence of zinc chelates on the cure characteristics of rubber compounds was estimated based on rheometer measurements. The cure characteristics of NBR compounds with different activators are given in Table 4 and Figure 3.

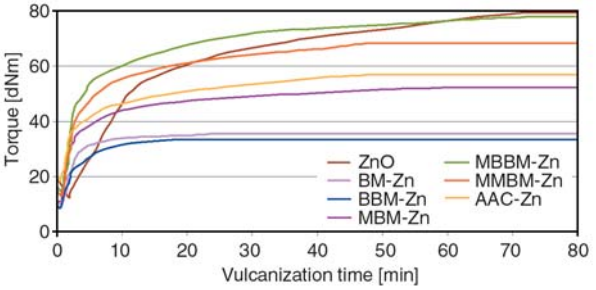

Figure 3. Rheometer isotherms of NBR compounds containing zinc complexes

Applying zinc chelates resulted in a higher cure rate compared to the conventional ZnO system, despite the fact that the zinc ion content in the cure system is several times smaller (Table 5). We believe that the increase in cure rate may be due to better availability of zinc ions in zinc complexes than in zinc oxide crystals. The zinc ions trapped in a crystal of ZnO are not used for crosslinking due to their limited accessibility. From this point of view, the crystal structure of ZnO is the most important parameter. The most common crystal structure of ZnO is wurtzite (zincite) [17], which has a hexagonal geometry, with each zinc atom surrounded by a tetrahedron of oxygen atoms. The whole structure consists of an interconnected network of tetrahedra. Based on ZnO lattice parameters [18], the amount of zinc ions available in a single crystal is estimated to be 1.8 mmole/g of ZnO. Therefore, the calculated amount of Zn^{2+} available for interaction with sulphur and accelerators in examined rubber compound is 3.6 mmole Zn^{2+}/100 g of elastomer. Moreover, Zn^{2+} ions in the ZnO nanoparticle are strongly connected to the crystal structure, and are less likely to form intermediate active sulphurating agents that can be observed during vulcanization.

Table 4. Cure characteristics of NBR compounds

Compound	ΔG [dNm]	t_{90} [min]	n	$k \cdot 10^3$ [s^{-1}]
NBR/nano ZnO	68.0	70	2	7.0
NBR/BM-Zn	24.9	25	2	76.2
NBR/BBM-Zn	24.0	20	2	84.0
NBR/MBM-Zn	40.8	60	2	13.3
NBR/MBBM-Zn	63.2	75	2	5.4
NBR/MMBM-Zn	54.6	50	2	20.3
NBR/AAC-Zn	38.8	50	2	18.5

ΔG – increment of torque in the rubber compound during vulcanization; t_{90} – optimal vulcanization time; n – order of the crosslinking reaction; k – the constant of the vulcanization rate

Table 5. Zinc content in zinc complexes applied in rubber compounds

Activator	Zn^{2+} content in activator [mmole/g]	Zn^{2+} content in rubber compound [mmole/100 g NBR]
ZnO (in bulk)	12.3	24.6
ZnO (on crystal surface)	1.8	3.6
BM-Zn	2.0	6.0
BBM-Zn	1.6	4.8
MBM-Zn	1.7	5.2
MBBM-Zn	1.5	4.5
MMBM-Zn	1.6	4.8
AAC-Zn	3.8	7.6

For vulcanization rate, the most effective activators seemed to be BM-Zn and BBM-Zn (Table 4). For rubber compounds containing these activators the shortest times of vulcanization and simultaneously the highest constants of vulcanization rate were determined. The lower efficiencies of AAC-Zn, MBM-Zn, MBBM-Zn and MMBM-Zn are probably related to the high stability of these complexes. In the cases of MBBM-Zn and MMBM-Zn, the steric hindrance of methoxy groups and t-butyl chains in a complex molecule (see Figure 1), which reduces the availability of zinc ions to form the zinc-accelerator complex, may also cause the lower efficiency of these complexes in vulcanization. According to Heideman *et al*. [7] different reactivities of zinc complexes result from their different basicity. The alkaline character of activator accelerates the sulphur vulcanization of rubber. Methoxy and t-butyl groups are known for their electron-withdrawing and electron donating abilities, which could affect the strength of the coordination bonds in the zinc complexes and therefore, the degree of their ionic nature. However, considering the structure of all zinc chelates with 1,3-diketones as well as the results of zeta potential measurements, which confirmed quite similar acid-base properties of zinc chelates, we concluded, that the main reasons of their different reactivity in crosslinking process are differences in complexes stability and availability of zinc ions in zinc complex molecule.

The considerably lower torque that was observed for compounds with zinc chelates had no detrimental effect on the physical properties of obtained vulcanizates.

3.4. Crosslink density of vulcanizates and the distribution of crosslinks in elastomer network

We analyzed the influence of different zinc activators on the crosslink density of NBR vulcanizates. The crosslink density was determined by equilibrium swelling of vulcanizates in toluene. Results are given in Table 6.

From the data presented, it follows that applying zinc complexes as activators in sulphur vulcanization of NBR had a detrimental effect on the crosslink density. The calculated values of crosslink density confirmed that the most effective zinc complexes in vulcanization were BM-Zn and BBM-Zn.

Table 6. Crosslink density of NBR vulcanizates containing zinc complexes

Vulcanizate	Q_w	$\nu_e \cdot 10^3$ [mole/cm^3]	E [crosslinks/mole of sulphur]
NBR/nano ZnO	1.34	11.7	1.50
NBR/BM-Zn	1.42	11.0	1.41
NBR/BBM-Zn	1.39	11.3	1.45
NBR/MBM-Zn	1.64	9.4	1.21
NBR/MBBM-Zn	1.62	9.6	1.23
NBR/MMBM-Zn	1.63	9.5	1.22
NBR/AAC-Zn	1.51	10.3	1.32

Q_w – equilibrium swelling of vulcanizate in toluene;
ν_e – crosslink density of vulcanizate; E – crosslinking efficiency

This seems even more important when we realize that the content of Zn^{2+} ions in 1 phr of BM-Zn and BBM-Zn is about six times smaller than in 1 phr of applied nanosized zinc oxide. A considerable decrease in crosslink density compared to conventional ZnO was observed when MBM-Zn, MBBM-Zn and MMBM-Zn were used as activators. The highest activity of BM-Zn and BBM-Zn chelates in vulcanization was also confirmed by the calculated values of crosslinking efficiency (Table 6). Only BM-Zn and BBM-Zn chelates allowed to achieve the crosslinking efficiency comparable with nanosized zinc oxide.

Apart from crosslink density, the distribution of crosslinks and the presence of defects in the elastomer network have a great importance as far as the mechanical properties of vulcanizates are concerned [19]. In other words, not only the number of crosslinks, but also their distribution and spatial arrangements contribute to the network mechanical performance. From a mechanical point of view, the heterogeneous distribution of crosslinks in the elastomer network is supposed to have a detrimental effect on mechanical properties of vulcanizates if we assume that densely crosslinked domains of the network concentrate stresses under external strain and initiate breaking of the sample. Therefore, vulcanizates with homogeneous structure exhibit higher tensile strength [20]. Vilgis and Henrich [21] postulated that heterogeneity of the network strongly affects the vulcanizate behavior under high strain and therefore, such mechanical properties as tensile strength and elongation at break. In less crosslinked part of the network the distribution of stress in crosslinked sample can be more effective as a result of stress relaxation. The propagation of microcracks within these areas could be hin-

dered and microcracks could rise only under higher stresses and deformations. As a result materials tensile strength and elongation at break increase.

The crosslink distributions in an NBR matrix were estimated based on freezing point depression of solvents confined in a polymer gel. It is a simple method to determine network structure in rubber composites. The freezing point depends on the conditions required for the formation of crystalline nuclei, that is limited by elastomer network restrictions and limitations in movement of polymer chains. From the data presented in Figures 4–8, it follows that the freezing point depression of solvent in swollen elastomer network depends on the crosslink structure. Two peaks were observed on DSC curves. The first, detected at (–6°C), is due to the crystallization of free benzene. The other corresponds to the crystallization of benzene entrapped in the swollen gel; its position depends on the crosslink density. The peak of confined solvent is shifted towards a lower temperature compared to the free benzene peak. In the case of vulcanizates crosslinked in the presence of zinc complexes (Figures 4–8), the peak of benzene entrapped in the swollen network is shifted towards higher temperatures compared to a vulcanizate containing conventional zinc oxide. This behavior corresponds to a decrease of network density, which agrees with the spatial structure parameters of vulcanizates given in Table 6. Moreover, broadening of solidification peaks suggests broadening of the distribution of mesh sizes.

According to Baba [15], the peak position of the solvent confined in the polymer gel is directly related to the radius of the mesh (R_p) by the Equation (2):

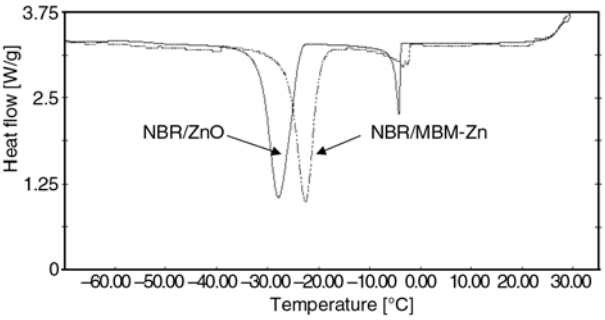

Figure 6. DSC thermogram of swollen NBR vulcanizates containing: zinc oxide (continuous line), MBM-Zn chelate (broken line)

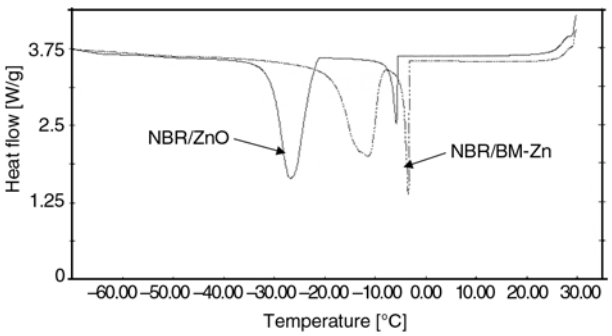

Figure 4. DSC thermogram of swollen NBR vulcanizates containing: zinc oxide (continuous line), BM-Zn chelate (broken line)

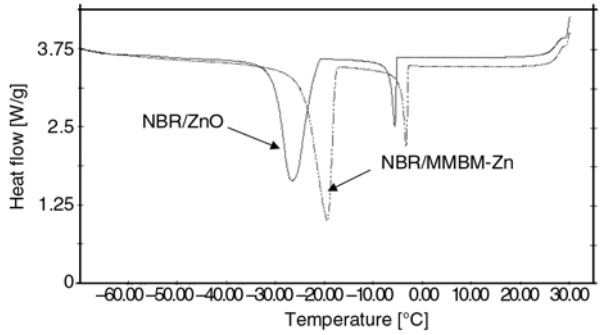

Figure 7. DSC thermogram of swollen NBR vulcanizates containing: zinc oxide (continuous line), MMBM-Zn chelate (broken line)

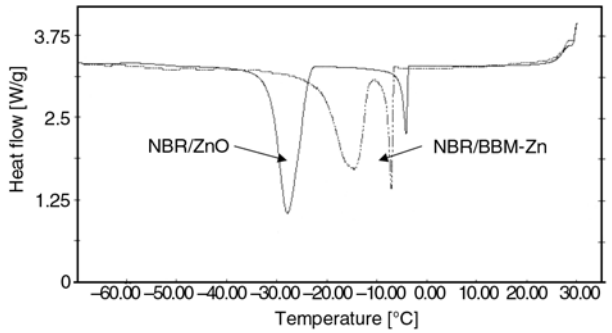

Figure 5. DSC thermogram of swollen NBR vulcanizates containing: zinc oxide (continuous line), BBM-Zn chelate (broken line)

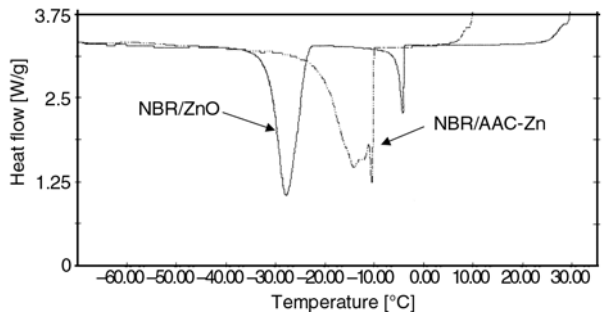

Figure 8. DSC thermogram of swollen NBR vulcanizates containing: zinc oxide (continuous line), AAC-Zn complex (broken line)

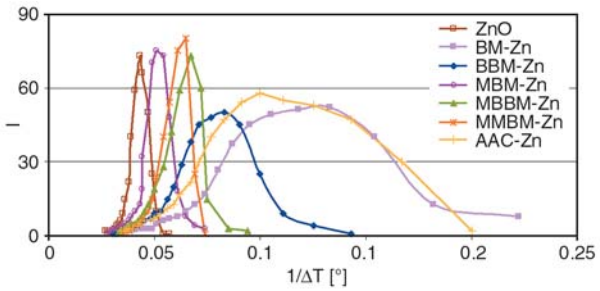

Figure 9. Distribution of molecular weights (I) between network crosslinks in vulcanizates containing zinc complexes

$$R_p = \frac{-A}{\Delta T} + B \tag{2}$$

where $\Delta T = T_0 - T$; T_0 is the triple point temperature of solvent; and A, B are constants depending on the solvent.

The radius of the mesh is proportional to the molecular weight of the network between crosslinks M_c. Therefore, to analyze the vulcanizate structures, we estimated the distribution of molecular weights between crosslinks. Results are presented in Figure 9.

Parameter I corresponds to the molecular weight of the network between crosslinks and was estimated based on the peak intensity of benzene confined in a swollen gel. The data presented in Figure 9 indicates that the distribution of crosslinks in the elastomer network resembles a Gaussian distribution. However, broadening of the crosslink distribution was observed for vulcanizates obtained with AAC-Zn, BM-Zn and MBBM-Zn zinc complexes. Therefore, it can be concluded that the elastomer networks obtained using these zinc chelates are more heterogeneous than those formed with zinc oxide as the activator. On the contrary the crosslinks distribution in vulcanizates with MBM-Zn and MMBM-Zn complexes was narrower. Vulcanizates with heterogeneous networks exhibited considerably higher tensile strength (see results in Table 7). Therefore, the heterogeneity of the network helps improve the vulcanizate mechanical properties.

Table 7. Mechanical properties of NBR vulcanizates containing zinc complexes

Vulcanizate	SE_{300} [MPa]	TS [MPa]	EB [%]
NBR/nano ZnO	2.7	10.3	541
NBR/BM-Zn	2.1	16.8	621
NBR/BBM-Zn	2.3	15.6	609
NBR/MBM-Zn	1.7	9.2	724
NBR/MBBM-Zn	1.3	13.8	766
NBR/MMBM-Zn	1.5	12.7	721
NBR/AAC-Zn	2.6	15.0	706

SE300 – stress at 300% relative elongation; TS – tensile strength; EB – elongation at break

3.5. Mechanical properties of vulcanizates

Having established the effect of zinc chelates on the vulcanization of rubber compounds, we then examined the mechanical properties of vulcanizates. Results are given in Table 7.

From the data compiled in Table 7, it follows that applying zinc chelates considerably increased the tensile strength of vulcanizates compared to using conventional ZnO. The stress at a relative elongation of 300% slightly decreased, which may be a result of the crosslink density decrease. It is worth noticing that vulcanizates containing zinc complexes have a higher elongation at break corresponding to their higher elasticity.

As far as the tensile strength of vulcanizates is concerned, the most effective appeared to be zinc acetylacetonate, BM-Zn and BBM-Zn complexes, much like the cure characteristics presented in the previous section. These zinc complexes contain higher Zn^{2+} ion content and have the best availability of these ions as well. However, using MMBM-Zn and MBM-Zn especially had a detrimental effect on the tensile strength of vulcanizates. The explanation for the deterioration of mechanical properties may be: difficult availability of zinc ions in chelates due to steric hindrance, lower content of Zn^{2+} ions compared to other complexes, the presence of methoxy groups in the complex molecule as well as homogeneity of elastomer network (according to DSC thermograms in Figures 6 and 7). It should be noticed that vulcanizate containing MBBM-Zn exhibited high tensile strength and elongation at break despite lower zinc ions content and the presence of methoxy groups. It could be a result of network heterogeneity. This observation confirmed that elastomer network heterogeneity caused the improvement of vulcanizates physical properties.

3.6. Dispersion of zinc chelates in elastomer matrix

Assuming that the particles of accelerators, sulphur, and fatty acids diffuse through the polymer

matrix and are adsorbed on the surface of zinc oxide forming intermediate complexes [6], the dispersion of zinc oxide particles in the elastomer matrix has a great importance as far as the activation of sulphur vulcanization is concerned. SEM images of the vulcanizate surfaces were taken to estimate the dispersion of activator particles in the elastomer (Figures 10a–10f).

ZnO nanoparticles are poorly dispersed in the elastomer matrix and therefore are not homogeneously distributed (Figure 10a). They create microsized clusters of particles (agglomerates) with complex structures. Additionally, the tendency of zinc oxide nanoparticles to agglomerate in the elastomer matrix was confirmed by rheological studies of zinc oxide suspensions in paraffin oil (model of

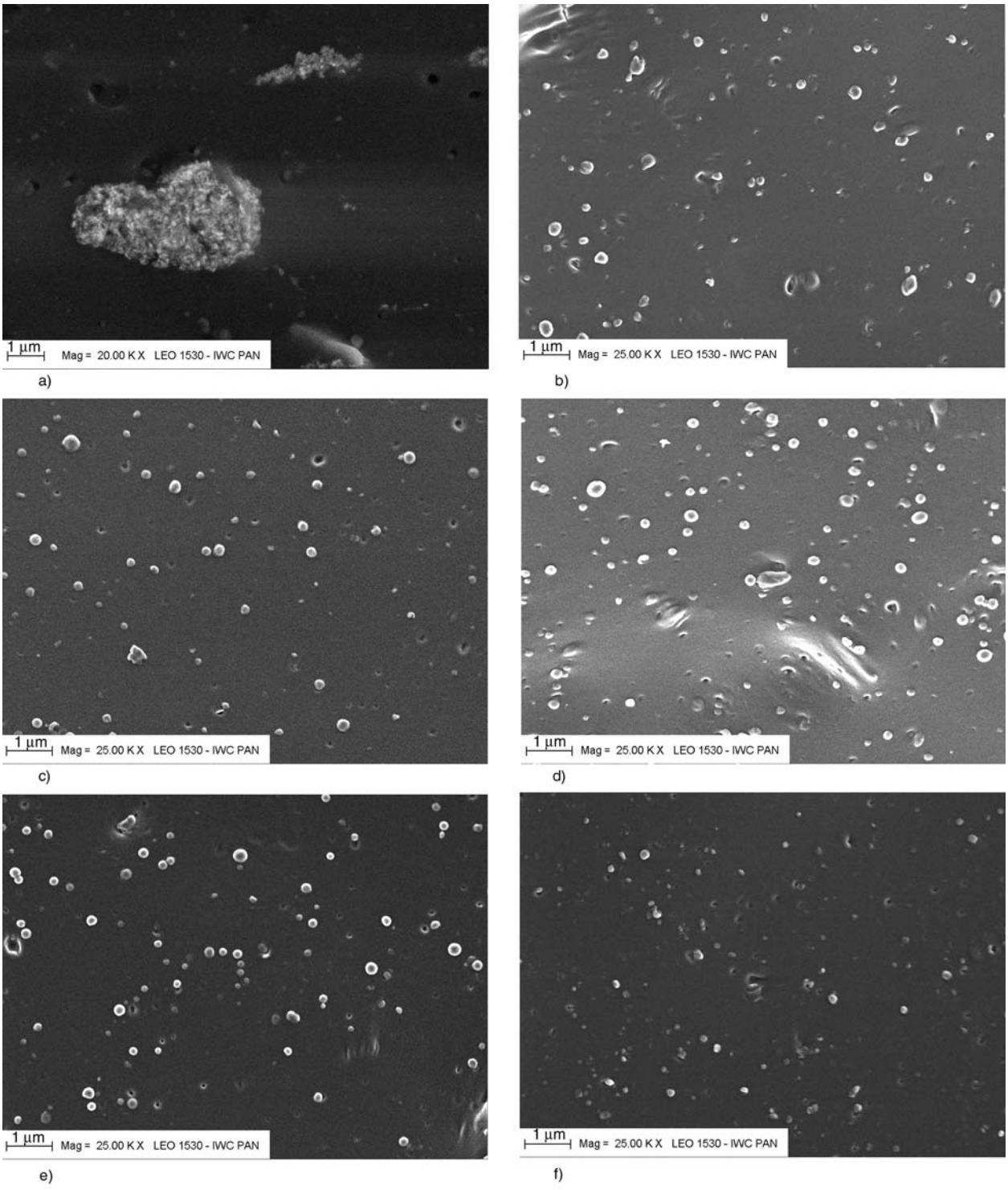

Figure 10. SEM images of NBR vulcanizates a) with nanosized ZnO, b) with BM-Zn, c) with MBM-Zn, d) with MBBM-Zn, e) with MMBM-Zn, f) with zinc acetylacetonate AAC-Zn

elastomer matrix), presented in our previous work [22]. The agglomeration of zinc oxide particles causes their surface area to decrease followed by a decrease of the interface between the zinc oxide and other components of the crosslinking system. As a result, zinc oxide was observed to be less efficient as an activator of sulphur vulcanization. Moreover, agglomerates of zinc oxide particles may be responsible for local increases in crosslink density in vulcanizates, which may initiate breaking of the sample under external stress.

Zinc chelate particles, on the other hand, are homogenously distributed in the elastomer (Figures 10b–10f). The estimated size of zinc complex particles seems to be in the nanometer range, which makes their surfaces available for interactions. This is why their interactions with sulphur and accelerators are more efficient. Despite homogenous dispersion of particles, vulcanizates containing zinc complexes have more heterogeneous networks than vulcanizates crosslinked with zinc oxide as activator. The reason is that SEM micrographs show only the 'macro-dispersion', which is not identical with uniformity of the zinc ions concentration. The differences in dispersion of nanosized zinc oxide and zinc complexes are due to their different solubility and miscibility with elastomer as well as high surface energy of zinc oxide nanoparticles that results in their agglomeration [22].

4. Conclusions

Zinc acetylacetonate and zinc complexes with 1,3-diketones were used as activators for sulphur vulcanization of NBR.

We conclude that zinc complexes are good substitutes for ZnO as activators in sulphur vulcanization of butadiene-acrylonitrile rubber, without any detrimental effect on the crosslinking rate, or physical properties of vulcanizates. The slight decrease in crosslinking density of vulcanizates and efficiency of crosslinking process did not influence their mechanical properties. Zinc 1,3-diphenylpropane-1,3-dione (BM-Zn) and zinc 1-(4′-t-butylphenyl)-3-phenylpropane-1,3-dione (BBM-Zn) were the most effective as crosslinking activators. The lower efficiency of zinc acetylacetonate and other examined zinc chelates is related to the stability of the complexes. In the more stable zinc complexes, the zinc ions are less available to form the active sulphurating agent (the zinc-accelerator complex that can react with allylic sites of elastomers unsaturations to form the crosslink precursor). Moreover, the steric hindrance of methoxy groups and t-butyl chains in a complex molecule of MBBM-Zn and MMBM-Zn seemed to reduce the availability of zinc ions during vulcanization.

As a general conclusion, we claim that zinc complexes with β-diketones applied in the crosslinking process help obtain vulcanizates with properties similar to those with nanosized ZnO. This reduces the amount of zinc ions applied by 40% compared to zinc oxide. This is particularly relevant as reducing the use of Zn^{2+} ions is an important ecological goal.

Acknowledgements

The authors wish to acknowledge the Polish Ministry of Science and Higher Education for supporting this research.

References

[1] Chapman A., Johnson T.: The role of zinc in the vulcanisation of styrene-butadiene rubbers. Kautschuk Gummi Kunststoffe, **58**, 358–361 (2005).

[2] Brydson J. A.: The Chemistry of Rubber. Applied Science, London (1978).

[3] Li Z. H., Zhang J., Chen S. J.: Effects of carbon blacks with various structures on vulcanization and reinforcement of filled ethylene-propylene-diene rubber. Express Polymer Letters, **2**, 695–704 (2008).
DOI: 10.3144/expresspolymlett.2008.83

[4] Luyt A. S., McGill W. J., Shillington D.: A DSC study of the interaction of 2-mecraptobenzothiazole, sulphur, ZnO and stearic acid in the absence of rubber. British Polymer Journal, **23**, 135–139 (1990).
DOI: 10.1002/pi.4980230122

[5] Kruger F. W. H., McGill J.: A DSC study of curative interactions. I. The interaction of ZnO, sulfur, and stearic acid. Journal of Applied Polymer Science, **42**, 2643–2649 (1991).
DOI: 10.1002/app.1991.070421002

[6] Coran A. Y.: Chemistry of the vulcanization and protection of elastomers: A review of the achievements. Journal of Applied Polymer Science, **87**, 24–30 (2003).
DOI: 10.1002/app.11659

[7] Heideman G., Noordermeer J. W. M., Datta R. N., van Baarle B.: Effect of zinc complexes as activator for sulfur vulcanization in various rubbers. Rubber Chemistry and Technology, **78**, 245–257 (2005).

[8] Nieuwenhuizen P. J.: Zinc accelerator complexes: Versatile homogeneous catalysts in sulfur vulcanization. Applied Catalysis A: General, **207**, 55–68 (2001). DOI: 10.1016/S0926-860X(00)00613-X

[9] Mark J. E., Eirich F. R., Erman B.: Science and technology of rubber. Academic Press, San Diego (1994).

[10] Chapman A. V., Porter M.: Sulphur vulcanization chemistry. in 'Natural rubber science and technology' (ed.: Roberts A. D.) Oxford University Press, Oxford, 511–620 (1988).

[11] Fritzsche J., Das A., Jurk R., Stöckelhuber K. W., Heinrich G., Klüppel M.: Relaxation dynamics of carboxylated nitrile rubber filled with organomodified nanoclay. Express Polymer Letters, **2**, 373–381 (2008). DOI: 10.3144/expresspolymlett.2008.44

[12] Sae-oui P., Sirisinha C., Hatthapanit K.: Effect of blend ratio on aging, oil and ozone resistance of silica-filled chloroprene rubber/natural rubber (CR/NR) blends. Express Polymer Letters, **1**, 8–14 (2007). DOI: 10.3144/expresspolymlett.2007.3

[13] Ohm R. F.: Rubber chemicals. in 'Kirk-othmer encyclopedia of chemical technology' (ed.: Howe-Grant M.) John Wiley and Sons, New York, Vol 21, 460–481 (1997). DOI: 10.1002/0471238961.18210202150813.a01

[14] Flory P. J., Rehner J.: Statistical mechanics of cross-linked polymer networks. II. Swelling. Journal of Chemical Physics, **11**, 521–526 (1943). DOI: 10.1063/1.1723792

[15] Baba M., Gardette J-L., Lacoste J.: Crosslinking on ageing of elastomers II. Comparison of solvent freezing point depression and conventional crosslinking evaluation. Polymer Degradation and Stability, **65**, 415–420 (1999). DOI: 10.1016/S0141-3910(99)00030-0

[16] Sun C., Berg J. C.: A review of the different techniques for solid surface acid-base characterization. Advances in Colloid and Interface Science, **105**, 151–175 (2003). DOI: 10.1016/S0001-8686(03)00066-6

[17] Zecchina A., Lamberti C., Bordiga S.: Surface acidity and basicity: General concepts. Catalysis Today, **41**, 169–177 (1998). DOI: 10.1016/S0920-5861(98)00047-9

[18] Yin J., Liu Z. G., Liu H., Wang X. S., Zhu T., Liu J. M.: The epitaxial growth of wurtzite ZnO films on $LiNbO_3$ (0001) substrates. Journal of Crystal Growth, **220**, 281–285 (2000). DOI: 10.1016/S0022-0248(00)00861-7

[19] Shah G. B.: The effect of bimodality on tensile properties of filled silicone networks. Express Polymer Letters, **2**, 878–884 (2008). DOI: 10.3144/expresspolymlett.2008.102

[20] Hernandez L. G., Diaz A. R., de Benito Gonzales J. L., Orosa I. F., Fernandez A. M.: Effects of the structure and crosslink distribution on the physical properties of a natural rubber network: Comparison of sulfur, peroxide and benzene-1,3-disulfonylazide crosslinking systems. Kautschuk Gummi Kunststoffe, **45**, 1033–1037 (1992).

[21] Vilgis T. A., Heinrich G.: New aspects in rubber elasticity: A challenge for theoretical physics and applied materials sciences. Kautschuk Gummi Kunststoffe, **45**, 1006–1014 (1992).

[22] Zaborski M., Przybyszewska M.: Nanoparticle zinc oxide applied for crosslinking of butadiene rubbers. in '8th European Symposium on Polymer Blends and Eurofillers, Bruges, Belgium', 116 (2005).